ELECTRONIC STRUCTURE AND ENERGETICS OF FE-BASED SUPERCONDUCTORS: EFFECTS OF CHEMICAL AND MAGNETIC DISORDER IN (BA-X)(FE-Y)$_2$AS$_2$

BY

SUFFIAN NAEEM KHAN

DISSERTATION

Submitted in partial fulfillment of the requirements
for the degree of Doctor of Philosophy in Physics
in the Graduate College of the
University of Illinois at Urbana-Champaign, 2014

Urbana, Illinois

Doctoral Committee:

Professor David Ceperley, Chair
Professor Duane Johnson, Director of Research
Professor Lance Cooper
Professor Tim Stelzer

Abstract

The Fe-based superconductors (Fe-SCs) have reinvigorated the community of high-T_c researchers worldwide. Like copper-oxide superconductors (Cu-SCs), they are layered compounds in proximity to an antiferromagnetic (AFM) state. The Fe-SC systems are amenable to controlled chemical doping/alloying, exhibiting coexistence of AFM and SC, as well as structural transformations versus temperature and pressure that lead to competing magnetic and structural defects. Because of this, exploration of the electronic structure of the normal (non-SC) state, and its related properties, may reveal key physics underlying connections between structure, magnetism and SC.

In this thesis we study the phase stability, electronic structure, and magnetism of alloyed (Ba-Am)(Fe-Tm)$_2$As$_2$ superconductors involving transition metals (Tm=Co, Ni, Cu, Zn) and alkali metals (Am = K, Na) in nonmagnetic, paramagnetic, and antiferromagnetic states for the competing tetragonal and orthorhombic structures. These cover prominent electron (Tm) and hole (Am) doping scenarios studied experimentally. To accomplish this in a unified way, we utilize a Green's function approach based upon the all-electron, Korringa-Kohn-Rostoker (KKR) multiple scattering theory in combination with the coherent-potential approximation (CPA) to handle chemical (alloying) and magnetic (orientational) disorder, all implemented within a self-consistent-field, density functional theory (DFT). For Tm doping, we detail the Fermi-surface evolution and nesting that dictate instabilities to the observed spin-density wave (SDW) state. For Am doping we track topological changes in the Fermi surface and connect these to transitions between SC phases. For K-doping, dissolution of electron cylinders occurs near 90%K with a Lifshitz (topological) transition, as observed, which reduces key inter-band interactions. This result reveals a transition that influences $s^{\pm}$ to d-like SC and suggests the origin for the deviations for the empirically identified Bud'ko-Ni-Canfield scaling. Formation energies indicate alloying at 35%K, as observed, but a tendency for segregation on the K-rich ($\geq$ 60%K) side, explaining the difficulty of controlling sample quality and conflicting results between characterized electronic structures.

In addition, due to the observed proliferation of twins and magnetic twin boundaries in $BaFe_2As_2$ (and possible other operative magnetic planar defects) with temperature and pressure, we study the stability and

magnetic properties of competing antiphase and domain boundaries, twins and isolated *nano*twins (twin nuclei). These nanoscale defects have very low surface energy (22-210 $m\mathrm{Jm}^{-2}$), with twins favorable to the mesoscale. The *nano*twins explain features in measured pair distribution functions obtained from neutron diffraction. Notably, these low-energy defects are tied to the magneto-structural transition whose fluctuations are widely expected to drive SC.

To my Father and Mother.

Acknowledgments

This project would not have been possible without the support of many people. Many thanks to my adviser, Professor Duane Johnson, who provided guidance and support. I thank research fellows Drs. Aftab Alam, Nikolai Zarkevich, and Andrei Smirnov for their tutorship. I thank Dr. Jason Reich for stimulating discussion in the office. I thank Professor Lance Cooper for patiently advising me as I searched for a thesis adviser. I thank Professors David Ceperley and Tim Stelzer for serving on my committee. At the Ames Laboratory and Iowa State University I thank Professors Paul Canfield, Sergey Bud'ko, Alan Goldman, and Rob McQueeney as well as Drs. Andreas Kreyssig, Yongbin Lee, and Mingyu Kim for research discussions. I thank my parents, Dr. Naeem Khan and Huma Khan, for their love and financial support. I thank my good friends Nir Friedman, Juan Atkinson, Aditya Sharma, Yun Liu, Teck Tan, Fawad Ismail, Lance Min, Hamood Arham, and Jitong Yu in Urbana-Champaign, Illinois and Arun Madhavan, Cameron Biaganek, Zaid Hashim, Jeritt Tucker, Orpheus Kypris, Marius Dragomiroiu, Lawrence Crowley, Zachary Yaple, Jordan Schlek, Brandt Jensen, Ceren Gunsoy, and Jarrod Brockman in Ames, Iowa for making graduate school memorable.

It is important to acknowledge the support for my Ph.D. thesis provided through the Center for Defect Physics, an Energy Frontier Research Center at Oak Ridge National Laboratory, funded by the U.S. Department of Energy (DOE), Office of Science, Basic Energy Sciences, Materials Science and Engineering Division. In addition, I would like to thank the hospitality and support of the Ames Laboratory and the Division of Materials Science and Engineering, where much of this work was performed while a research assistant at the University of Illinois Urbana-Champaign. The Ames Laboratory is operated for the U.S. DOE by Iowa State University under contract DE-AC02-07CH11358.

Table of Contents

Chapter 1

Fe-based Superconductors

Since the discovery of high-temperature superconductivity (SC) in copper-oxide compounds by Bednorz and Müller in 1987 [1], much effort has been invested in finding SC in other transition-metal oxides. But, with critical temperatures (T_c) often below 5 K, this program has had little success. Then, in 2008, while investigating transparent oxide semiconductors, Kamihara et al. [2] discovered $LaFeAsO_{1-x}F_x$ superconducts at $T_c = 26$ K. As magnetic impurities are known to be highly deleterious to SC, it came as a surprise that strongly magnetic Fe could serve as a building block for SC. The high-T_c and weak isotope effect clearly mark these compounds as a new class of unconventional superconductor (USC). So, Fe-based superconductors (Fe-SC) have reignited an interest in high-T_c superconductivity; and, with it, the hope of further unraveling the microscopic mechanisms driving USC. If a predictive model of USC is reached, it could permit a rapid computational search for a room-temperature superconductor —a holy grail. Shortly after Kamihara et al.'s work, Rotter et al. [3] found superconductivity in $Ba_{1-x}K_xFe_2As_2$. This established the two most studied classes of Fe-SCs. To date, there have been thousands of publications on the Fe-SCs. By chemical and pressure tuning, T_c has been raised to 65 K. While the prospect of a still higher T_c is limited, the Fe-SCs remain exciting as a pathway for making theoretical progress on the question of unconventional pairing. They also have unique material properties, including a strong coupling of magnetism, structure, and superconductivity. As an applied technology, the Fe-SCs can be used for their high critical fields (up to 50 T) and high critical currents (10^6 A cm^{-2}). Moreover, these critical quantities are more isotropic than for the copper-oxide superconductors (Cu-SC) and may supplant SCs used in some of today's high-field magnets. Other applications could include power generation and, due to an interplay of itinerant and local magnetism, spintronics.

Questions, therefore, arise for the Fe-SCs: What is the normal state quasiparticle spectrum? What drives the magnetic and SC instabilities? What is the structure and symmetry of the SC gap parameters? What viable pairing mechanisms are there? As magnetism and SC arise from instabilities in the electronic structure, a characterization of the normal state is key to understanding unconventional pairing.

The goal of this dissertation is to understand the normal state electronic structure, phase stability, and

magnetism of (Ba-Am)(Fe-Tm)$_2$As$_2$ alloys for transition metals Tm=Co, Ni, Cu, Zn and alkali metals Am = K, Na from first-principles density functional theory (DFT). These correspond to electron (Tm) and hole (Am) doped variants of $BaFe_2As_2$. In particular, the Fermi surface evolution is charted in these compounds and marked changes are tied to magnetic and SC transitions. The observed proliferation of magnetic planar defects that affect the magneto-structural transition are explained. Magneto-structural fluctuations likely play a role in nematic order and Cooper pairing. Calculations were performed using the all-electron, Korringa-Kohn-Rostoker (KKR) [4, 5] method in combination with the coherent potential approximation (CPA) [6], a single-site mean field theory to address both chemical (alloying) and magnetic (orientational) disorder. Extensive code development was done to provide a detailed analysis of alloyed electronic structure, including electronic dispersion, density of states, and Fermi surfaces. Code was also developed to improve the accuracy of the Fermi surface and to improve the robustness of calculations.

As SC is not the immediate focus, an overview of the phenomena and theory of superconductivity, including the Bardeen-Cooper-Schrieffer (BCS) theory of superconductivity is provided in the appendix. The terminology of the BCS theory and the notion of pairing symmetries sets a backdrop for many articles on SC. For further background see [7, 8, 9, 10, 11]. Below a summary of unconventional superconductors and details of Fe-SCs, in particular, is given. Good reviews on Fe-SCs are provided by references [12, 13, 14, 15, 16, 17, 18].

1.1 Unconventional Superconductors

Berndt Matthias, a prominent experimentalist in the 1970s who discovered a large number of SCs, formulated six rules to discovery [19]: 1. High symmetry is good, cubic symmetry is best, 2. High density of electronic states is good, 3. Stay away from oxygen, 4. Stay away from magnetism, 5. Stay away from insulators, and 6. Stay away from theorists. Many of the USCs, most of which have been discovered since then, break those rules in a dramatic fashion. *An USC is one in which Cooper pairs are not an s-wave singlet or are not mediated by an electron-phonon interaction.* They include so-called organics, heavy fermions, Cu-SCs, and, most recently, Fe-SCs. These often have higher T_c than allowed by a BCS weak electron-phonon coupling and also show a limited isotope effect. To this day a rigorous theory of USCs is lacking.

Organic superconductors are any organic compound that features SC. That makes them a broad class of SC that need not share underlying pairing mechanisms. They display especially rich phase diagrams and come in one-, two-, and three-dimensional varieties (i.e., one or more direction may be strongly insulating). A commonly studied example is (BEDT-TTF)$_2X$, where X is an anion separating layers of the organic

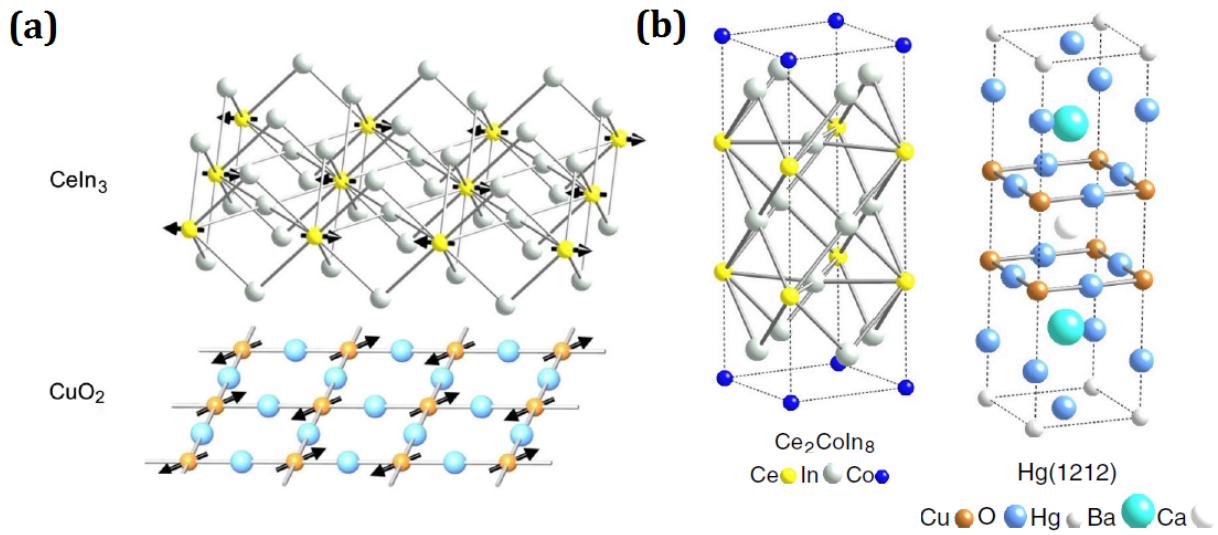

Figure 1.1: (a) Active structural layers for Cu-SCs and Ce-based heavy fermion SCs. Both show an AFM pattern in the ground-state. (b) The complete crystal structure for representative examples. In fact, the active layers and spacer layers can be combined in different arrangements, giving rise to a number of possibilities. After [20].

BEDT-TTF (a large organic molecule). At ambient pressure they are Mott insulating and become SC only under pressure. Pressure serves to increase hybridization effects and improve transport, especially along the c-axis (defined as perpendicular to layers). These support a lattice of spin 1/2 molecular dimers that are in a frustrated arrangement. The suggested pairing symmetry is d-wave; that, and the Mott insulating phase, have drawn strong comparisons to Cu-SCs. One advantage of organic SCs is that constituent elements are readily available. Their T_c does not exceed 12 K, however.

Heavy fermions are Ce or U based alloys take advantage of f electrons hybridizing with itinerant electrons to form heavy quasiparticles. As a strongly magnetic ion in contact with conduction electrons, they exhibit the Kondo effect –an unusual interaction of conduction electrons and magnetic impurities. Because they arrange in a regular lattice, one also refers to the Kondo lattice. The Kondo lattice leads to an unusual three orders of magnitude increase in the electronic specific heat. As heavy rare-earths are embedded in active, superconducting layers, inclusion of strong spin-orbit coupling is crucial to a proper description of pairing. UPt_3 is one of the better understood examples. Altogether, three SC phases have been identified for it, showing nearly degenerate SC states are realizable. The order parameter goes as $e^{i2\phi}$, suggesting an exotic f-wave symmetry (or, in terms of lattice symmetries, more precisely "E_{2u}"). Most of the heavy fermions are near an AFM transition. An important counterexample, both for heavy fermions and for USCs in general, is UGe_2, which is both ferromagnetic and SC. The calculated and observed Fermi surfaces are

nearly two-dimensional, emphasizing the effectiveness of layering and c-axis "blocking."

The active layers in Cu-SCs consist of the flat sheets of Cu and O atoms. The electronic structure is two-dimensional and there is only one active band at the Fermi level. It is well established by phase sensitive experiments that the gap has d-wave symmetry. Only for the Cu-SCs has such a clear symmetry been shown in the order parameters. It is well known they have the highest T_c, with maximum of 133 K (ambient pressure) or 150 K (high pressure) for $HgBa_2Ca_2Cu_3O_8$. They have strongly correlated electrons, which gives rise to local moments on the Cu site. Thus, they are best described by a single-band Hubbard model. Like other USCS, the parent compounds are in a Mott insulating AFM phase.

What ties to together many of the USCs is a layered structure with active layers that can be tuned by chemical and pressure effects. Parent compounds are insulating or semi-metallic, and valence states are composed of d or f electrons. Magnetic phases, especially AFM, are abundant. SC arises when the magnetic phase is diminished by tuning parameters and could be a result spin fluctuations or a quantum critical point. Now we explore the details of Fe-based superconductors, of specific focus here.

1.2 Fe-based superconductors

The Fe-SCs are built from electronically active tri-layers of Pn-Fe-Pn (Pn = As, P, Se, Te, S) that can tuned by chemical substitution or applied pressure. The highest T_c to date is 65 K in single-layer FeSe films [22], making them second only to Cu-SCs in order of T_c. Both the high T_c and explicit electron-phonon coupling calculations make clear Cooper pairs in these compounds cannot be mediated by traditional phonon pairing mechanisms [23, 24]. The Fe-SCs present themselves in two major classes: ReFeAsO (rare earth Re = La, Ce, Pr, Nd, Sm, Gd) and $Ae Fe_2As_2$ (alkali earth Ae = Ca, Ba, Sr) and their chemically tuned derivatives. There are also two minor classes. These include AmFeAs (alkali metal Am=Li, Na) and FeCh (chalcogenide Ch = Se, Te, S). With the exception of FeCh, the active tri-layers are separated by intervening "blocking" layers that improve two-dimensionality, stabilize the structure, and donate charge carriers. The Fe-SCs from the major classes are metallic antiferromagnets (AFM) at stoichiometry and prove to be robust under chemical doping, even allowing in-plane disorder. The valence electronic structure arises from a hybridization of As $4p^3$ and Fe $3d^5$ electrons, which have combined in covalent bonds to form $FeAs_4$ tetrahedra. The Fermi surface arises from all Fe d orbitals, giving rise to multiple electron and hole Fermi sheets. Pairing is likely mediated by interband interactions between hole and electron quasiparticles. And strong Fermi surface nesting may be the source of the observed AFM. At modest doping and low pressures, the Fe-SCs are believed to exhibit the same SC phase with universal characteristics. The gap parameter is proposed to have s-wave symmetry

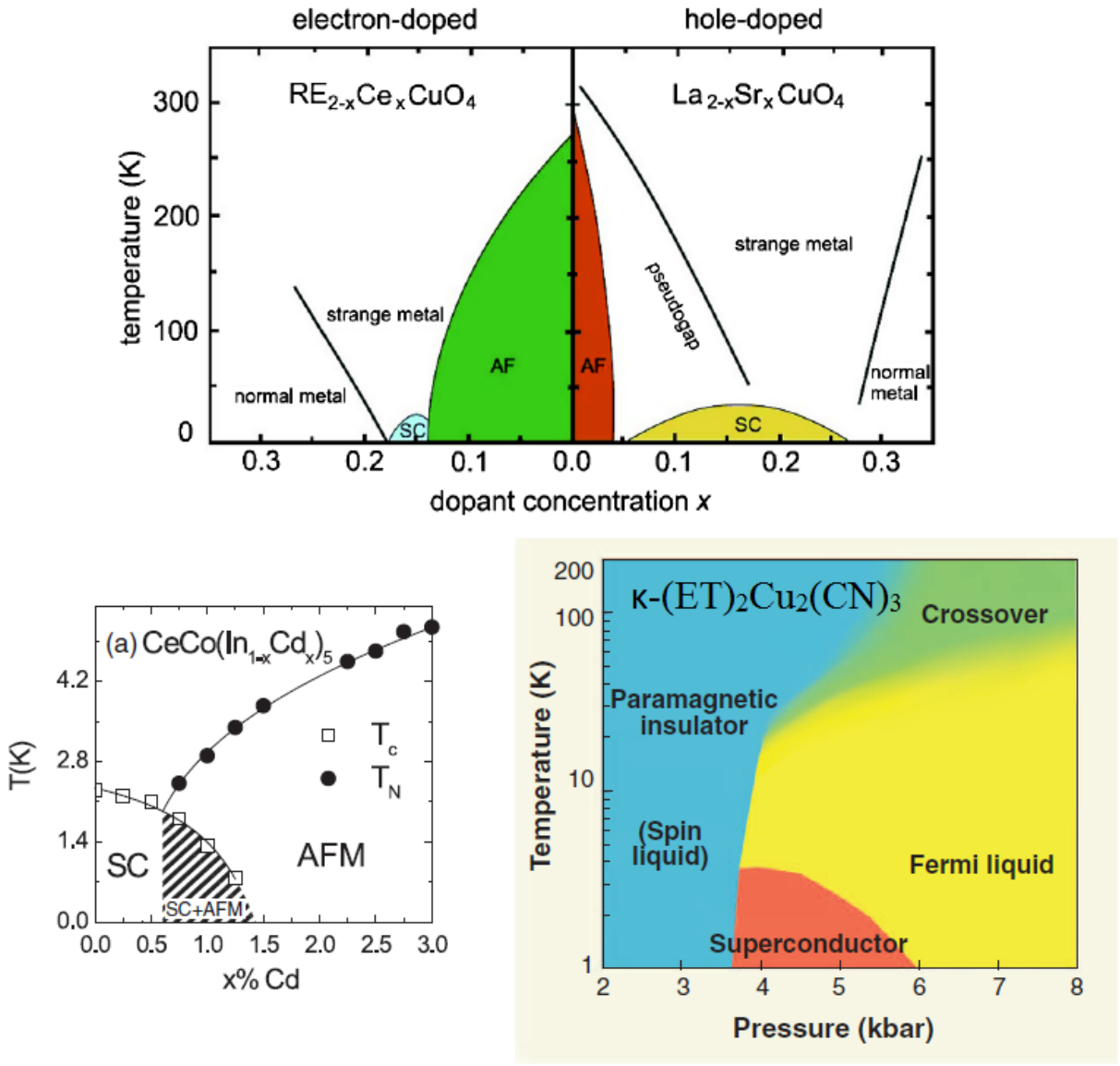

Figure 1.2: Phase diagrams of representative copper-oxide, heavy fermion, and organic superconductors. Neighboring magnetic phases are often present. After [20, 21]

.

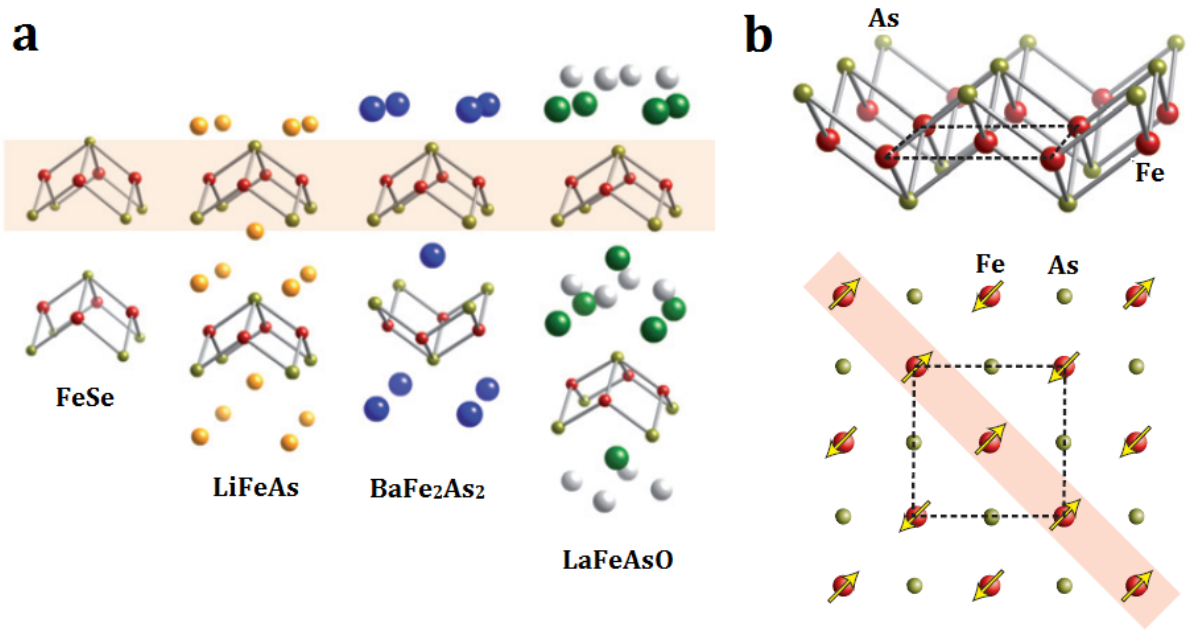

Figure 1.3: (a) The four classes of Fe-SCs and their associated structures. (b) The common structural motif of As-Fe-As trilayers and the striped antiferromagnetic pattern. After [14].

with a sign change between Fermi sheets. The key effects of doping and pressure are to reduce Néel T_N, thereby increasing AFM spin fluctuations and bringing the system closer to a quantum critical point (QCP). The Néel transition is also accompanied by an orthorhombic distortion likely driven be nematic electron ordering.

Because they are weak metals that show at most modest correlations, the electronic-structure is reasonably predicted by density functional theory (DFT) calculations, which often agree with angle-resolved photoemission (ARPES). This makes these compounds more amenable to realistic computations than the Cu-SCs. At higher doping there is evidence the SC phase changes. There are for instance deviations from otherwise universal scaling laws and apparent changes in the gap symmetry. The malleability of Fe-SCs is significant since this is a limiting factor for high-T_c SCs in applications.

1.3 Crystal Structure

There are two major and two minor classes of Fe-SCs. The most studied prototype from each major class is $LaFeAsO_{1-x}F_x$ (from the "1111") and $Ba(Fe_{1-x}Co_x)_2As_2$ (from "122"). And from each minor class is LiFeAs (from "111") and FeSe (from "11"). The Fe-SCs are synthesized using one of three techniques: (1) solid-state reaction and (2) high-pressure synthesis to create polycrystalline samples; or, (3) the flux method to create

large single crystals. All the structures are composed of layers and undergo a tetragonal to orthorhombic symmetry breaking at low temperatures, after which one in-plane axis is compressed ∼1%. The layered geometry gives rises to strong anisotropies.

The common structural motif of Fe-SCs is a square lattice of Fe atoms with pnictogen (As, P) [25] or chalcogenide (Se, Te, S) [26] atoms staggered above and below the center of Fe squares. This arrangement forms FePn_4 tetrahedra. In the high-T tetragonal phase, a and b directions are at 45 ° to the Fe subnet. In the low-T orthorhombic phase, a and b directions coincide with the Fe subnet. The Fe-Fe bonds are metallic, the Fe-As highly covalent, and the intervening layers connected by ionic interactions [14]. A pure FeAs compound, one without blocking layers, is not possible because $FeAs_6$ octahedra rather than $FeAs_4$ tetrahedra are formed [27]. The structural parameters, such as lattice constant a and Fe-As-Fe bond angle, have a direct influence on T_c (see Fig. 1.10c) [28]. In some cases T_c follows this structural tuning. For example, $Ba_{1-x}K_xFe_2As_2$ at low doping [29] or the changes in ReFeAsO with varying Re [18]. On the other hand, $CsFe_2As_2$ has close to ideal tetrahedra but T_c only 2.6 K [30].

The only internal cell parameter is the height of As planes relative to Fe planes (z_{As}). This parameter adjusts the Fe-As bonding, and thus has a strong effect on the observed T_c [28] and electronic structure [31]. The predicted z_{As}, according to DFT, is sensitive to the exchange-correlation (XC) functional and whether magnetic ordering is considered [32]. From Table. 1.1 it is evident only the choice of generalized gradient approximation (GGA) for XC functional and AFM for magnetic ordering produces the experimental z_{As}. Note, however, that the GGA predicted magnetic moment of LaFeAsO is much larger (2 μ_B) [33] than the observed one (0.3 μ_B) [34]. As the cell size can change electron density (i.e., the electrons per unit volume), it can have substantial effects on electron degenerecy, Fermi level, and overall electronic structure. Thus, it is best to take lattice parameters as extracted from X-ray diffraction when performing DFT calculations

The 1111 compounds consist of ReFeAs($O_{1-x}F_x$); $Ae_{1-x}R_x$FeAsF; and $Re_{1-x}Ae_x$FeAsO. The 1111 are formed in the ZrCuSiAs structure with space group $P4/nmm$ at high temperatures and $Cmma$ at low temperatures. The T_c value decreases with the size of the rare-earths; and, concomitantly, the lattice constant a. An alternative to F doping on O sites is to create O vacancies. Both lead to effective electron

	Exp.	GGA-NM		GGA-AF		GGA
	z_{As}	z_{As}	Error (Å)	z_{As}	Error (Å)	μ (calc.)
LaFeAsO	0.6513	0.6375	0.12	0.6478	0.03	2.06 μ_B/Fe
$BaFe_2As_2$	0.3545	0.3448	0.13	0.3520	0.03	1.97 μ_B/Fe
LaFePO	0.6339	0.6225	0.05	0.6254	0.03	0.60 μ_B/Fe

Table 1.1: Predicted z_{As} by varying exchange-correlation and magnetism. After [35].

doping. The 1111 were the first discovered class and usually exhibit the highest T_c for bulk structures, reaching up to 55 K in $SmFeAsO_{0.85}$ [36]. The lattice constants for representative LaFeAsO are $a = 0.4035$ nm, $c = 0.8739$ nm, and internal coordinate $z_{As} = 0.1418$ nm [37]. The 1111 compounds remain difficult to study because available crystals are small and difficult to synthesize [38]. Furthermore, polar states at the surface interfere with ARPES measurements, giving a poor representation of the bulk electronic structure [39]. Also see [12]

The 122 compounds are $Ae(Fe_{1-x}Tm_x)_2As_2$ or $Ae_{1-x}Am_xFe_2As_2$. They form in the $ThCr_2Si_2$ structure and $I4/mmm$ space group, which symmetry breaks to $Fmmm$ at low temperatures. The highest T_c is 38 K in $Ba_{0.6}K_{0.4}Fe_2As_2$. For tetragonal $BaFe_2As_2$, the focus of this thesis, the lattice constants are $a = 0.3917$ nm, $c = 1.3297$ nm, and z_{As} =0.1380 nm [40]. The c-axis is larger than in the 1111; however, the active FeAs layers have nearly the same a. It is the most easily synthesized Fe-SC and dopants are more uniformly distributed [41]. One difficulty is that structural and magnetic twin domain boundaries proliferate throughout the sample [42]. Samples either need to be de-twinned in experiment, or the presence of twins considered in theoretical models. It has even been found twin boundaries act as nucleation sites for SC [43]. In this thesis we consider the formation energetics of twin and other planar defect boundaries in a later chapter.

Both 111 and 11 compounds have a tetragonal $P4/nmm$ structure which reduces to $P2_1/m$ at low-temperatures. They have lower T_c then their 1111 and 122 counterparts, but serve to further delimit the boundaries of SC. Their relatively simple structure also makes synthesis and analysis easier. The 111 are composed of LiFeAs and NaFeAs. These are the best compounds to perform ARPES as they yield large single crystals with a nonpolar surface [44]. They are, however, highly reactive to air, making handling difficult. LiFeAs has a T_c of 18 K. It is unusual for featuring a non-magnetic ground state that superconducts without pressure or doping [45]. And NaFeAs has Neél, nematic, and SC transitions at 52, 41, and 23 K, respectively, in the parent state [46]. The 11 consist of FeS and $FeTe_{1-x}Se_x$ alloys. While T_c is 8 K only, it can be increased dramatically on application of pressure. The limited T_c in these compounds may be a result of reduced two-dimensionality due to a lack of blocking layers.

There is also a more exotic "245" phase, with high magnetic moments (3 μ_B) and a high Néel temperature (500 K) [47]. The motif of the spacer layers can be complex, e.g., $(Sr_3S_2O_5)Fe_2As_2$ or $Sr_4V_2O_6Fe_2P_2$. A T_c of 37 K is close to the maximum for 122 compounds. They are either observed to be insulating or semimetallic down to 100 K. However, this has been distinguished as a result of phase separation of metallic and AFM insulating regions [48]. Due to their complexity and similarity to 122 compounds, these are not frequently studied.

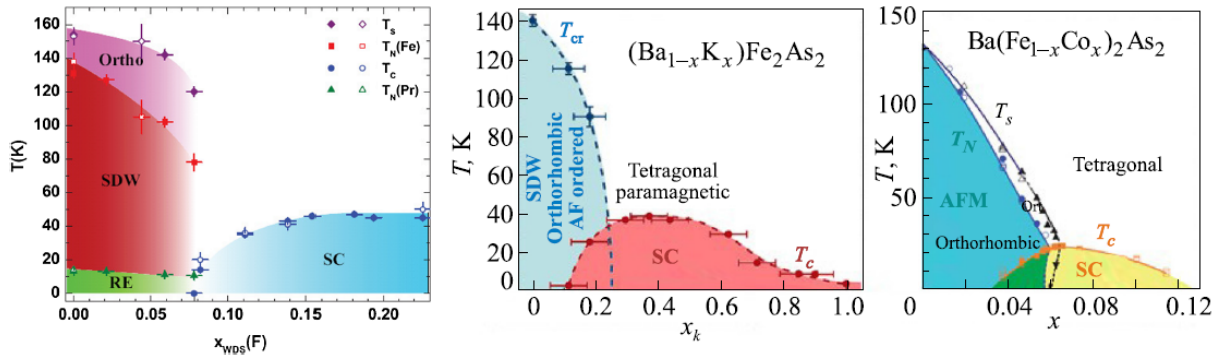

Figure 1.4: Phase diagrams of $PrFeAsO_{1-x}F_x$ [51], $(Ba_{1-x}K_x)Fe_2As_2$ [52], and $Ba(Fe_{1-x}Co_x)_2As_2$ [53].

1.4 Phase Diagram

The SC transition is identified by a drop in electrical resistance, an increase in diamagnetic response, and a peak in magnetic susceptibility $d\chi/dT$ (see [18]). The Fe-SCs feature a variety of tuning parameters; including chemical doping, hydrostatic and uniaxial pressure, and vacancy formation. Unlike the Cu-SCs, all atomic sites can be doped, including within active As-Fe-As tri-layers. Substituting Fe for magnetic ions Mn or Cr is disruptive to SC, while substitution by Co or Ni enhances it. Substitution of the alkali earth site is common, especially as hole doped $Ba_{1-x}K_xFe_2As_2$. Less commonly, rare-earth substitution is possible; for example, $Gd_{1-x}Th_xFeAsO$ for electron doping [49] and $La_{1-x}Sr_xFe_2As_2$ for hole doping [50]. The sign of the charge carriers can be checked by examining the Hall coefficient.

Both the 1111 and 122 are orthorhombic, AFM metals in their parent ground-state. Spins are aligned along the shortened b axis and antialigned along a and c (see Fig. 1.3). The presence of insulating layers reduces coupling in the c direction and spin fluctuations are easily excited in this direction [35]. As the electrons are itinerant, the AFM state is also called a spin-density wave (SDW); in analogy with the magnetic state of Cr alloys [54]. For LaFeAsO the structural transition (155 K) proceeds the Neél transition (137 K) [55]. The same is true for other 1111 compounds. It is interesting to note the rare-earth ions exhibit their own magnetic ordering at lower temperatures (see Fig. 1.4), for example at 6 K in SmFeAsO [56]. This additional magnetic order persists in the SC phase and there is no indication these f electrons play a role in SC. For $BaFe_2As_2$ the structural and Néel transition occur simultaneously (140 K), and the same is true for other 122 compounds.

Fluorine doping of LaFeAsO results in a slight reduction in T_N until the onset of SC, after which no Néel phase persists. By contrast, in $CeFeAsO_{1-x}F_x$ the T_N drops continuously to zero before the onset of SC [58]. And in $SmFeAsO_{1-x}F_x$ there is a concentration range in which both phases coexist [59], though perhaps

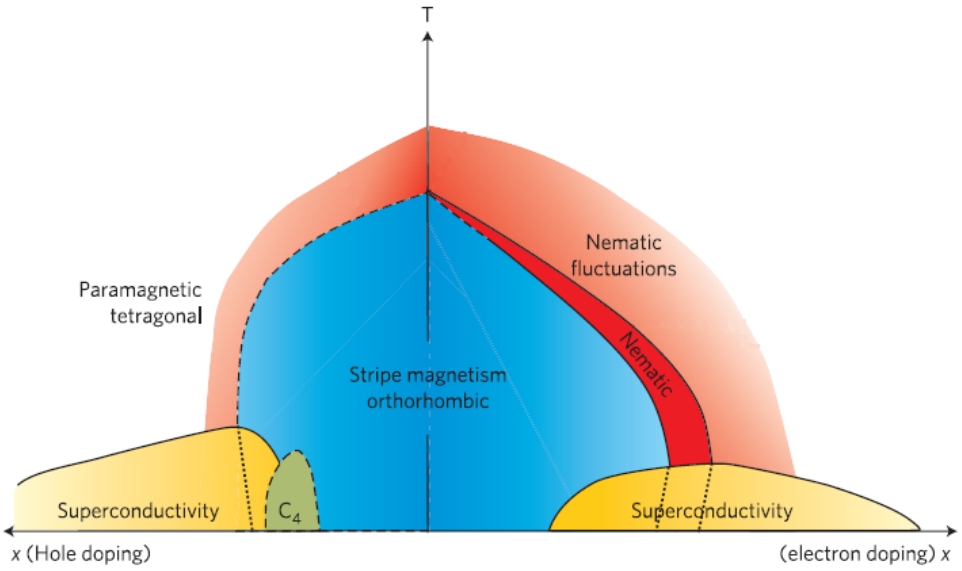

Figure 1.5: Cartoon phase diagram of electron and hole doped 122 SCs. After [57].

not microscopically. All the 122 compounds show a gradual reduction of T_N on doping and a max T_c near the AFM quench point (see Fig. 1.4 and Fig. 1.5), with a coexistence region between both phases. Hole-doped $(Ba_{1-x}K_x)Fe_2As_2$ samples show phase separation at the nanometer scale [60]. While electron-doped $Ba(Fe_{1-x}Co_x)_2As_2$ is known to be coexistent down to the subnanometer scale [61]. In $Ba(Fe_{1-x}Tm_x)_2As_2$ (Tm=Co, Ni) the SDW also becomes incommensurate in this coexistence region, emphasizing the itinerancy of electrons [62]. Electron doping is known to rapidly suppresses spin coupling along the c-axis [63]. Notably, isovalent substitutions can also induce SC; for example, $BaFe_2(As_{1-x}P_x)_2$ reaches $T_c = 30$ K [64]. In this case stearic effects play a role and a comparison can be made to pressure effects.

There is an approximate symmetry between phase diagrams on hole and electron doping of 122 compounds, signaling loss of AFM and stearic effects are one of the key drivers. The proximity of the AFM quench point to max T_c on both sides strongly suggests pairing is mediated by AFM spin fluctuations. In $Ba(Fe_{1-x}Co_x)_2As_2$ the structural and AFM transitions become split and second order, as is the case with many of the 1111 compounds as well. However, in $Ba_{1-x}K_xFe_2As_2$ the two transitions remained tied and first order, also true on applying hydrostatic pressure. At heavy hole doping, as in KFe_2As_2, the nature of SC may be changed. For example the gap acquires additional nodes and the symmetry appears to change from $s^{\pm}$ to d [65, 66]. This is not unlike how multiple SC phases were identified in UPt_3. For heavy electron doping the SC phase is lost altogether.

The nematic phase transition associated with the orthorhombic distortion and Néel transition has been of particular interest [57]. The Ising-like nematic order refers to breaking of the 90 ° lattice rotational symmetry

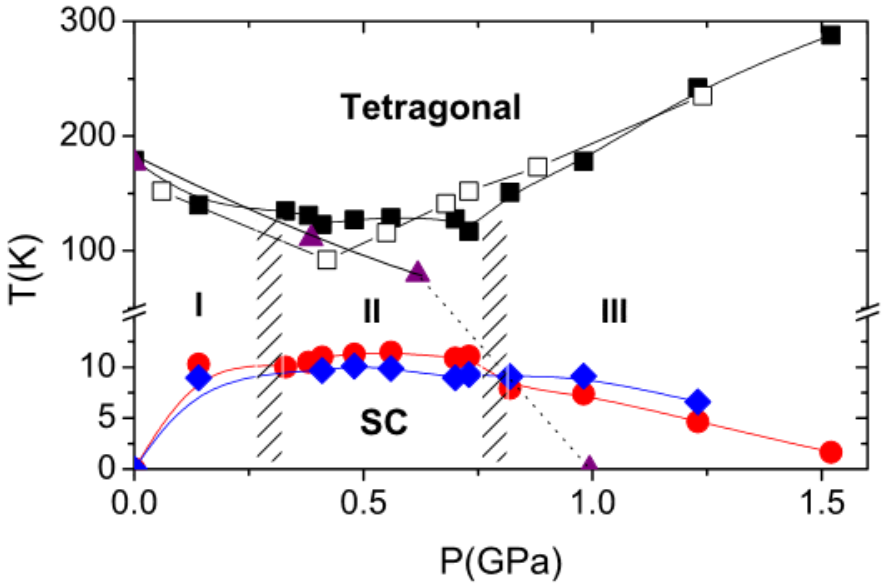

Figure 1.6: Phase diagrams of $CaFe_2As_2$. Regions I and III correspond to a orthorhombic and collapsed tetragonal phase respectively. Region II is a coexistence of I and III. After [71].

while preserving time-reversal symmetry. As noted, in-plane disorder disrupts this transition, splitting the structural and Néel pieces and making it second order. It is unlikely to be driven by soft phonon modes because strong in-plane anisotropies of the electrical properties are detected above the transition. There are two possible electronic mechanisms: orbital fluctuations and spin fluctuations. Clarifying which is the primary order parameter would suggest which mechanism is more likely responsible for Cooper pairing. Orbital fluctuations favor an s^{++} gap symmetry. In other words a gap that preserves sign throughout the Brillouin zone. AFM spin fluctuations would favor an $s^{\pm}$ gap symmetry, or a change in sign by translation of (π, π) in **k**-space. AFM fluctuations have been detected well above the nematic transition [67]. Calculations and observations of the Drude weight [68, 69] and magnetic scattering rate [70] lend strong support for an $s^{\pm}$ scenario. Below T_c there is a strong suppression of the orthorhombic distortion, suggesting the nematic and SC electronic effects compete with each other. Nematic ordering also plays a role in Cu-SCs and and heavy fermion compounds.

Application of either hydrostatic or uniaxial pressure can induce SC. Modest pressure reduces the a lattice constant, with optimal doping tending to be near perfect $FeAs_4$ tetrahedra. Decreasing a increases Fe and As hybridization and inhibits magnetism [72]. T_c increases with pressure only if sample is underdoped, suggesting a connection between doping and pressure [73]. Pressure experiments under different conditions yield different results [74, 75, 76] due to the sensitivity of samples to anisotropic pressures. A maximum T_c is achieved at 28 kbar in $SrFe_2As_2$ and 35 kbar in $BaFe_2As_2$ [74]. In $CaFe_2As_2$, above 0.35 GPa, there is a

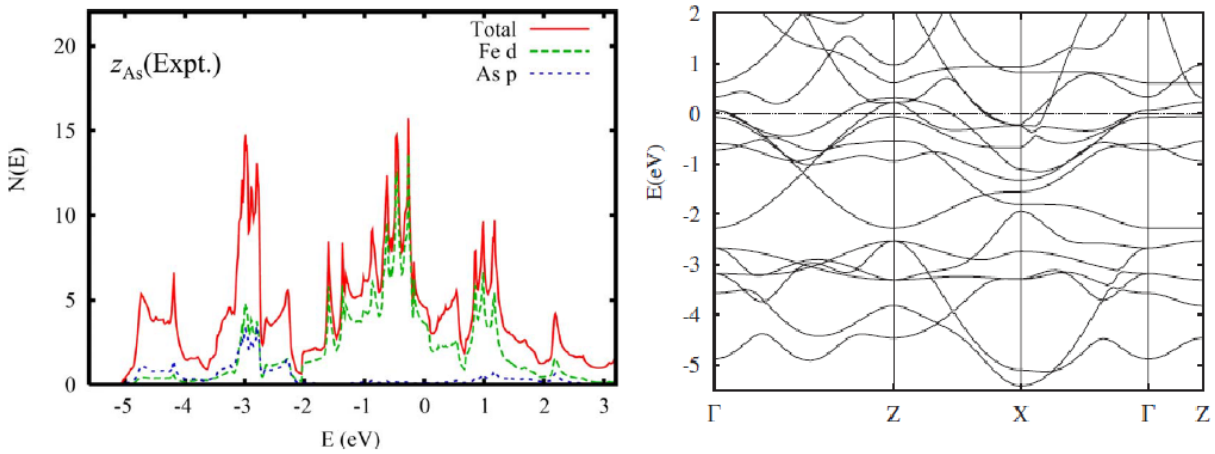

Figure 1.7: Density of states and band structure of $BaFe_2As_2$. After [31].

dramatic (∼5%) reduction in volume into a "collapsed" tetragonal phase [77] (see Fig. 1.6). The magnetic ordering vanishes at the onset of this phase, which calculations support.

A general theme is that T_c improves with fewer interactions along the c-axis, or as the electronic character becomes more two-dimensional. It also improves as magnetic effects are inhibited by shrinking the lattice or shifting the Fermi level. Also, SC has been linked to a loss of a 3D Fermi hole pocket [78].

1.5 Electronic Structure

Superconductivity and magnetism can be traced to interactions of electrons near the Fermi surface (FS). Thus the electronic structure is a key determinant in understanding the origins of magnetic and SC phases.

The valence states are formed from a hybridization of Fe $3d^5$ and As $4p^3$ electrons. The Fe d are at higher energies than As p. Further, only Fe d orbitals contribute at the Fermi level (see Fig. 1.7). Theoretical models require all Fe d orbitals [79] in order to get an electronic structure that qualitatively resembles that observed from ARPES [39, 80, 81], or calculated in DFT [31, 82]. The 1111 and 122 compounds show a low carrier concentration and high density of states (DOS) [82]. The DFT DOS at the Fermi level for $BaFe_2As_2$ is 1.53 eV/Fe [31] and for LaFeAsO is 1.31 eV/Fe [82]. Those values are sufficient to indicate a Stoner-like magnetic instability, as is observed. A simple correlation between DOS and T_c does not work, as might be expected from BCS theory. For example, in $Ba_{1-x}K_xFe_2As_2$ the Fermi level DOS is not peaked at optimal doping [12].

The band structure and Fermi surface can be described according to simplified 2D or full 3D models. The Brillouin zones (BZ) are different for each and both are depicted in Fig. 1.8. In 2D models one can also choose whether the unit cell contains one or two Fe atoms. Due to the staggered position of As atoms,

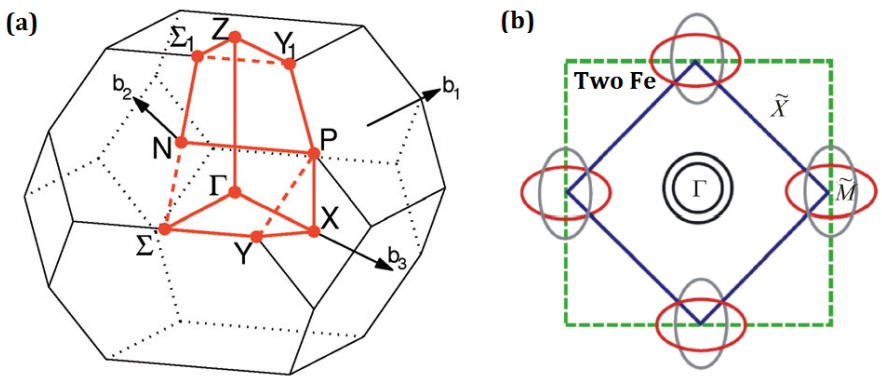

Figure 1.8: (a) 3D BZ of body-centered tetragonal lattice. After [83]. (b) 2D BZ for 2 Fe-atom unit cell along with cartoon Fermi surfaces. Note the similarity to calculated 3D Fermi surfaces in Fig. 1.9. After [84].

the proper unit cell contains two Fe atoms, though these atoms are connected by an inversion symmetry. Theoretical considerations using low-energy model Hamiltonians often favor a simplified one Fe per site and its corresponding (extended) Brillouin zone (BZ). Arsenic atoms may be removed by folding them into an effective Fe-Fe next nearest neighbor interaction. A conversion between the extended and folded BZ (i.e., the 2 Fe BZ) is necessary in order to compare experimental, computational, and theoretical works. This is accomplished by translating the extended BZ Fermi surface by the reciprocal lattice vectors of the folded BZ.

The Brillouin zone has a strong influence on the Fermi surface and what symmetries may be present (see Fig. 1.8a). The key high symmetry positions are Γ at the center, X at the center of square faces, and Z at the center of top face (i.e. along k_z). The Fermi surface of the NM parent compounds $BaFe_2As_2$ and LaFeAsO are presented in an extended BZ scheme in Fig. 1.9. There are two electron cylinders at the X point and two or more hole sheets at Γ point. The number and shape of the hole sheets are sensitive to the internal cell parameter z_{As}. The hole sheets are often warped in the k_z direction, emphasizing these compounds are more three-dimensional than Cu-SCs. Around Γ one or more of the hole cylinders is pinched. It is possible even that one of the holes becomes an ellipsoid about Z depending on pressure and doping. The electron and hole cylinders are of d_{xz} and d_{yz} character and the fraction of each is angle dependent. Any hole pocket at Z is of d_{z^2} character. The small, compensated volumes of the Fermi surfaces result in low carrier concentrations. In 122 compounds the hole and electron volumes, which are proportional to carrier density, are equal [81]. This Fermiology can be modified with a rigid-band Fermi level shift, reproducing the effects of low-doping for some carrier types (e.g., $Ba(Fe_{1-x}Co_x)_2As_2$ [85]). The calculated FS gave the first suggestion of the *s*-wave pairing symmetry [82]. Thus, the ES of Fe-SCs is complex, with multiple bands

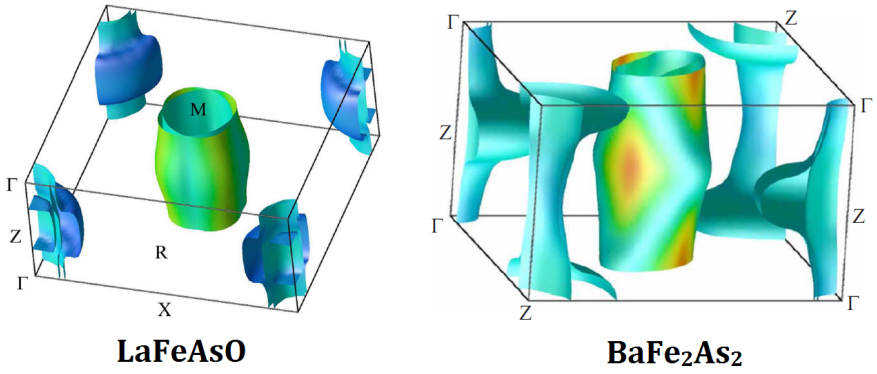

Figure 1.9: Fermi surfaces for LaFeAsO and $BaFe_2As_2$. After [31, 82].

and three dimensionality, in contrast to the Cu-SCs.

There is a strong Fermi surface nesting at the (π, π) wave vector connecting Γ and X points, which corresponds to the observed AFM ground-state. The nesting causes a SDW instability because electrons can lower their kinetic energy, a so-called "Peierls" transition [86]. The nesting also emphasizes the itinerant character of the magnetism. Furthermore, when nesting is clearly visible, a SDW ground-state is usually present [85]. And when nesting is absent, as in LiFeAs, magnetic ordering is absent [45]. Nesting also properly describes an incommensurate splitting of the SDW in $Ba(Fe_{1-x}Co_x)_2As_2$ [62]. It has even been suggested the disruption of Fermi surface nesting, and thus a suppression of SDW state, might be more important to onset of SC on carrier doping than Fermi level shifts [14]. On the other hand, FeTe, while maintaining strong spin fluctuations at the (π, π) mode, shows a different ground-state magnetic ordering [87]. A perfectly itinerant picture is, however, not entirely accurate either. Measurements of the magnetic susceptibility show large dispersion in k-space for $CaFe_2As_2$ [88]. Local Heisenberg J_1-J_2 models, while capable of correctly predicting the ground-state AFM ordering, cannot fully explain measured magnetic excitations [89]. The correct picture is likely intermediate to these two.

On electron doping the electron cylinders about X grow and the hole cylinders about Γ and Z shrink. The onset of SC with electron doping has been tied to the disappearance of a Fermi hole pocket at Z, as visible in ARPES for $Ba(Fe_{1-x}Co_x)_2As_2$) [78]. The presence of this hole is sensitive to the pnictogen height, possibly explaining the connection of As-Fe-As bond angle to T_c. A topological change in the Fermi surface is known as a "Lifshitz" transition. On hole doping $Ba_{1-x}K_xFe_2As_2$ the electron cylinders shrink and hole cylinders grow. At some critical concentration the electron cylinders disappear and are replaced by four lobes centered about the X point [90]. A major result of this thesis is characterizing this Lifshitz transition and its connection to a change in the SC phase.

The calculated and experimentally resolved bands are not in perfect agreement. Fitting the calculated

bands requires three times renormalization and shifts of about ∼40 meV [91, 45]. This suggests modest electron correlations are present.

1.6 Magnetism and Correlations

The ground-state magnetic ordering corresponds to a (π, π) commensurate spin wave as confirmed by ARPES and corroborated in DFT. The Néel transition occurs at relatively low temperatures ($T_N \sim 150$ K). The (π, π) ordering is just what would be expected based on arguments of itinerant electrons driven by Fermi surface nesting. It also well explains a transverse splitting in the SDW wave vector that is observed in $Ba(Fe_{1-x}Co_x)_2As_2$ [62] and suspected in $Ba_{1-x}K_xFe_2As_2$ [92].

However the presence of local moments at temperatures well above the Néel transition in the paramagnetic phase suggests correlations may be larger than anticipated [93]. Unusually, DFT predicts much larger moments than observed. Most DFT predictions for the moment are 2 μ_B, which is line with the paramagnetic fluctuating moment. However, observed ordered moments can be much smaller, for example 0.35 μ_B in LaFeAsO [94] or 0.87 μ_B in $BaFe_2As_2$ [95]. And the observed fluctuating moment in $BaFe_2As_2$ of $\langle m^2 \rangle = 3.2$ [96] is larger than expected from an itinerant SDW model based on the random phase approximation [97]. Quasiparticle mass enhancements due to Coulomb correlation follow the reduction in moments well [98]. The mass enhancement's are explained as a kinetic frustration between direct Fe-Fe hopping and indirect hopping via As atoms. There is especially a sensitivity of magnetic moments to hybridization of Fe and As atoms [72]. Hartree-Fock approximations to the Hubbard model show there is an intermediate regime, for Hubbard U and bandwidth W with $U/W = 0.3 - 0.4$, for which the materials are both metallic and magnetic [99, 100]. Purely local models for J_1-J_2 show values, indeed even signs, that are inconsistent across the spectrum of Fe-SCs [101, 102, 103].

There is much interest in spin excitations because the dominant feeling is that Cooper pairing is mediated by spin fluctuations. Indeed, a correlation between the spectral weight of spin dynamics and SC is found. For overdoped $Ba(Fe_{1-x}Co_x)_2As_2$ [104] and $LaFeAsO_{1-x}F_x$ [105] the disappearance of SC and spin fluctuations occur together. Moreover, in the SC phase, a resonance peak appears [106, 107]. This is also taken as strong evidence for a sign change in the order parameter on translation from hole to electron pockets.[108]

1.7 Gap Symmetry

Determining the gap symmetry has been a major concern of Fe-SC researchers. The symmetry restricts the nature of the pairing interaction. For further details on what is meant by the gap symmetry, consult the

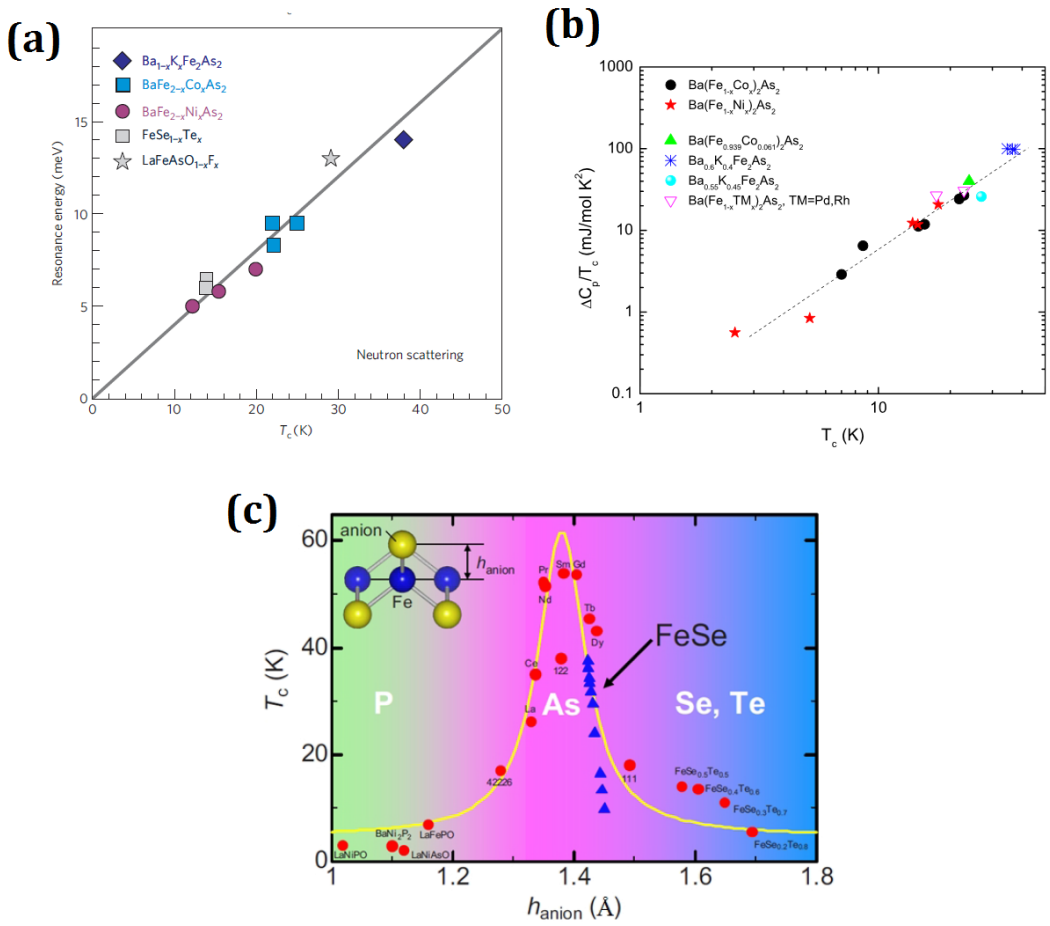

Figure 1.10: Universal scaling of T_c and (a) neutron scattering resonance, (b) specific heat, and (c) pnictogen height. After [14, 109, 110] respectively.

appendix. In Cu-SCs the phase sensitive Josephson junction experiments have conclusively established the gap is "d"-wave. On the other hand, for Fe-SCs a lack of half-integer flux by superconducting quantum interference (SQUID) rules out an all d-wave scenario [111]. Further, ARPES experiments find nearly isotropic gaps about both the hole and electron cylinders. In $Ba_{1-x}K_xFe_2As_2$ these gaps are 10 meV, except for the outer hole sheet, which is 4 meV [112]. It has been argued that if AFM spin fluctuations mediate pairing then the gap symmetry must be "$s^{\pm}$," meaning a sign change on translation by (π, π) in $\mathbf{k}$-space [82].

1.8 Universal Scaling Laws

There are three quantities that correlate strongly to T_c. The first is the As-Fe-As bond angle, with optimal doping tending to be near ideal tetrahedra, which minimize the crystal field splitting of the Fe atom [28]. In addition, there is a universal scaling law between specific heat and T_c: the so-called "Bud'ko-Ni-Canfield" scaling, or specific heat jump $\Delta C_S \propto T_c^3$ [109]. Finally the energy of the magnetic resonance in neutron scattering data scales linearly with T_c [14]. These are shown together in Fig. 1.10.

1.9 Issues to Address

The DFT studies performed thus far have focused on the parent compounds. The few computational studies on the effects of chemical doping have been approximated by (1) a rigid-band model, (2) fractional nuclear charge on an atom, (3) the Virtual Crystal Approximation (VCA), or (4) a supercell that contains a large dopant concentration (i.e., one or two dopant atoms) in a unit cell. These models vary in degree of sophistication, but they all suffer the deficiency that they use a periodic crystal potential to simulate disorder and ignore potentially relevant physics dictating dispersion. The resulting sharp Fermi surfaces are equivalent to an ordered crystal. In reality, the **k**-space resolved density of states, or Bloch spectral function $A(\mathbf{k}, E)$, should exhibit dispersed $E_n(\mathbf{k})$, with a width related to the finite electron state lifetimes. Disorder broadening of the dispersion can affect (and enhance) Fermi-surface nesting and, therefore, magnetic SDW instabilities. Notably, the first three approximations are severe regarding disorder effects on the electronic-structure.

DFT has proven well in reproducing the electronic structure and Fermi surfaces of Fe-SCs, especially when compared to ARPES and quantum oscillation. It also correctly predicts the ground-state magnetic ordering, including for end compounds that do not SC or have different magnetic orderings. Thus, there is an evolution of the phase stability and only calculations of the intermediate alloy will demarcate where changes take place. These changes in phase stability are not frequently discussed but plague sample preparation. Elucidating their origin can aid experimentalists better understand the sources of their difficulty.

It is believed that magnetic and SC instabilities arise from the Fermi surface nesting and Lifshitz transitions. As the Fermi surface evolves with tuning parameters, such as chemical doping and pressure, these instabilities are affected. A DFT study on the evolution of the Fermi surface with doping helps better tie the key transition points in the phase diagram with the electronic structure. While ARPES experiments can assist in this regard, they are comparatively slow to perform, can be affected by inhomogeneities near the surface, and are difficult to interpret due to the relatively low quality of measurements in Fe-SCs.

In this thesis we tackle the prominent electron doped $Ba(Fe_{1-x}Co_x)_2As_2$ and hole doped $Ba_{1-x}K_xFe_2As_2$ using the CPA to simulate chemical and magnetic disorder. We examine the evolution of the Fermi surface, including Lifshitz transitions, and how Fermi surface nesting is affected. We see where the rigid-band begins to fail and a proper alloying theory is necessary. We also check the stability of phases against magnetism and chemical segregation. Finally, we investigate the presence of low-energy spin excitations. These bear a strong influence on the nematic transition and spin fluctuations necessary for pairing.

Chapter 2

Computational Methods

In this chapter a description is given of the computational methods used in this thesis. This includes density-functional theory, multiple-scattering theory, and the coherent potential approximation.

2.1 Density Functional Theory

2.1.1 Problem Statement

Solid state physics and quantum chemistry problems ultimately seek to solve the time-independent Schrödinger equation describing the motion of nuclei and electrons. Explicitly this is written

$$H\Psi(\mathbf{R_1}, \mathbf{R_2}, ..., \mathbf{R_N}; \mathbf{r_1}, \mathbf{r_2}, ..., \mathbf{r_n}) = E\Psi(\mathbf{R_1}, \mathbf{R_2}, ..., \mathbf{R_N}; \mathbf{r_1}, \mathbf{r_2}, ..., \mathbf{r_n}) \tag{2.1}$$

where $\mathbf{R_1}, ..., \mathbf{R_N}$ and $r_1, ..., r_n$ specify the coordinates of ions and electrons respectively. The Hamiltonian H is given, for Z_I the charge of the Ith ion, by

$$H = -\sum_I \frac{\nabla_I^2}{2M} - \sum_i \frac{\nabla_i^2}{2m} + \sum_{i,j} \frac{e^2}{r_i - r_j} - \sum_{i,I} \frac{eZ_I}{r_i - R_I} + \sum_{I,J} \frac{Z_I Z_J}{R_I - R_J} \tag{2.2}$$

where I and i refer to ion and electron indices respectively. This equation is exactly solvable only for the hydrogen atom. The first simplification is the Born-Oppenheimer approximation; i.e., to treat the ion coordinates as fixed when solving for the electronic degrees of freedom. This is possible because the heavy ions have a much slower response than electrons to perturbations. Later, if needed, the ground-state energy from the electronic problem can be fed as an effective potential in a reduced Schrödinger equation for the ionic degrees of freedom. The Born-Oppenheimer approximation is rarely considered the limiting factor in solid-state physics problems, including superconductivity. Often the ionic degrees of freedom are spatially localized and their positions ascertained by X-ray diffraction.

Solving for the electronic degrees of freedom under the Born-Oppenheimer approximation still presents a

formidable challenge. One approach is to employ the variational principle with a complicated, parametrized wave-function in an attempt to account for both exchange and correlation effects of electrons. This is used in quantum Monte Carlo but is computationally demanding. Only at most a few electrons can be solved for this way. Another approach is to use the variational principle under the assumption the electrons can be described as a Slater determinant of single-particle orbitals. This leads to the popular Hartree-Fock scheme. Here, however, we make use of an alternate reduction of the electronic problem by expressing it explicitly in terms of the electron *density*.

2.1.2 Hohenberg-Kohn Theorems

Density functional theory (DFT) draws its foundations from two theorems formulated by Hohenberg and Kohn. The first states that the external potential $V_{\text{ext}}(\mathbf{r})$, i.e., the Coulomb field of the ions, is a unique functional of $\rho(\mathbf{r})$, the ground-state electron density. The proof, again omitted, uses the variational principle. Because it is clear $V_{\text{ext}}(\mathbf{r})$ fixes the entire problem statement, we can write any physical property, in particular the ground-state wave function, as a functional of the ground-state density. For example we can write the ground state energy is

$$E[\rho] = \int V_{\text{ext}}(\mathbf{r})\rho(\mathbf{r})d\mathbf{r} + \int \frac{\rho(\mathbf{r})\rho(\mathbf{r}')}{|\mathbf{r}-\mathbf{r}'|}d\mathbf{r}d\mathbf{r}' + F[\rho], \tag{2.3}$$

where $F[\rho]$ is a unique functional that embodies all unaccounted effects, including exchange and correlation.

The second theorem states that, if $V_{\text{ext}}(\mathbf{r})$ is held fixed in Eq. (2.3), then only the true ground state density will yield a minimum energy. The proof, which we omit, is again based on the variational principle. The outcome, importantly, for a N electrons, is the variational result that $\delta[E[\rho] - \mu N]/\delta\rho = 0$, where μ is the electronic chemical potential. This variational principle permits a practical, self-consistent solution for the ground-state density if $F[\rho]$ were known. While it is unlikely an exact form for $F[\rho]$ will be found, it can be approximated. A leading guess starts by solving the free electron gas for a uniform density ρ_0. This gives the solution $F[\rho_0] = Q[\rho_0]$, where $Q[\rho_0]$ is an ordinary function of ρ_0. The approximation is then to take $F[\rho(\mathbf{r})] \cong \int Q[\rho(\mathbf{r})]d\mathbf{r}$, a sum of correlations based on the local density. This leads to the so-called *local density approximation*. Other, more sophisticated, approximations exist. A popular one is the *generalized gradient approximation*, which attempts a correction for gradients in the electron density.

2.2 Multiple Scattering Theory

2.2.1 Greens Functions

The single particle Greens function $G(E, \mathbf{r}, \mathbf{r}')$ of a molecule or solid gives a satisfying and complete solution to the electronic structure problem. Important physical properties are obtained by simple operations on G. For example, the position-resolved density of states is

$$n(E, \mathbf{r}) = -\frac{1}{\pi}\lim_{\eta\to 0^+}\mathrm{Im}\, G(E + i\eta, \mathbf{r}, \mathbf{r}).$$

Integrating over energy gives the charge density $\rho(\mathbf{r}) = -e\int_{-\infty}^{\mu} n(E, \mathbf{r})dE$. And integrating over $\mathbf{r}$ gives the density of states $n(E) = \int n(E, \mathbf{r})d\mathbf{r}$. For an ordered crystal the Greens function takes the form $G(E, \mathbf{R} + \mathbf{r}, \mathbf{R}' + \mathbf{r}')$ where $\mathbf{R}, \mathbf{R}'$ are Bravais vectors and $\mathbf{r}, \mathbf{r}'$ are now limited to the central unit cell. A lattice Fourier transform then yields $G(E, \mathbf{k}; \mathbf{r}, \mathbf{r}')\delta_{\mathbf{k}\mathbf{k}'}$ for vectors $\mathbf{k}, \mathbf{k}'$ in the Brillouin zone. The poles of $G(E, \mathbf{k})$ reveal the electronic dispersion (or band structure for ordered case) $E = E_n(\mathbf{k})$ of the solid. $G(E, \mathbf{k})$ is the basis for numerous properties, including the DC conductivity and susceptibilities (magnetic and chemical short-range order). In addition to its close relation to observables, the Greens function also plays an important role in advanced approximation schemes for substitutionally-disordered solids. Thus, an electronic structure code built on Greens functions is an effective means to solving the electronic structure problem.

2.2.2 Fundamental Equations

Multiple-scattering theory (MST) relates the Greens function of a solid (or molecule) to the electron scattering occurring at each atom. To express this precisely the volume of the solid has to be partitioned into space-filling, convex Voronoi polyhedra (VP); each one centered about one atomic nucleus. A natural VP choice for a monatomic crystal is the geometrically-defined Wigner-Seitz cell. This partitioning defines a decomposition of the effective, one-electron crystal potential $V(\mathbf{r})$ into sub-potentials $V^n(\mathbf{r}) \equiv V(\mathbf{r})\Omega^n(\mathbf{r})$, where $\Omega^n(\mathbf{r})$ is one inside the nth cell and zero otherwise. Each $V^n(\mathbf{r})$ is treated as an independent "site" for electron scattering. In real applications care must be taken that $V^n(\mathbf{r})$ is determined predominantly by the charge of the nth atom it encloses, not those of its neighbors. A poor partition has the consequence that basis-set expansions will require a large number of basis functions [a large cutoff, e.g., $L_{\mathrm{Max}} = (\ell m)$ for spherical harmonic $Y_{\ell m}(\Omega)$] to get accurate results. The scattering off the nth cell is described by the

single-site scattering matrix

$$\mathbf{t}^n(E,\mathbf{r},\mathbf{r}') \equiv V^n(\mathbf{r}) + \int d\mathbf{r}'' V^n(\mathbf{r}) g(E,\mathbf{r},\mathbf{r}'') \mathbf{t}^n(E,\mathbf{r}'',\mathbf{r}'),$$

where $g(E,\mathbf{r},\mathbf{r}')$ is the free-particle propagator. This matrix is closely related to the canonical on-shell scattering matrix $\mathbf{S}(E,\mathbf{p},\mathbf{p}')$. Because $V^n(\mathbf{r})$ has strong contributions from the core of the nth atom, it is expected to be almost spherical about the atomic site $\mathbf{R}^n$. This permits the theory to draw on a large body of knowledge from single-site scattering theory to determine $\mathbf{t}^n$.

Multiple scattering theory collects each $\mathbf{t}^n$ in the *scattering path operator* (SPO)

$$\tau^{nm}_{LL'}(\mathbf{k},E) = [(\mathbf{t}(E)^{-1} - \mathbf{g}(\mathbf{k},E))^{-1}]^{nm}_{LL'}, \tag{2.4}$$

where n,m are site indices; matrices are expressed in angular momentum basis $L = (\ell m), L'$; $[\mathbf{t}] \equiv \delta_{nm}\mathbf{t}^n_{LL'}$ and $\mathbf{g}(\mathbf{k},E)$ is the Fourier transform of free-electron propagator

$$g^{nm}_{LL'}(E) = \delta_{nm} \int\int d\mathbf{r} d\mathbf{r}' J^n_L(E,\mathbf{r}) \frac{-e^{i\sqrt{E}|\mathbf{r}-\mathbf{r}'|}}{4\pi|\mathbf{r}-\mathbf{r}'|} J^m_{L'}(E,\mathbf{r}')\,,$$

for $J^n_L(E,\mathbf{r})$ a spherical Bessel wave with angular momentum L emanating from the nth site. The physical interpretation of the SPO is to transform an incoming electron wave on the mth site to an outgoing wave at the nth site. The complete Greens function can be expressed in terms of it as

$$G^{nm}(E,\mathbf{k};\mathbf{r},\mathbf{r}') = -\delta_{nm}\Sigma_L Z^n_L(E,\mathbf{r}_<) U^n_L(E,\mathbf{r}_>) + \Sigma_{LL'} Z^n_L(E,\mathbf{r}) \tau^{nm}_{LL'}(\mathbf{k},E) Z^m_{L'}(E,\mathbf{r}')\,,$$

where $Z^n_L(E,\mathbf{r}), U^n_L(E,\mathbf{r})$ are regular and irregular solutions of the Schrödinger equation with potential $V^n(\mathbf{r})$ that satisfy L-dependent boundary conditions. Bloch waves solutions exist wherever $G(E,\mathbf{k})$ has a pole, or

$$||\mathbf{t}(E)^{-1} - \mathbf{g}(\mathbf{k},E)|| = 0\,. \tag{2.5}$$

Korringa first derived this band structure equation from an "exact" band theory (infinite basis) and Kohn and Rostoker via a variational approach, permitting Rayleigh-Ritz based calculations. Thus, MST [embodied in Eqs. (2.4) and (2.5)] is often referred to as the constant-energy KKR method.

Note that, for a given energy E, the Green's function solutions for all $\mathbf{k}$ are obtained. So, no information regarding *unoccupied* or other *occupied* states are required for a full solution. This constant-E KKR approach is distinguished from standard band-structure (spectral) methods, including KKR, that use

constant-**k** searches for all eigenvalues. In such a case, all occupied states plus a large range of unoccupied states are necessary for a complete basis set. Thus, for Fermi surface studies, we only need calculate the KKR Green's function at one energy – the chemical potential, i.e.. the Fermi energy at zero Kelvin.

2.2.3 Self-consistency

The fundamental equation of MST expects an effective, one-electron potential $V_{\text{in}}(\mathbf{r})$ as input. Initially this is taken as a guess and the potential $V_{\text{out}}(\mathbf{r})$ reconstructed from the resulting charge density $\rho_{\text{out}}(\mathbf{r})$ does not match $V_{\text{in}}(\mathbf{r})$. To achieve a potential that has this self-consistency the MST approach has to be iterated over the output potentials.

According to DFT, $V_{\text{out}}(\mathbf{r})$ can be reconstructed as a functional of $\rho_{\text{out}}(\mathbf{r})$. In particular $V_{\text{out}}[\rho] = V_{Ze} + V_{ee}[\rho] + V_{\text{xc}}[\rho]$ where the terms are nuclear-electron, electron-electron, and exchange-correlation functionals respectively. As mentioned, $\rho(\mathbf{r}) = \frac{e}{\pi}\text{Im}\int_{-\infty}^{\mu} G(E,\mathbf{r},\mathbf{r})dE$. Substitution of the fundamental equation of MST gives

$$\rho(\mathbf{r}) = \frac{e}{\pi}\text{Im}\int_{-\infty}^{\mu}\{-\Sigma_L Z_L^n(E,\mathbf{r}_<)U_L^n(E,\mathbf{r}_>) + \Sigma_{LL'} Z_L^n(E,\mathbf{r})\tau_{LL'}^{nn}(\mathbf{k},E)Z_{L'}^n(E,\mathbf{r})\}dE$$

when $\mathbf{r} \in \Omega^n$ and where for solids $\tau_{LL'}^{nn}(E) = \frac{1}{N}\Sigma_{\mathbf{k}}\tau_{LL'}^{nn}(\mathbf{k},E)$ is computed as a BZ average. Thus, numerical integration over **k**-space must be performed for every sample point E in the energy integration. Being a Green function, $G(E)$ is analytic in for complex E (it is Herglotz) and decays exponentially in the positive imaginary half-plane of E. Distorting the energy contour (e.g., contour integration via semicircular numerical grid starting from the bottom of valence band to Fermi level) takes advantage of this so fewer E samples are needed.

2.2.4 Coherent-Potential Approximation

The proper way to handle disordered materials is to average the Greens function over all possible configurations. For solid-state materials the number of configurations grows exponentially with sample size, making such a brute-force strategy beyond the reach of quantum simulations. The usual mean-field approximations involve representing the ensemble by an effective medium. An advantage of MST is that it can naturally accommodate such a medium. Consider that for a substitutionally-disordered solid, like metallic alloys or doped superconductors, the underlying crystal lattice positions $\{\mathbf{R}^n\}$ remain well-defined. As the free propagator $\mathbf{g}(\mathbf{k},E)$ depends only on the $\{\mathbf{R}^n\}$, it does not need modification. The focus lies on how to choose a $\mathbf{t}$(E) so that it adequately describes and effective medium. Consider the alloy *CuAu* in the face-centered

cubic (FCC) structure, with probability of Cu (Au) on any site being $c_{\rm Cu}$ ($c_{\rm Au}$), although inhomogeneous distributions in a complex unit cell can be handled too.

The *coherent potential approximation* (CPA) [113, 114] demands a self-consistency criterion for $\mathbf{t}_C(E)$. Consider three crystals: one with scattering $\mathbf{t}_C(E)$ on every site, one with scattering $\mathbf{t}_{\rm Cu}(E)$ on a central site and $\mathbf{t}_C(E)$ on all the others, and a third with a $\mathbf{t}_{\rm Au}(E)$ impurity instead. The CPA demands that the average of the SPO associated for the impurity is the same for the SPO for effective medium, giving a single-site self-consistency equation of

$$c_{\rm Cu}\tau^{\rm imp}_{\rm Cu}(E;t_C,t_{\rm Cu})^{00}_{LL'} + c_{\rm Au}\tau^{\rm imp}_{\rm Au}(E;t_C,t_{\rm Au})^{00}_{LL'} = \tau_C(E;t_C)^{00}_{LL'}\,, \tag{2.6}$$

where 00 explicitly indicates that electron scattering begins and ends on the impurity site. Note that the RHS depends only on the "unknown" $\mathbf{t}_C(E)$, and the LHS depends both on known impurity scatterers and the unknown $t_C(E)$. So, the equality in Eq. (2.6) must be established iteratively. The SPO for the impurity can be written explicitly in terms of the effective medium SPO, i.e.

$$\tau^{\rm imp}_{\alpha}(E)^{00}_{LL'} = \mathbf{D}_\alpha\tau_C(E)^{00}_{LL'} \text{ with } \mathbf{D}_\alpha = [1+\tau_C(E)^{00}(\mathbf{t}_\alpha(E)^{-1}-\mathbf{t}_C(E)^{-1})]^{-1}\,,$$

where α is either Cu or Au. Using the inverse Fourier transform for the 00 element

$$\tau^{00}_C(E) = \frac{1}{N}\Sigma_{\mathbf{k}}\tau^{00}_C(\mathbf{k},E) = \frac{1}{N}\Sigma_{\mathbf{k}}(\mathbf{t}_C(E)^{-1}-\mathbf{g}(\mathbf{k},E))^{-1} \tag{2.7}$$

for N samples in $\mathbf{k}$-space. For a perfect lattice of CPA (complex) scatters, Eq. (2.7) can be solved like a band-structure problem, with initial guess $\mathbf{t}_C(E) := \mathbf{t}_{\rm ATA}(E)$, and then Eq. (2.6) can be concurrently solved using a Newton-Raphson root-finding method. The CPA equation has to be solved independently for each energy E. Moreover each Newton-Raphson iteration requires a separate integration over the BZ to obtain a new guess $\tau^{00}_C(E)$. The end result is that software is many times slower when using the CPA. The real potentials $V_{\rm Cu}(\mathbf{r})$ and $V_{\rm Au}(\mathbf{r})$ can be obtained once $\tau_C(E)$ is known by using the real-space fundamental equation of MST at the respective impurity site. That closes the loop for a self-consistent determination of $V(\mathbf{r})$.

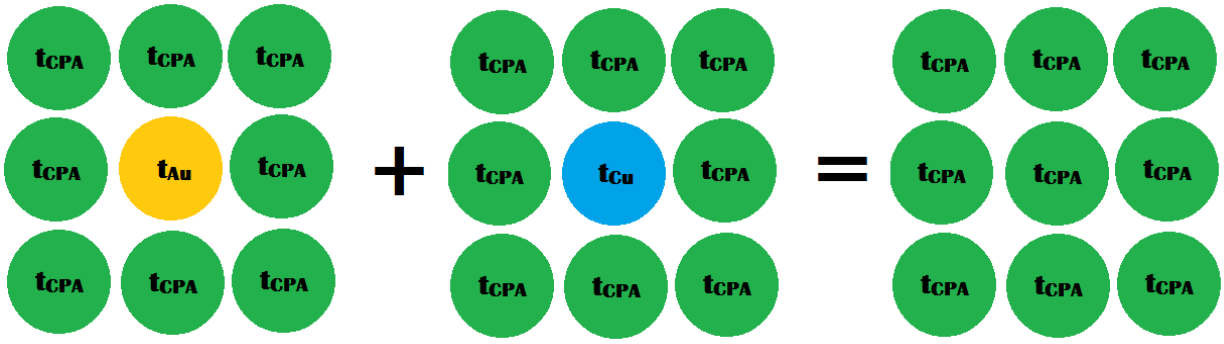

Figure 2.1: The CPA requires that the average scattering from the solutes embedded in the medium create a coherent lattice.

2.2.5 Thermodynamics and Total Energies

In a single-particle description of a many-body system, the number of particles

$$\mathcal{N}(\mu) = \int_{-\infty}^{\infty} d\epsilon\, \bar{n}(\epsilon) f(\epsilon - \mu), \tag{2.8}$$

where $f(\epsilon - \mu)$ is the Fermi-Dirac function and $\bar{n}(\epsilon)$ is the ensemble-averaged density of states for the electronic chemical potential μ. Notably, from a thermodynamic (Gibbs') identity,

$$\mathcal{N}(\mu) = -\frac{\partial \Omega}{\partial \mu}_{V,T}, \tag{2.9}$$

and, if we have a closed-form solution for $\mathcal{N}(\mu)$ in a system, we obtain a variational closed-form expression for the electronic Grand Potential $\Omega(\mu, T, V)$. Indeed, it is easily shown the electronic Grand Potential is

$$\Omega(\mu, T, V) = -\int_{-\infty}^{\infty} d\epsilon\, \bar{N}(\epsilon; \mu) f(\mu - \epsilon) + \int_{-\infty}^{\mu} d\mu' \int_{-\infty}^{\infty} d\epsilon\, \frac{\partial \bar{N}(\epsilon; \mu')}{\partial \mu'} f(\mu' - \epsilon) \tag{2.10}$$

where $\bar{N}(\epsilon; \mu)$ is the ensemble-averaged, integrated density of states (i.e., integration up to fixed μ without the Fermi factor). One must add the average nuclear-nuclear interaction energy for all atoms for a total $\Omega(\mu, T, V)$. At 0 K, $f(\epsilon - \mu) \to \Theta(\epsilon - \mu)$, and $\Omega(\mu, T, V) \to E(\mu) - \mu \bar{N}(\mu)$, which is the electronic total energy. The above results leads to a very simple, and general derivation of the finite-temperature Kohn-Sham-Mermin theorem. Importantly, again, if we have an analytic expression for $\bar{N}(\epsilon; \mu)$, we can derive an analytic expression for $\Omega(\mu, T, V)$.

In general, an expression for $\bar{N}(\mu)$ is given by the so-called Lloyd's formula, which is specified in the next chapter for KKR (ordered) in Eq. (3.10) and the KKR-CPA (disordered) in Eq. (3.11). Notably, Lloyd's

formula is an *analytic, closed-form* solution for the integrated $\bar{n}(\epsilon)$ within the KKR(CPA) formalism. In the CPA, by substitution of the Lloyd expression, it may be derived (c.f. [6])

$$E(\mu) - \mu\bar{N} = \int_{-\infty}^{\mu} d\epsilon\,(\epsilon - \mu) \sum_{\alpha} c_{\alpha}\bar{n}_{\alpha}(\epsilon) - \int_{\Omega} d^3r \int_{-\infty}^{\mu} d\mu' \sum_{\alpha} c_{\alpha}\bar{\rho_{\alpha}}(\mathbf{r})\frac{\partial v_{\alpha}(\mathbf{r})}{\partial \mu'}, \tag{2.11}$$

where $\bar{n}_{\alpha}$ is the density of states, $\bar{\rho}_{\alpha}(\mathbf{r})$ the charge density, and $\bar{v}_{\alpha}(\mathbf{r})$ the potential for the α component on a site. An important point about Eq. (2.11) is there is a variational principle underlying it: $\delta(\bar{E}-\mu N)/\delta\bar{\rho}_{\alpha} = 0$. As a result of Eq. (2.11), we have a closed-form solution for the total energy (or grand potential at finite temperature) for disordered, partially ordered, or fully ordered systems within the CPA, just as found in band-structure methods. For further reading consult [6, 115].

This short section provides the mathematical basis for a proper self-consistent-field density functional theory (DFT) within a first-principles CPA, which recovers at finite temperature Mermin's theorem immediately for ordered (as found in typically band-structure case) and for partially ordered or disordered cases in the KKR-CPA. A similar derivation and grand potential is obtained for the DCA [115], which then includes atomic short-range order within the electronic structure. Such a derivation is possible from a KKR representation based on *Lloyd's formula* [116, 117], which is an expression for the configurationally–averaged *integrated* density of states $\bar{N}(E)$ as a function of energy E, known for ordered solids [118, 119, 116] and CPA [120, 121]. Lloyd's formula is a Friedel-like sum rule for the change in the number of states around an impurity cluster in a solid, see section 3.2.

As a result, we have a scf-DFT KKR-CPA to address disordered, partially ordered, or fully ordered alloy systems on an equal footing. We will utilize this to calculate the formation enthalpies as needed to explain stability in doped Fe-based superconductors.

Chapter 3

Computational Tools

3.1 Bloch Spectral Function: Disordered Electronic Structure

The Bloch spectral function $A(\mathbf{k}, E)$ is an important observable for disordered systems. It is also the observable that is directly measured in ARPES experiments. Because of its central role, I have implemented routines to evaluate it for general disordered alloys, like Cu_3Au, Cu_3Pd, and $Ba(Fe,Cu)_2As_2$. The first two systems exhibit short-range ordering spots in their diffraction patterns that can be understood by nesting of the $A(\mathbf{k}, E)$ near the Fermi level. The latter system exhibits an instability to an incommensurate SDW, also due to nesting. This analysis can be carried over to other Fe-SCs and may suggest splitting in compounds that have not been explored yet.

The Bloch spectral function is expressed in the Fourier representation as

$$A(\mathbf{k}, E) = -\frac{1}{\pi}\mathrm{Im}\sum_{\mathbf{k}} G(E, \mathbf{k}+\mathbf{K}, \mathbf{k}+\mathbf{K})\,. \tag{3.1}$$

It is the **k**-space resolved DOS folded back into the BZ. For an ordered crystal this corresponds to Dirac delta function peaks at Bloch wave solutions.

For a given Bravais lattice with chemical disorder due to homogeneous distribution of dopant atoms represented within the CPA, the spectral peaks defining the band structure (electronic dispersion) are broadened to reflect they are no longer stationary. The mean-field, effective Hamiltonian is not Hermitian, and thus formerly eigenstates take on complex eigenvalues. If the disorder is not too pronounced, the effect on a Greens function can be expressed as a Lorentzian broadening. Starting with Eq. (3.1),

$$A(\mathbf{k}, E) = -\frac{1}{\pi}\mathrm{Im}\sum_{n\mathbf{k}'}\int d^3\mathbf{r}d^3\mathbf{r}'\sum_{\mathbf{K}}(e^{-i(\mathbf{k}+\mathbf{K})\cdot\mathbf{r}})\left(\frac{\psi_{n\mathbf{k}'}(\mathbf{r})\psi^*_{n\mathbf{k}'}(\mathbf{r}')}{z_{n\mathbf{k}'}-E}\right)(e^{i(\mathbf{k}+\mathbf{K})\cdot\mathbf{r}'}) \tag{3.2}$$

$$= -\frac{1}{\pi}\mathrm{Im}\sum_{n}\frac{1}{z_{n\mathbf{k}}-E} = -\frac{1}{\pi}\mathrm{Im}\sum_{n}\frac{1}{E_{n\mathbf{k}}+\Delta_{n\mathbf{k}}+i\Gamma_{n\mathbf{k}}-E} \tag{3.3}$$

$$= \sum_{n}\frac{1}{\pi}\frac{\Gamma_{n\mathbf{k}}}{(E-E_{n\mathbf{k}}-\Delta_{n\mathbf{k}})^2+\Gamma^2_{n\mathbf{k}}} \tag{3.4}$$

where $E_{n\mathbf{k}}$ is the band structure of the unperturbed, ordered crystal and $\Delta_{n\mathbf{k}}, \Gamma_{n\mathbf{k}}$ represent a shift and broadening respectively. Due to the the complex eigenvalue, states evolve in time as

$$\Psi_{n\mathbf{k}}(\mathbf{r}, t) = e^{-\Gamma_{n\mathbf{k}}(t/\hbar)} e^{i(E_{n\mathbf{k}}+\Delta_{n\mathbf{k}})(t/\hbar)} \psi_{n\mathbf{k}}(\mathbf{r}). \tag{3.5}$$

Thus, the lifetime of the states is $\hbar/\Gamma_{n\mathbf{k}}$. For no disorder, the width is 0, and hence, the lifetime is infinite (i.e., it is a stationary state); whereas, for a width 5% of the Brillouin zone dimension along a particular k-vector, the lifetime until scattering into nearby state is 10^{-15} secs.[1] Such broadening and shifting is seen is for de Haas van Alphen experiments or in broadened widths in photoemission experiments.

Within MST-CPA formalism one can write

$$A(\mathbf{k}, E) = \frac{1}{\pi} \text{Im Tr}[\mathbf{F}^{CC}(E)\tau_C(\mathbf{k}, E) + (\mathbf{F}^{C}(E) - \mathbf{F}^{CC}(E))\tau_C^{00}(E)] \text{ with} \tag{3.6}$$

$$[\mathbf{F}^{C}]^{nm}_{LL'} = \delta_{nm} \sum_{\alpha} c_\alpha \int d\mathbf{r}\, \Omega^n(\mathbf{r}) Z_L^{n\alpha}(E, \mathbf{r}) \sum_{L''} Z_{L''}^{n\alpha}(E, \mathbf{r}) D^{n\alpha}_{L''L'} \text{ and} \tag{3.7}$$

$$[\mathbf{F}^{CC}]^{nm}_{LL'} = \delta_{nm} \sum_{\alpha\beta} c_\alpha c_\beta \int d\mathbf{r}\, \Omega^n(\mathbf{r}) \sum_{L''L'''} D^{n\alpha}_{L''L} Z_{L''}^{n\alpha}(E, \mathbf{r}) Z_{L'''}^{n\beta}(E, \mathbf{r}) D^{n\beta}_{L'''L'} \tag{3.8}$$

for the indices α, β running over all mixing atoms on the nth site in the unit cell, $D^{n\alpha}_{LL'}$ gives the SPO for the corresponding impurity crystal (as introduced in the section on the CPA), and 00 indicates the central unit cell in the crystal. The first term is just a composition weighted DOS of the fundamental equations of MST for the impurity crystals. The second term is a correction for scatterings that start and end on different species of impurity atom; its presence is essential to prevent nonphysical, negative densities.

I implemented the Bloch spectral function into our KKR-CPA package. This required code that could compute the mixed-component real-space integrals for F^{CC}. *The Bloch spectral function is critical to visualizing band structures and Fermi surfaces,* a key component of my analysis. In order to output the band-structure, a set of waypoints in k-space and an energy window is specified. This then generates a spaghetti plot for the band structure similar to Fig. 4.8. For visualizing the Fermi surface, the waypoints in k-space, along with the Γ point define a closed area. This area is traversed either by rays emanating out from Γ or by parallel line segments. This results in plots similar to Fig. 4.6.

[1] To make this lifetime estimate, we note the following simple argument: For quasiparticles near certain high symmetry points in the Brillouin zone, $E = \hbar^2 k^2/2m^*$, where m* is the effective mass. To order of magnitude, we can replace m^* with the electron mass, m. Then, the lifetime $\Gamma \sim \hbar/dE = \hbar m/(\hbar^2 k dk) = m/(\hbar k dk)$. We can also take the lattice constant $a = 5\text{Å}$. Then, for 5% smearing, the lifetime is about 10^{-15} sec.

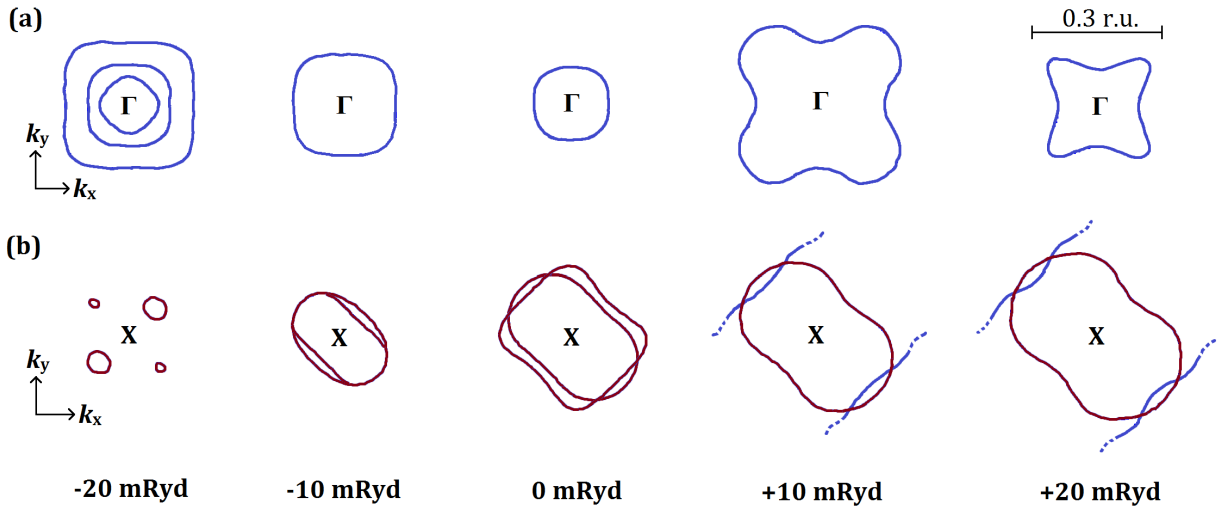

Figure 3.1: (a) Cross-sections of the band structure of $BaFe_2As_2$ for $k_z = 0$ near the Γ point for energies near to the Fermi level (as determined by contour integration, not the Lloyds Formula). Electron and hole pockets are denoted in red and blue respectively. The band structure changes rapidly with energy. (b) About the X point. The Lloyds formula predicts a dramatic shift of Fermi level to -9 mRyd. This results in better agreement with experiment.

3.2 Lloyd's Formula: Accurate Fermi level

In MST, because of the finite, numerical basis, there can be sensitivity to some quantities, with the most important being the Fermi energy. Many physical properties (e.g., Fermi surface, charge transport, etc.) depend critically on the relative location of the Fermi level. The numerical integration of the finite-basis $G_L(E)$ to get the integrated $N_L(E)$ is not the same as integration of an exact G and then truncating in L for an evaluation of $N_L(E)$. The Lloyd's formula is an analytic expression for the $N_L(E)$, providing the thermodynamically correct Fermi level.

One of my required extensions of our KKR code has been to make a feasible and general numerical implementation of this formula into software. With it we are able to evaluate correctly to the thermodynamic (rather than truncated basis) Fermi level of $BaFe_2As_2$ so that resulting Fermi surfaces properly describe the electron and holes pockets well (see Fig. 3.1).

The Lloyd's formula is an extension of the Friedel (single-site) sum-rule for the integrated DOS:

$$N(E) = N_{\text{free}}(E) + \frac{2}{\pi}\sum_{\ell}(2\ell+1)\delta_\ell(E)\,, \tag{3.9}$$

where $\{\delta_\ell(E)\}$ are the phase-shifts for scattering from the central potential $V(\mathbf{r})$ and $N_{\text{free}}(E)$ is the integrated DOS of free electrons. For complex E, Eq. (3.9) is incorrect, but it can be generalized by use of

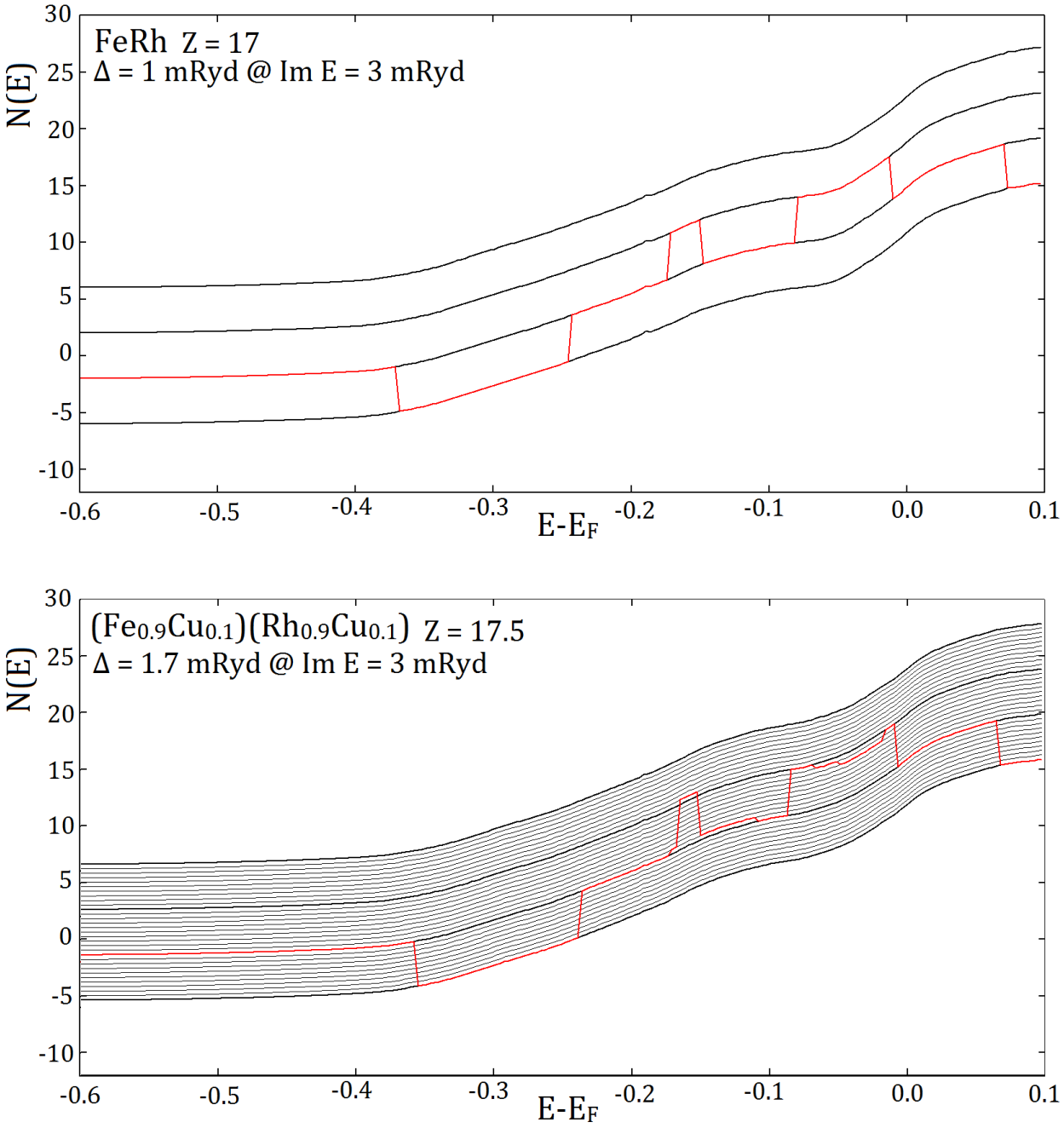

Figure 3.2: Equivalent branches of Lloyd's formula for $(Fe_{1-x}Cu_x)(Rh_{1-x}Cu_x)$ at concentrations of (a) 0.0 and (b) 0.10 showing a proliferation of branches at incommensurate concentrations. This poses a major obstacle to the use of Lloyd's formula at arbitrary concentrations.

scattering matrices. In MST the Lloyd's formula for an ordered system, where standard band-structure methods and fixed-E KKR get the same results, becomes

$$N(E) = N_{\rm free}(E) + \frac{1}{\pi}{\rm Im}\ \log||\alpha(E)|| - \frac{1}{N_k}\Sigma_{\mathbf{k}}\frac{1}{\pi}{\rm Im}\ \log||1 - \mathbf{t}(E)\mathbf{g}(\mathbf{k},E)|| \tag{3.10}$$

for N_k samples in $\mathbf{k}$-space, and where $\alpha(E)$ is defined by the behavior of the scattering solutions of $V(r)$ near the scattering centers. The Lloyd's formula, Eq. (3.10), is an amazing result being the closed-form expression for the integrated density of states! One does not have to integrate over energies numerically the Green's function to get the number of electrons – one has a direct thermodynamic expression.

The determinant is performed over both site and angular-momentum indices. The "Im log" operation yields the phase of the determinant. Because the KKR determinant passes through zero at every Bloch solution, it picks up a phase of π at these locations, which is how the formula (valid for *complex* E) tracks the number of electrons up to energy E. There is a practical limitation in that *at a given* E the above phase is only known to within modulo 2π. Thus, it can only give the total integrated DOS to within a whole number. If we already have an approximate guess for the Fermi energy, which we do, the Lloyd's formula gives an exact thermodynamic correction to that obtained from a self-consistent DFT with L-truncated Green's function.

Within the CPA approximation for disordered systems the Lloyd's formula generalizes to

$$N(E) = N_{\rm free} + \frac{1}{\pi}{\rm Im}\ \sum_{\alpha} c_\alpha \log||a_\alpha|| - \frac{1}{N_k}\sum_{\mathbf{k}}\frac{1}{\pi}{\rm Im}\ \log||1 - \mathbf{t}_C\mathbf{g}(\mathbf{k})|| - \frac{1}{\pi}{\rm Im}\ \sum_{\alpha} c_\alpha \log||1 - (\mathbf{t}_\alpha - \mathbf{t})\mathbf{G}^{00}||\,, \tag{3.11}$$

where the index α runs over all mixing atoms, $\mathbf{t}_\alpha$ is the scattering off the impurity potential $V_\alpha(\mathbf{r})$,$G^{00} = \frac{1}{N_k}\sum_{\mathbf{k}} G^{00}_{LL'}(\mathbf{k},E)$, and E has been suppressed for clarity. Approximations beyond the CPA, such as the DCA (dynamical cluster approximation), have a similar analytic formula.

There is a concentration weighting of terms in the Lloyd's formula for the CPA. This leads to a serious complication as there is a proliferation of equivalent branches for which the Lloyd's formula can be output (c.f. Fig. 3.2). In these calculations, the only way around this was to compute the Fermi level for adjacent, commensurate concentrations and then to use this information to surmise which is the correct branch. Once the correct branch is known, the formula gives a precise location of the Fermi level.

3.3 Brillouin Zone: Construction and Symmetry

In order to perform integration of the Brillouin zone (BZ), it was necessary to create a geometric representation of it. This was done in the same way a Wigner-Seitz cell is constructed. Large rectangular planar faces were setup normal to, and at the midpoint of, the line segment connecting Γ to neighboring reciprocal points. This was done for the first three shells of neighboring reciprocal points, all but ensuring that no faces of the Brillouin zone would be missing. The interior half-planes of each of these faces define the Brillouin zone interior. To complete the construction, each rectangular face is clipped against the interior of the other planes. One of the difficulties of the clipping procedure is to retain full precision without generating extraneous faces. This was done by accomplished by defining a threshold parameter to prevent the creation of faces with zero area. The final result is a set of complex, polygonal faces which define the BZ faces. The explicit description of the BZ in terms of vertices, normals, and faces simplifies geometric operations in $\mathbf{k}$-space. See Fig. 3.3 for different perspectives on the BZ of $BaFe_2As_2$.

The symmetry of the BZ then needs to be detected. In order to do this, the faces are triangulated about their center. This ensures the maximum number of symmetries are detected. (Otherwise, some rotations about the center of that face might be missed.) Vectors are then defined extending from Γ to the center of the triangulated faces, these represent the wedges of the BZ they pass through. By applying the crystal symmetry operations to these vectors, it must be that they map back on top of each other. Vectors, and their respective wedges, that map onto each other are equivalent. That means integrating a scalar quantity (e.g., spectral function) will be the same in both wedges. This, in turn, means only one wedge needs to be integrated and a degeneracy factor applied. This saves up to 48 times the effort. For a tensor quantity (e.g., the SPO), the appropriate transformation operators associated with that symmetry need to be applied to relate one wedge integral to another. For example, if wedges "a" and "b" are equivalent, then $\tau_a = D(\sigma)^\dagger \tau_b D(\sigma)$, where $D(\sigma)$ is the quantum mechanical matrix that transforms one basis $\{\alpha_n\}$ to $\{\sigma\alpha_n\}$ for crystal symmetry σ.

3.4 Brillouin Zone: Integration via "Ray" Method

The above observable require a BZ integral for $\tau(\mathbf{k}, E)$ to be performed multiple times. This is nontrivial as $\tau(\mathbf{k}, E)$ blows up whenever $(\mathbf{k}, E)$ corresponds to a Bloch wave solution. To actually perform such integration I have written an integration routine that is based on wedges which emanate from the Γ point to the faces of the BZ. This method is applicable to complex crystals, is adaptive to angular variations in $\tau(\mathbf{k}, E)$, and returns error bounds.

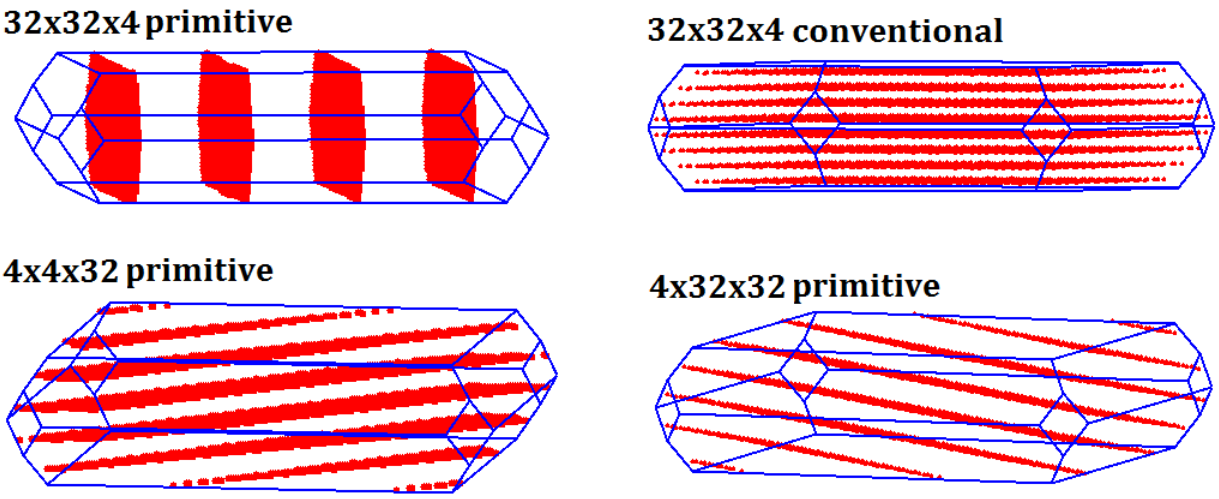

Figure 3.3: The Brillouin zone of $BaFe_2As_2$ from four perspectives. Also shown is different sets of points for sampling the k-space, some better representing the space than others.

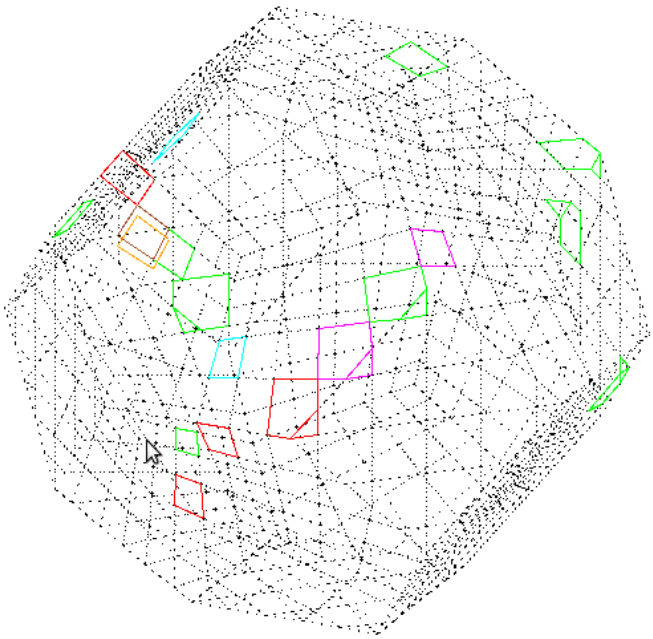

Figure 3.4: Tetrahedron defined by the zone center and a gridded circumscribing box that are clipped to the face-centered cubic Brillouin zone boundary.

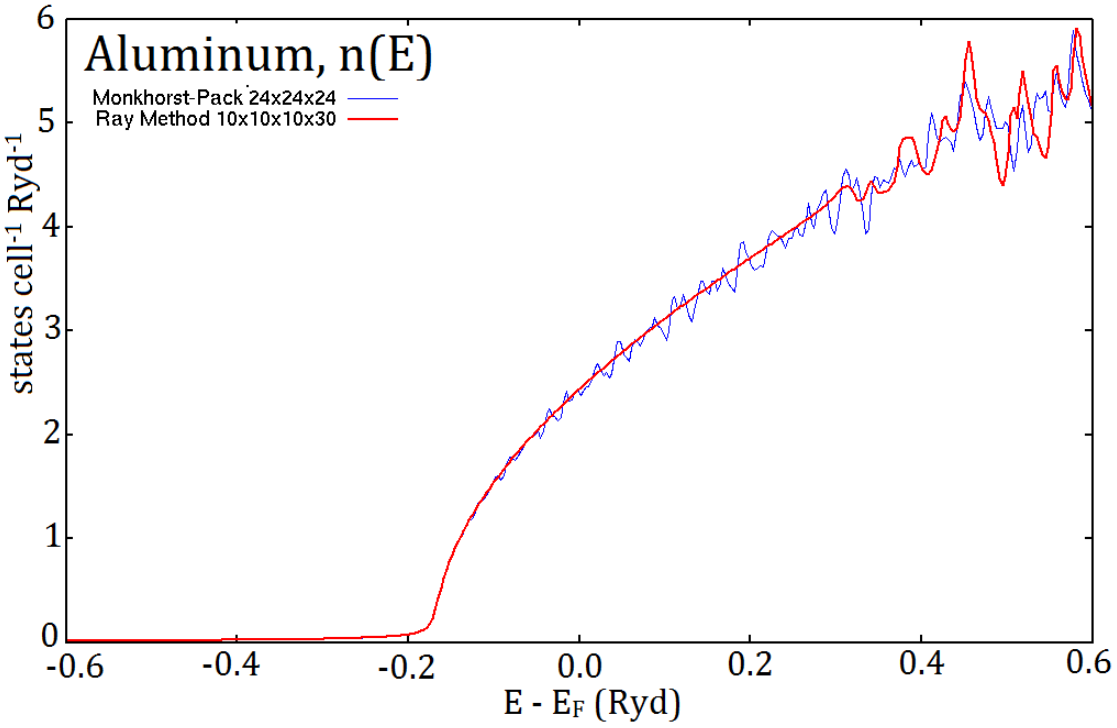

Figure 3.5: The ray method does a better job of capturing the $\sqrt{E}$ singularity in the density of states at the on-set of a band than the ubiquitous Monkhorst-Pack special k-points scheme.

The BZ is split into pyramidal wedges whose base is the BZ faces and whose vertex is the Γ point. This set is further split by triangulating the base planes about their center to define refined bases and new wedges. Every symmetry operation is acted on these wedges to determine which sets of wedges W_n are equivalent to each other. Multiplying the one-dimensional integration along Γ to the center of the base of W_n by the volume of W_n provides an integration estimate. The advantage of using 1-D integrals is that the integrand $\tau(k\hat{\mathbf{k}}_{\text{ray}}, E)k^2$ can be fit to a cubic rational function, i.e.,

$$\frac{p_3k^3 + p_2k^2 + p_1k + p_0}{q_3k^3 + q_2k^2 + q_1k + q_0}k^2, \tag{3.12}$$

which can be integrated exactly with respect to k within a small domain. This follows because Eq. (3.12) can be expanded in partial fraction decomposition as

$$a_2k^2 + a_1k + a_0 + \frac{c_1}{k - z_1} + \frac{c_2}{k - z_2} + \frac{c_3}{k - z_3} \tag{3.13}$$

and the latter terms integrate to logarithms. Thus, the singularities in $\tau(\mathbf{k}, E)$ are treated exactly.

To check the error in the integral, a refinement of W_n is made by subdividing it into the four wedges

formed by the triangulation of the base of W_n on connecting the midpoints of its edges. These new wedges give a more accurate estimate of the wedge integral. The difference between these two integrations of the same wedge W_n gives an estimate of the error. If the error is too high, further recursive subdivisions can be performed until the desired tolerance is reached. For many metals, where band energy contours are close to spherical, the error is low and only 24 samples are required along a ray. In other cases it is possible to improve on this method by choosing more than one center of integration, say at the three highest symmetry points in **k**-space.

Later, a further refinement was made to the ray method that took better advantage of the symmetry of system. Most crystals have either orthorhombic or hexagonal conventional cells. Thus, in an alternate scheme for generating tetrahedra W_n, a circumscribing box (with orthorhombic or hexagonal symmetry) is placed about the BZ. The faces of this box are then grided uniformly and grid cells, along with the Γ point, define tetrahedral wedges W_n. This results in improved convergence of integrals with respect to mesh resolution.

An example of the efficacy of the ray method is shown in Fig. 3.5 for face-centered-cubic aluminum. At the onset of a band edge there is a van-Hove singularity which gives rise to a $\sqrt{E}$ singularity in the density of states. The standard Monkhorst-Pack scheme has difficulty capturing such singularities because it chooses a discrete set of sampling points. On the other hand, the ray method captures such a singularity well because it models the integrand as a rational function that is then analytically integrated. The presence of van-Hove singularities near the Fermi level can have a strong effect on the electronic properties of a material. Furthermore, it is only possible to perform a Lloyd formula integration using the ray method. This is because the ray method can track phases along a ray (which undergo large jumps near the bands), whereas the Monkhorst-Pack cannot because it consists of a disconnected set of sampling points.

3.5 Coarse Parallelization over Energy and k-space

For systems as complex as AFM Ba(Fe-Co)$_2$As$_2$, it takes much longer for the charge-density and potential solutions to converge because the CPA self-consistency must be achieved before then next charge self-consistency. In order to complete a large number of calculations in short order, it is necessary to parallelize the calculation to run on high-performance clusters. I have implemented a coarse parallelization of the code by subdividing the energy contour integration and BZ k space integration over compute nodes (see Fig. 3.6). For simple systems this results in an optimal time reduction by a factor of N for N nodes. This was done using the Message Passing Interface (or MPI).

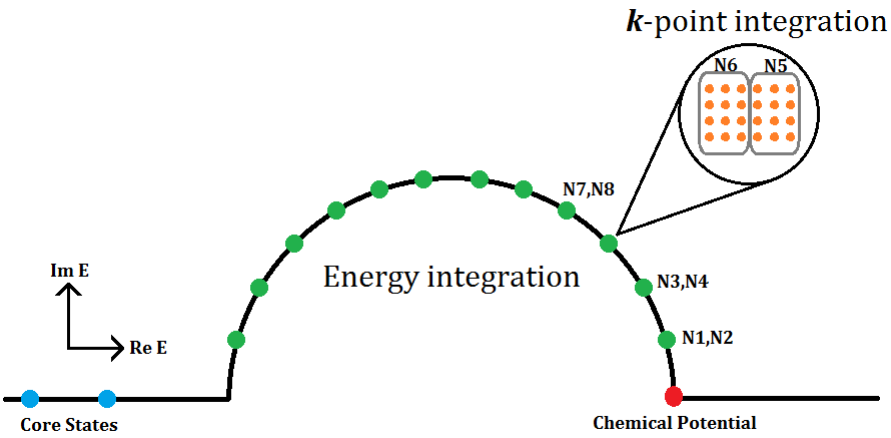

Figure 3.6: (Color online) In this example, compute nodes (N1-N8) are distributed two each for every energy sample point on the contour integral. The nodes at a given sample point subdivide the **k**-space evaluations that in a **k**-space integral..

3.6 Fine parallelization and Preconditioning for sparse $M = \tau^{-1}$

Parallelization can take place at many levels in KKR theory. The integration samples over **k**-space and energy E can all be calculated independently. For cells with a modest number of atoms there can be thousands of such sample points, and parallelization over this set is sufficient to exhaust all the cores likely to be available. For larger cells **k**-space is reduced in size and only a few k space samples are needed, redirecting a bulk of the effort to the matrix inversions for $\tau(\mathbf{k}, E)$. Therefore parallelization may be needed at this finer level. This can be achieved by solving the sparse linear system $\tau(\mathbf{k}, E)^{-1}\mathbf{x} = \mathbf{e_i}$ to get each column of $\tau(\mathbf{k}, E)$ independently. Without a preconditioner $\mathbf{P} = \mathbf{M^{-1}}$ that can also be found in parallel, the common iterative procedures that solve for $\mathbf{x}$ will converge slowly.

I have written my own implementation of a complex version of the sparse approximate inverse algorithm (SPAI) to find $\mathbf{P}$ for a sparse matrix $\mathbf{M}$. Unlike most preconditioners, this algorithm will work for any non-Hermitian matrix M and can be computed in parallel for each column. This is essential as the Greens function $G(E)$ is non-Hermitian for complex E. SPAI allows the column $\mathbf{P_i}$ to be non-zero over a restricted subset of indices $\mathcal{J}$. These might be a few entries near the diagonal (e.g. $i-2 \rightarrow i+2$ for diagonal site at i). This defines a set $\mathcal{I} = \{i | M(i, \mathcal{J}) \neq 0\}$. The best choice for the nonzero entries $\mathbf{P}_i(\mathcal{J})$ is to minimize $||M(\mathcal{I}, \mathcal{J})\mathbf{P}_i - \mathbf{e}_i(\mathcal{J})||$. A direct solution for $\mathbf{P}_i(\mathcal{J})$ can be obtained in this restricted subspace by a QR decomposition of $M(\mathcal{I}, \mathcal{J})$. An LU factorization or other method could work equally well as this stage, but a QR decomposition can be updated simply in subsequent iterations. This only solves the sub-problem over $(\mathcal{I}, \mathcal{J})$ and there remains a residual $\mathbf{r} = M(\text{all}, \mathcal{J})\mathbf{P}_i(\mathcal{J}) - \mathbf{e}_i$. The trick in SPAI is to estimate which additional entries in $\mathbf{P}_i$ will be most profitable in further reducing $\mathbf{r}$. It can be shown the reduction in $||\mathbf{r}||$ by

addition of *just* the kth entry into $\mathbf{P}_i$ is$\rho_k = \frac{\mathbf{r}^\dagger \mathbf{M e_k}}{||\mathbf{M e_k}||^2}$. By calculating ρ_k for all $k \notin \mathcal{J}$, it is evident which few entries to add to $\mathbf{P_i}$ (or equivalently the set $\mathcal{J}$). Having enlarged $\mathcal{J}, \mathcal{I}$ is redefined and $||M(\mathcal{I},\mathcal{J})\mathbf{P}_i - \mathbf{e}_i(\mathcal{J})||$ again minimized. This time the QR-decomposition for $M(\mathcal{I},\mathcal{J})$ is just an update from the last iteration. This procedure is continually repeated until the residual $\mathbf{r}$ is sufficiently small (about 0.5), or the maximum fill-in allowed on $\mathbf{P}_i$ is reached. Using SPAI can reduce the number of iterations required to converge $x = [\tau(\mathbf{k}, E)]_i$ by an order of magnitude.

3.7 Voronoi Polyhedra and Gaussian Integration

A parametric integration routine was also developed for real-space integrations of the Voronoi polyhedra (VP) defining atomic cells. These were needed for charge density integrations. As the integrand here is well-behaved, unlike that for $\tau(\mathbf{k}, E)$, an alternate integration scheme was developed. In this case one that takes advantage of the smooth integrand $\rho(\mathbf{r})$. To perform this integration the VP is subdivided into wedges, much as in the BZ construction. A bi-unit box, and its associated Gauss points, are mapped to the VP wedge to perform the integral. Details are specified below and can also be read in [122].

Dual Coordinate Transformation and Gauss Quadrature Sums

Having divided the system into VP about each atom, there are two ways to proceed depending on the nature of the integrand $f(\mathbf{r})$. For simple integrands, separate each VP integration over a numerous simple polyhedra associated with each VP face and perform Gauss quadrature sum, and the method works straightforwardly. If $f(\mathbf{r})$ has singularities near the origin, or if it is accessible only on a sparse grid, then two major VP subdomains need to be handled separately, i.e. inside and outside of the inscribed sphere. If $f(\mathbf{r})$ is spherical, the integral is one-dimensional and easy to perform accurately, whereas the second, interstitial domain is more challenging.

The interstitial has too unusual a boundary for the direct determination of suitable sampling points and their weights. To find the sampling points, we transform a bi-unit cube $-1 \leq x, y, z \leq 1$ into each pieces of the interstitial formed by each VP face and the site center but cropped by the inscribed sphere. If any face has more than four vertices, points are added within the face (uniformly distributed) so that each face can be subdivided into polygons always having at most four vertices (a quadrilateral base); as a result, no interstitial subdomain has more than eight corners, like the cube. The same map used on the Gauss-Legendre points tells us the sampling positions in each interstitial subdomain. Note that one could use a triangular base, but we find that, while both subdivisions give the same results, the quadrilateral requires less operations,

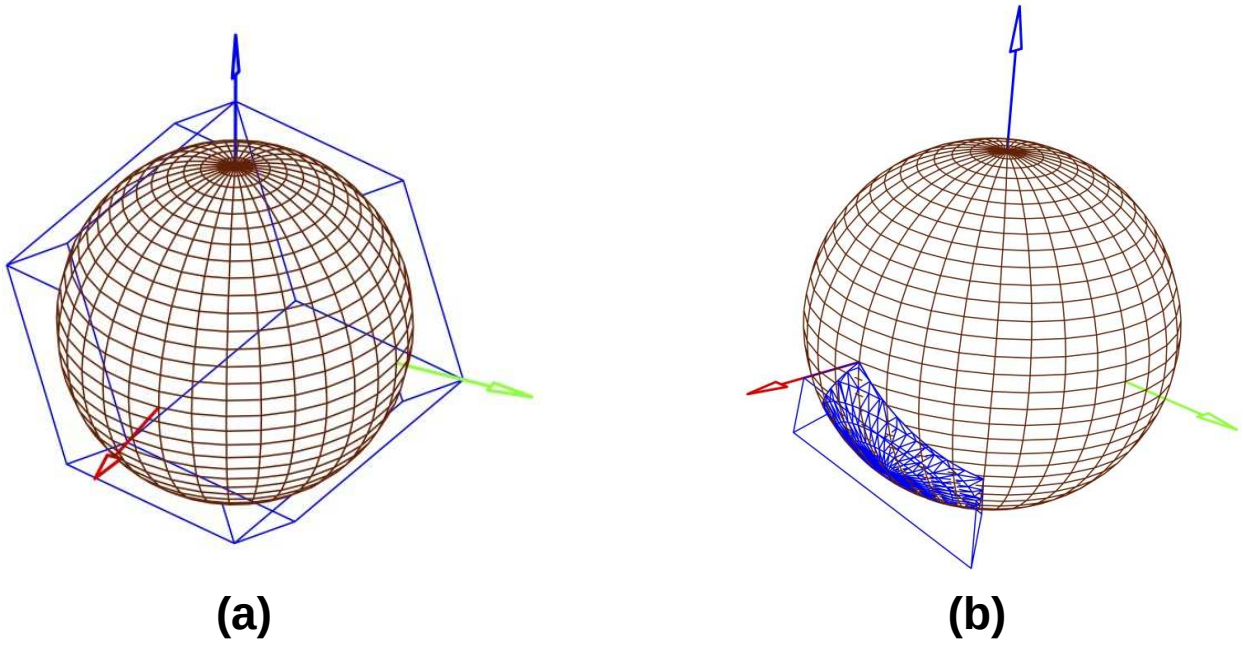

Figure 3.7: (a) VP of a FCC structure with twelve quadrilateral faces and an inscribed (touching) sphere. (b) A section of the VP shown as single truncated pyramid.

hence, it is more efficient.

For clarity, consider a one-atom FCC crystal, as in Fig. 3.7(a), where the VP consists of 12 quadrilateral faces, which are divided into 12 cropped pyramids. Pick one, as in Fig. 3.7(b), and introduce spherical coordinates (r, θ, ϕ) so that the z-axis is perpendicular to the VP face. Within each piece, the radius r runs from the inscribed radius R to the pyramid base (or VP face). To consider the case where the inscribed sphere integral is not done separately, take $R \to 0$ in what follows, and each pyramidal piece will no longer be cropped.

Before we map the cube to this element, we must find a transformation that flattens the curved interior surface. Choose any three of the four corner vertices formed by the intersection of the pyramid and the inscribed sphere. These three points are taken to define an interior plane. Now consider a cross-section of the element at fixed angle ϕ or θ, which resembles Fig. 3.8(a). Note l_n is the distance from center of the inscribed sphere to point of intersection of radius vector with interior plane; and l_f is the distance to intersection with base plane (or face). Then the map

$$r = \frac{1}{l_f - l_n}\Big[l_f(R - l_n) + r'(l_f - R)\Big] \tag{3.14}$$

will radially expand the interstitial piece (unprimed coordinates) so that the surface cut of the inscribed sphere will map to the interior plane (primed coordinates). Note that the map as given takes the plane to

the sphere, because, ultimately, we want a map from the cube to the interstitial piece. Despite the simplicity of the map (Eq. 3.14), the Jacobian J_1 is non-polynomial due to the angular dependence of $l_f(\theta,\phi)$ and $l_n(\theta,\phi)$. The standard determinant form of J_1 can be simplified by considering the volume change of an infinitesimal cell embedded in a spherical coordinate mesh. The cell will be stretched radially by a factor of $dr/dr' = (l_f - R)/(l_f - l_n)$. And, because the cell will be translated radially from r' to r, the base area will change from $r'^2 d\Omega$ to $r^2 d\Omega$. Thus, the total volume change (ratio) of the cell will be $\frac{(l_f-R)}{(l_f-ln)}\frac{r^2}{r'^2}$.

Having flattened the interior, curved surface, we then perform a second mapping from this hexahedra to a bi-unit $2\times2\times2$ cube, as depicted in Fig. 3.9. Let (x',y',z') and (x'',y'',z'') be the coordinates before and after the transformation, respectively. Mathematically, we can connect them using the expression

$$\begin{bmatrix} x' & y' & z' \end{bmatrix} = \frac{1}{8}\begin{bmatrix} 1 & x'' & y'' & z'' & x''y'' & y''z'' & x''z'' & x''y''z'' \end{bmatrix} \times \tag{3.15}$$

$$\begin{bmatrix} 1 & 1 & 1 & 1 & 1 & 1 & 1 & 1 \\ 1 & -1 & -1 & 1 & 1 & -1 & -1 & 1 \\ -1 & -1 & 1 & 1 & -1 & -1 & 1 & 1 \\ 1 & 1 & 1 & 1 & -1 & -1 & -1 & -1 \\ -1 & 1 & -1 & 1 & -1 & 1 & -1 & 1 \\ -1 & -1 & 1 & 1 & 1 & 1 & -1 & -1 \\ 1 & -1 & -1 & 1 & -1 & 1 & 1 & -1 \\ -1 & 1 & -1 & 1 & 1 & -1 & 1 & -1 \end{bmatrix} \cdot \begin{bmatrix} x'_1 & y'_1 & z'_1 \\ x'_2 & y'_2 & z'_2 \\ x'_3 & y'_3 & z'_3 \\ x'_4 & y'_4 & z'_4 \\ x'_5 & y'_5 & z'_5 \\ x'_6 & y'_6 & z'_6 \\ x'_7 & y'_7 & z'_7 \\ x'_8 & y'_8 & z'_8 \end{bmatrix}. \tag{3.16}$$

where the index in the subscript (1 to 8) indicates the vertex number in Fig. 3.9. In this map, we have reverted to describe the hexahedral element in cartesian coordinates (x',y',z') rather than the spherical (r',θ',ϕ').

The Jacobian of the transformation J_2 that turns the hexahedra into a bi-unit cube is

$$J_2 = \begin{vmatrix} \frac{\partial x'}{\partial x''} & \frac{\partial x'}{\partial y''} & \frac{\partial x'}{\partial z''} \\ \frac{\partial y'}{\partial x''} & \frac{\partial y'}{\partial y''} & \frac{\partial y'}{\partial z''} \\ \frac{\partial z'}{\partial x''} & \frac{\partial z'}{\partial y''} & \frac{\partial z'}{\partial z''} \end{vmatrix}. \tag{3.17}$$

Thus, the volume integral over the interstitial region transforms to a volume integral over a cube. This

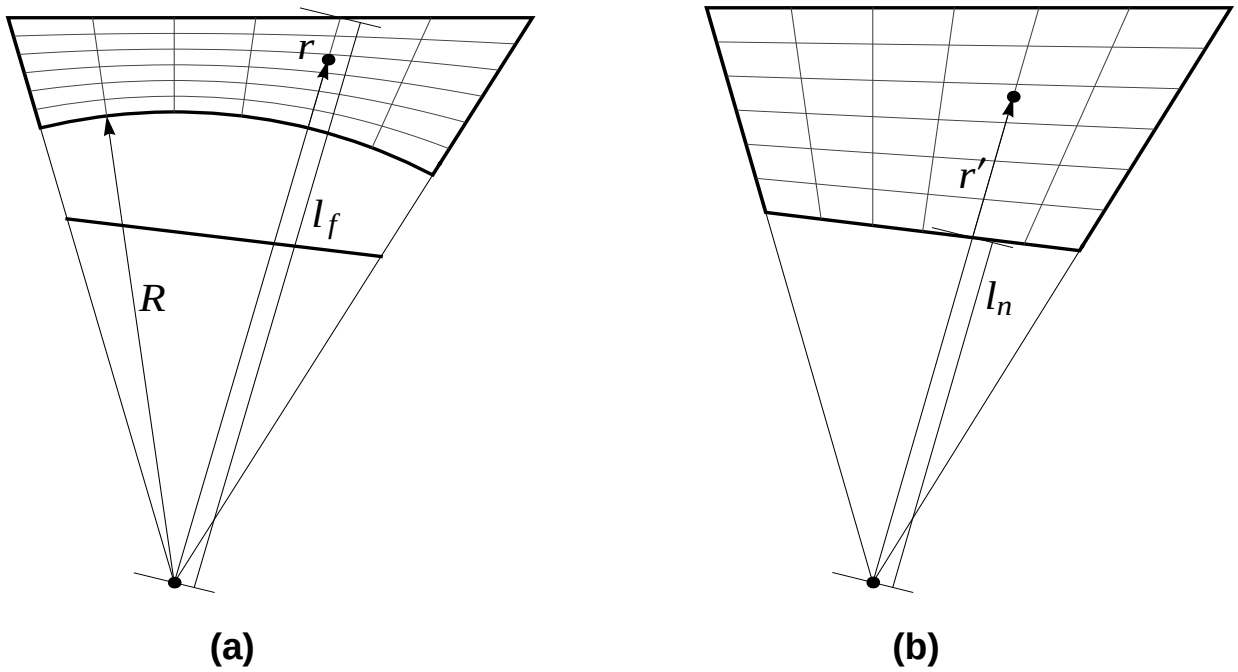

Figure 3.8: Cross-section of the cropped pyramid (a) before radial scaling and (b) after radial scaling.

can be expressed, using Gaussian-Legendre integration, as

$$\begin{aligned}\int_{\Omega^{IS}} f(\mathbf{r})d^3\mathbf{r} &= \int_{-1}^{1}\int_{-1}^{1}\int_{-1}^{1} d^3\mathbf{r}'' f(\mathbf{r}'')\ J_1\ J_2 \\ &= \sum_{l=1}^{N_l}\sum_{m=1}^{N_m}\sum_{n=1}^{N_n} f(x''_l, y''_m, z''_n)J(x''_l, y''_m, z''_n) \\ &\qquad \times w_l(x''_l)\ w_m(y''_m)\ w_n(z''_n) \end{aligned} \tag{3.18}$$

where $J = J_1 J_2$, and N_l, N_m and N_n are the number of quadrature points along x''-,y''- and z''-axes, respectively. The Gauss points x_i and weights w_i are known analytically from the zeroes of the Legendre polynomial, so Eq. (3.18) is straightforward to evaluate. Calculation time is primarily spent in numerically evaluating the analytically-derived Jacobians J_1 and J_2 for the two successive transformations and the $f(x'', y'', z'')$, hence, quite fast. This isoparametric approach achieves machine-precision error for VP integrals involving volume, charge-densities and potentials. The function $f(x'', y'', z'')$ should be evaluated at the specified x_i points; if, however, f is only defined on a discrete grid, the function must be interpolated to each x_i, in which case interpolation error is the major error that should be ameliorated to achieve high-accuracy integration. Generally, if $f(x'', y'', z'')$ is a polynomial of order p_1, p_2 and p_3 along the three directions, respectively, then the number of sampling points N required to integrate the quantity exactly for a simple polyhedra domain is $(\frac{p_1}{2}+1)\times(\frac{p_2}{2}+1)\times(\frac{p_3}{2}+1)$. For the case where we separate the integral over

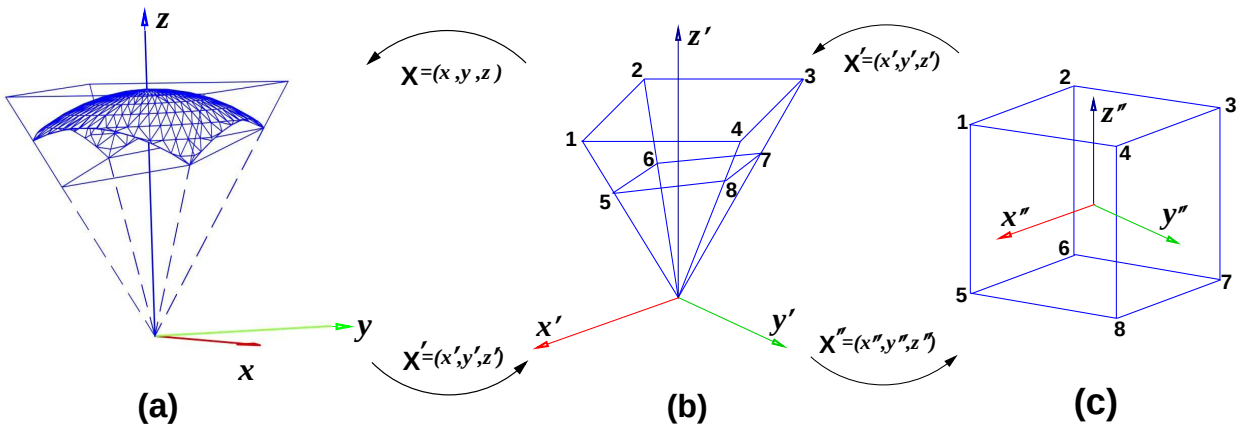

Figure 3.9: Two-step coordinate transformation: (1) Bottom curved surface (a) to the interior plane (b) via the Jacobian J_1, and (2) hexahedra in (b) to the isoparametric $(2 \times 2 \times 2)$ bi-unit cube (c) via the Jacobian J_2.

the inscribed sphere and integrate the interstitial over a domain that is curved, the transformation makes the integrand effectively non-polynomial; therefore, more Gauss points will be required.

We transform the Gauss-Legendre sampling points inside a bi-unit cube into the truncated pyramid by (1) cubic polynomial mapping of the corner points of the cube to the corner points of the truncated pyramid (given by J_2), and then (2) performing a linear mapping (in radius) of the interior plane (or side closest to origin) onto the relevant cut of the inscribed sphere (given by J_1). Our Jacobian $J \equiv J_1 J_2$ is always smooth and well-behaved, even for highly skewed pyramid. Baerends et al. [123, 124] have noted that their choice of coordinates can cause their intermediate functions to behave poorly (i.e., the J diverges) when the pyramid has wide opening angles, or a strongly skewed face. For our J to diverge, the interior plane would need to (nearly) touch the pyramid base plane; but, with the interior plane defined as the one passing through three of the intersection points of the inscribed sphere and the edges of the pyramid, this could only happen if the sphere touched one of the corners of the VP, which can never happen. In addition, the present procedure requires minimally fewer function evaluations.

An Exactly Solvable Model

To illustrate the numerical convergence and accuracy, we use Van-Morgan's exactly solvable charge-density model [125]. Many standard electronic-structure kernels can be exactly evaluated for the van Morgan density and potential, so the error in the numerical integrals can be precisely determined. We verify that accurate results are found with a modest number of Gauss points that depend on structure, and machine-precision can be achieved by increased number of points, slightly increasing computational time.

We showcase the convergence of *volume* and *charge* conservation, the $[\rho(\mathbf{r})V(\mathbf{r})]$ integral evaluated for *ki-*

netic and/or Coulomb energy, and more highly varying functions in l and $\mathbf{r}$. Apart from the cubic structures, we have also tested the convergence of the interstitial volume integral for more complex crystal structures. In the timings below, we have not utilized the associated symmetry of the crystal and the VP, so that the results reflect the most inequivalent case.

The van Morgan [125] test charge density is defined as

$$\rho(\mathbf{r}) = B \sum_{n=1}^{K} e^{i\ \mathbf{T_n}\cdot\mathbf{r}}, \tag{3.19}$$

where $\mathbf{T}_n$ are the nearest-neighbor reciprocal lattice vectors, and B is a scale factor. We will take $B = 1$ for simplicity. (From the Bauer expansion, a plane wave requires, in principle, an infinite number of spherical harmonics to be fully represented.) Because volumes Ω^{VP} and Ω^{MT} are known exactly for any crystal structure, it is often convenient, especially for site-centered methods, to divide the VP into two volumetric regions: the volume of inscribed sphere Ω^{MT} and the volume within the interstitial region Ω^{IS}, so that $\Omega^{VP} = \Omega^{IS} \cup \Omega^{MT}$.

First, we can precisely assess the numerical error associated with *volume conservation* via

$$\int_{IS} d^3r = \Omega^{IS} = \Omega^{VP} - \Omega^{MT}, \tag{3.20}$$

where $\Omega^{MT} = 4\pi R^3/3$, and, for example, R is $1/2$, $\sqrt{2}/4$, and $\sqrt{3}/4$ for SC, FCC, and BCC (in units of lattice constant), respectively. The left-hand-side numerical integral is compared with the analytic result available for the right-hand side. For example, the VP volumes are 1, 1/4, and 1/2 (in units of lattice constant cubed) for SC, FCC, and BCC, respectively.

Second, we can assess the integrations associated with *charge conservation*, including the determination of electronic chemical potential or Fermi energy. With $\rho(\mathbf{r})$ having no zero-mode component in its Fourier expansion, the integral of charge over a VP cell must be identically zero; hence, charge neutrality requires that

$$Q^{\text{total}} = \int_{VP} \rho(\mathbf{r}) d^3r = 0. \tag{3.21}$$

Subdivision of VP yields

$$Q^{IS} = \int_{\Omega^{IS}} \rho(\mathbf{r}) d^3r = -\int_{\Omega^{MT}} \rho(\mathbf{r}) d^3r. \tag{3.22}$$

Next, we can assess numerical errors for the $\rho(\mathbf{r})V(\mathbf{r})$ integral, which can be expressed as

$$[\rho V]^{IS} = \int_{\Omega^{IS}} \rho(\mathbf{r})V(\mathbf{r}) d^3r = \frac{4\pi K \Omega^{IS}}{|T_n|^2} - \int_{\Omega^{MT}} \rho(\mathbf{r})V(\mathbf{r}) d^3r. \tag{3.23}$$

Table 3.1: Convergence for the interstitial volume, charge and $[\rho V]$ integrals for various crystal structures. $\{N_l = N_m, N_n\}$ are the optimal number of points for each structure to reach an accuracy of at least 13-decimal places. VC, QC and $[\rho V]$ stands for the volume, charge and $[\rho V]$-integral convergence.

Structure	$\{N_l, N_n\}_{VC}$	$\{N_l, N_n\}_{QC}$	$\{N_l, N_n\}_{\rho V}$
SC	$\{18, 2\}$	$\{20, 6\}$	$\{18, 8\}$
BCC	$\{15, 2\}$	$\{26, 8\}$	$\{26, 10\}$
FCC	$\{13, 5\}$	$\{12, 6\}$	$\{12, 6\}$
HCP	$\{12, 5\}$		
B2	$\{15, 2\}$		
BCT	$\{12, 5\}$		

Besides band-energy (an eigenvalue summation requiring a Fermi energy) and exchange-correlation, the above three integrals reflect the main integrations contributing to DFT total energies, for example.

Accuracy

To illustrate the convergence of isoparametric integration, Figure 3.10 shows the logarithmic error in interstitial volume for six structures (i.e., 1-atom cubics, 2-atom hcp, and 2-atom B2 and BCT). Each point on the graph represents the result for a combination of quadrature points (N_l, N_m, N_n). From Fig. 3.9(a), it is clear that the cropped pyramid has a thinner dimension along the z-axis compared to the other two axes. Therefore, we use less quadrature points along $\hat{z}''$ than the $\hat{x}''$ and $\hat{y}''$, i.e., $N_n < (N_l, N_m)$; in particular, we used $N_l = N_m$. Accuracy of around 10^{-3} is already reached with only $N_l = N_m = 4$ points along the $\hat{x}''$ and $\hat{y}''$. The darker line in each panel shows the minimum number of quadrature points along $\hat{z}''$ to achieve a convergence to 13 decimal places. For example, the minimum number of Gauss points along $\hat{z}''$ for a BCC structure to attain an error less than 10^{-13} is two. The minimum number of points (N_l, N_m, N_n) required is listed below each subpanel.

The convergence of the charge density integral (Q) is given in Fig. 3.11. The left panel shows the logarithmic error in the interstitial charge Q^{IS} for the cubic structures. The right panel shows the absolute error $\epsilon^{VP} = Q^{VP}_{calc} - Q^{VP}_{exact}$ in the total charge integral. The charge convergence requires more points to yield a similar level of accuracy. For example, to achieve an accuracy of up to the third-decimal place, the BCC structure requires 8-points along the $\hat{x}''$ and $\hat{y}''$ compared to the 4-points needed for the SC and FCC structures. Higher accuracy requires more points for BCC case due to its wider and more asymmetric interstitial region.

In Table 3.1, we have listed the minimum number of points required to get the interstitial volume, charge and $[\rho V]$-integral convergence to more than 13^{th} decimal for each structure. The number of points required are given as $\{N_l = N_m, N_n\}$.

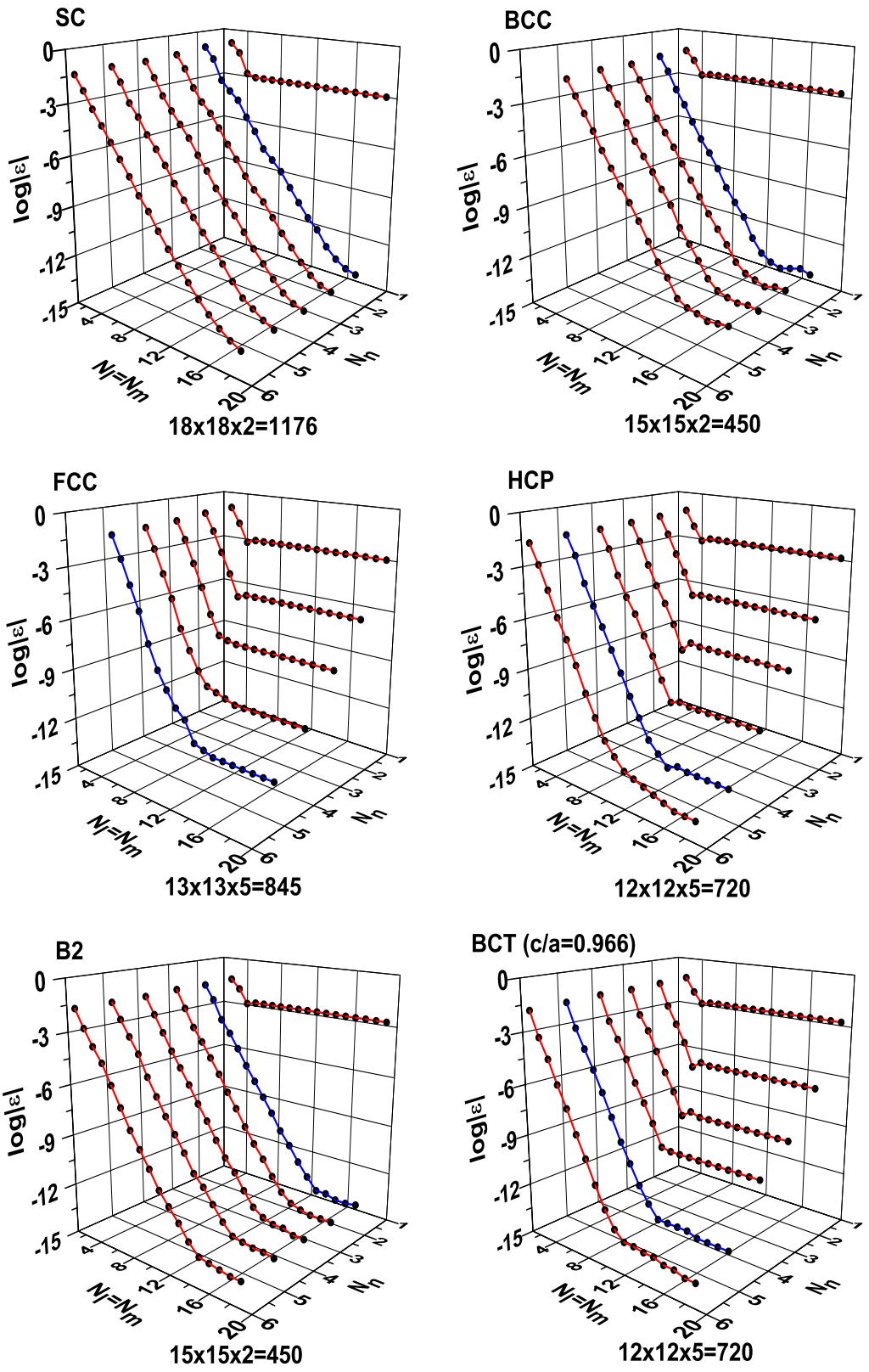

Figure 3.10: (Color online) Logarithmic (base-10) error in interstitial volumes for six structures. N_i $(i = l, m, n)$ is the number of Gauss points along $\hat{x}''$, $\hat{y}''$ and $\hat{z}''$, respectively, with $N_n < N_l = N_m$ due to a smaller caliper along $\hat{z}''$. Dark (blue) lines indicate minimum number of points along $\hat{z}''$ (total points listed below plots) to achieve 13 decimal accuracy.

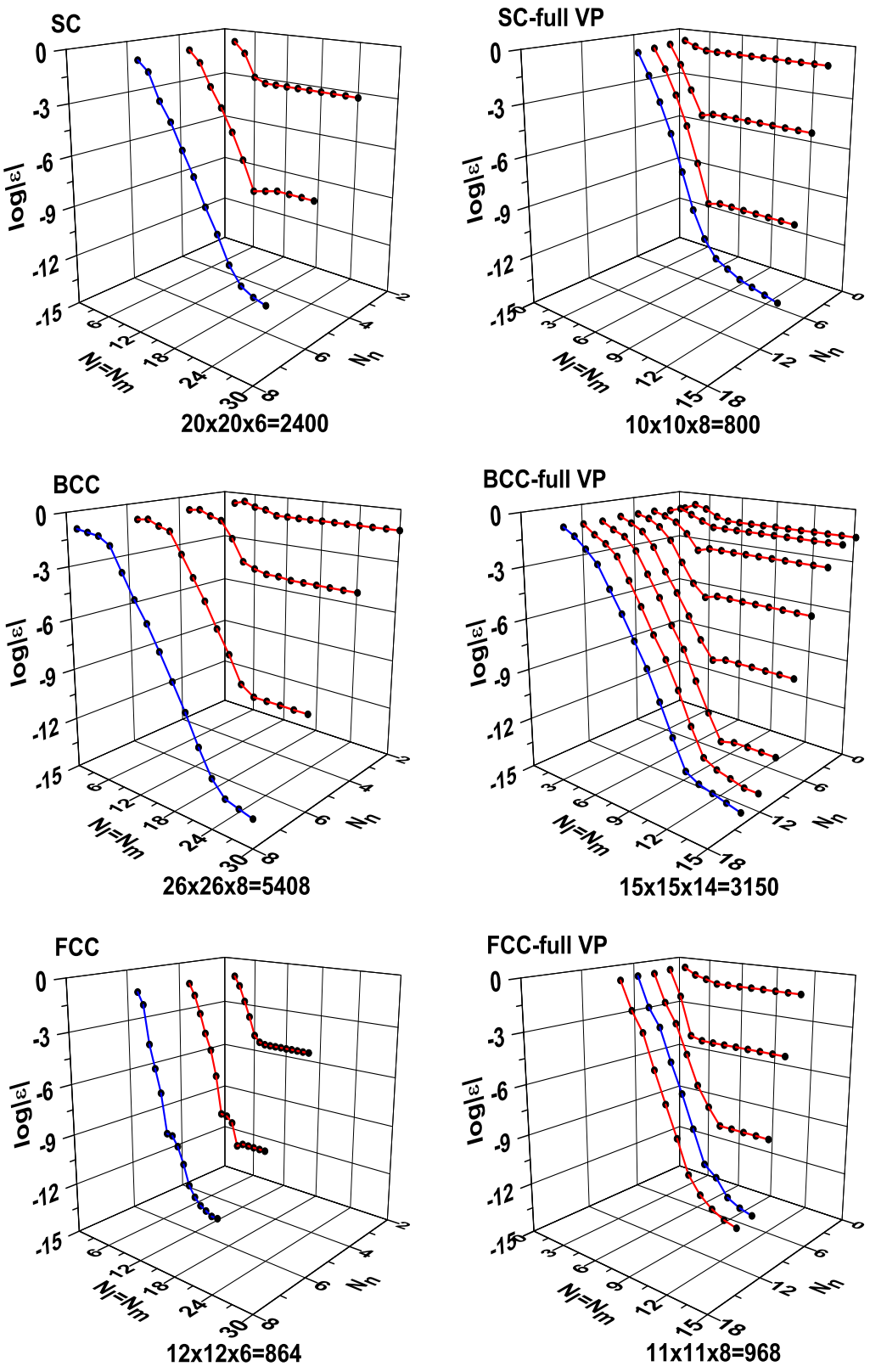

Figure 3.11: (Color online) For the van-Morgan problem for SC, BCC, and FCC, (left) the logarithmic (base-10) error in the interstitial charge, i.e., $\epsilon = (Q^{IS}_{calc} - Q^{IS}_{exact})/Q^{IS}_{exact}$, and (right) absolute error in VP total charge, i.e., $\epsilon = Q^{VP}_{calc} - Q^{VP}_{exact}$. Other details are as in Fig. 3.10.

The accuracy of all our integrals is limited by the accuracy of the VP boundary (vertices, faces and edges) information generated from the Bernal's software [126]. We have modified Bernal's original (binary-math/single-precision) code to improve its efficiency and extend its accuracy, and we were able to achieve just below 10^{-13}. We have verified that our main limitation in accuracy is due to lack of a *double-precision real* code. By rewriting the software from scratch, which is a considerable effort beyond the scope of present work, we could certainly achieve machine precision. Therefore, all integration results will be limited to just below 10^{-13}; with improved accuracy of VP information, machine-precision is achievable with similar Gauss points described.

Efficiency

To contrast the VP construction timings, we compare to the time required to expand the shape function (or 3-D step function) into spherical harmonics [127]. The shape-function approach is often used in the community when needing site-dependent quantities. The EMTO, KKR, LSMS, APW, etc., methods, for example, typically reports site-quantities, and KKR Green's function methods require site-dependent VP scattering matrices.

The shape-truncated function for a VP is defined as

$$\sigma(\mathbf{r}) = \begin{cases} 1 & \mathbf{r} \in \mathbf{\Omega} \\ 0 & \mathbf{r} \notin \mathbf{\Omega} \end{cases} \tag{3.24}$$

where Ω is the VP region. The expansion of $\sigma(\mathbf{r})$ in spherical harmonics yields the angular momentum decomposition

$$\sigma_L(|\mathbf{r}|) = \int_{\widehat{\mathbf{r}}} d\widehat{\mathbf{r}}\ Y_L^*(\widehat{r})\ \sigma(\mathbf{r}) \equiv \sigma_L(r), \tag{3.25}$$

where the integration is over the angles $\widehat{\mathbf{r}} \equiv (\theta, \phi)$ and $L \equiv (l, m)$. The shape function is used to simplify the numerical integration of any function $f(\mathbf{r})$ over the polyhedron volume Ω as

$$F = \int_\Omega f(\mathbf{r})\sigma(\mathbf{r})d^3r = \sum_{L=0}^{L_{max}} \int dr\ r^2 \sigma_L(r) \int_\Omega d\Omega\ Y_L(\widehat{r}) f(\mathbf{r}), \tag{3.26}$$

especially if it is well-represented by spherical harmonics.

The expansion coefficients $\sigma_L(r)$ must be truncated at a very high $L_{trunc} >> L_{max}$ to achieve an accurate representation of the VP shape and to obtain a reliable integral value. For example, for FCC structure, $\rho(\mathbf{r})$ is well represented using $L \leq 8$ (i.e., $L_{max} = 8$), but the shape-function should have $L_{trunc} >> 4L_{max}$ to have converged $\sigma_{L\leq 8}(r)$ that will yield an accurate integral. As we shall see, this L_{trunc} will limit the accuracy

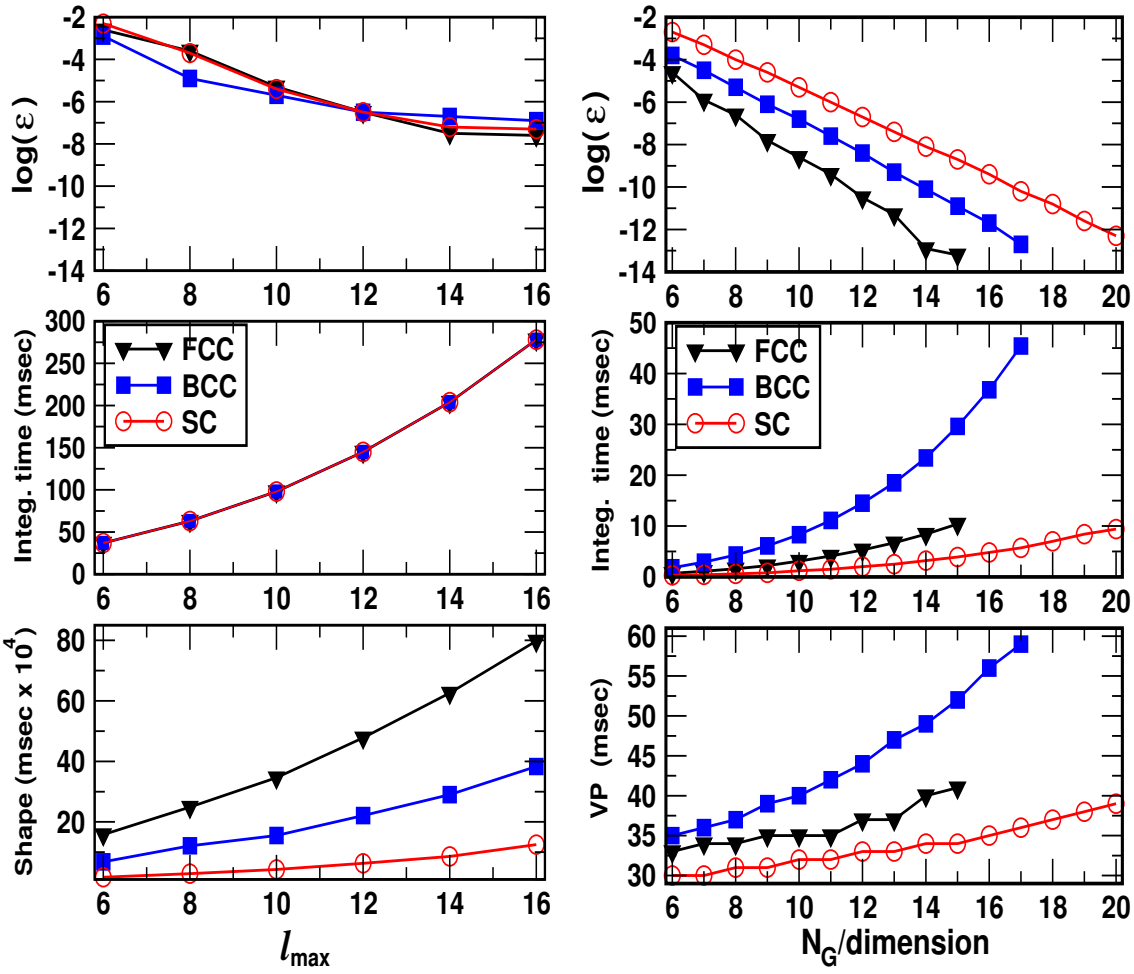

Figure 3.12: (Color online) Timings to achieve a specific level of interstitial-charge accuracy for cubic structures using shape-function (left) versus isoparametric (right) integration. Shown in panels are logarithmic error in the interstitial charge (top), and times to construct VP boundary information (bottom) and to integrate (middle). Isoparametric integration is $> 10^5$ faster and achieves machine precision.

of the integrals in the codes that use this approach, making the shape-function approach unacceptable for general (non-high-symmetry) structures, where L_{trunc} should be significantly larger than in the cubic cases to achieve the same level of accuracy as FCC.

Figure 3.12 shows accuracy and computer time for isoparametric (right panel) and shape-function (left panel) methods for SC, FCC, and BCC, for a direct comparison. The rate of convergence is given with respect to the number of Gauss points along each dimension for the present method, and with respect to the l_{max} for a fixed radial grid using shape-functions. The present method attains error in the van-Morgan interstitial charge below 10^{-13} with less computational time. The shape-function technique cannot achieve an accuracy better than 10^{-7} with $l_{max} = 16$, an extremely expensive calculation due to the high-L expansion. Hence, our method provides some significant advantages over existing approaches.

The bottom panel shows the time required to generate the boundary information necessary to achieve a certain level of accuracy. For both methods, most of the time is spent in determining the VP boundaries. The present method generates this information in terms of neighbors, vertices, faces and edges for each VP. The shape-function method gets the VP shape in terms of an L-expansion on a specific radial grid. Clearly, the shape-function method requires $> 10^4$ more time than the present method. The middle panel shows the time (in $m$sec) required to sum the final expression for the integration for both VP or shape function. The present method is faster by > 7 times. Overall, using no symmetry (degeneracy) information to reduce the computational time, we achieve $\simeq 10^5$ faster integration with 10^6 less error.

Summary

We have presented a fast, accurate, and easy to implement method for the numerical integration over general VP for polyatomic systems. The algorithm combines a weighted Voronoi partitioning of space with isoparametric integration using the Gauss-Legendre quadrature formulas of product type, and does not suffer from any ill behavior with shape of VP. In contrast to other methods, accuracy and convergence was tested rigorously via an analytic charge-density model, with machine-precision accuracy for reasonable number of Gauss points. We showed also that our algorithm is 10^5 faster and 10^7 more accurate than that based on shape-functions used in several electronic-structure codes. Our method could be used for other types of condensed matter problems requiring integration over arbitrary convex VP. Here, we implemented the general method in an site-centered, electronic-structure code and calculated formation enthalpies for FePd, yielding good agreement with experiment. The radii to set the Voronoi/Delauney tessellation weights is obtained from a physics-based definition, i.e., the saddle-points in the total electron density.

Chapter 4

Chemical and Magnetic Effects on Electronic Structure

4.1 Ba(Fe-M)$_2$As$_2$: Fermi-Surface Nesting and Magnetic Stability

Electron doping of $BaFe_2As_2$ (BFA) can be achieved by substituting a transition metal for Fe to give a metal-substituted solid solution M-BFA [128, 129], with an increasing electron-per-Fe (e/Fe) count. Notably, different behaviors for chemical and magnetic ordering instabilities are found for Co,Ni versus Cu,Zn solid-solutions, for example, with (in)commensurate AFM order depending on the dopant, with possible coexistence of SC and AFM order. Interestingly, Cr-based binary, metallic alloys [130, 131] show the same coexistence behavior but with T_c an order of magnitude smaller than Fe-SCs. Although numerous experimental studies on electron-doped BFA have been carried out over the last few years, a systematic theoretical investigation is still lacking. Here, we address $Ba(Fe_{1-x}M_x)_2As_2$ via a proper alloy theory to provide a direct comparison of trends and explain their origin.

For M-BFA in high-T I4/mmm and low-T Fmmm structures [40] with increasing e/Fe in the NM, PM, and AFM states, the KKR-CPA is used to examine relative phase stability (ΔE_f), Fermi-surface topologies and nesting (electron-hole) features through the Bloch spectral functions [132], and changes of the density of states (DOS) due to alloying and disorder, as well as to contrast these results to expectations from a rigid-band model.

4.1.1 Previous ARPES and DFT studies

Generally, DFT results on BFA match the striped AFM ordering [133] and measured electronic structure quite well. The FS exhibits two or three hole cylinders at the zone center (Γ) and two electron cylinders at the zone corner (X), as observed in DFT [31] and angle-resolved photoemission [134, 135, 136] (ARPES). The prominent (π,π) FS nesting between these cylinders helps stabilize the AFM state [12], and spin fluctuations in this mode may drive Cooper pairing [137, 138]. Hence, the need to study FS nesting and disorder

broadening effects.

The M-BFA phase diagrams show suppressed AFM ordering in favor of a neighboring SC state. The SC domes have M-fraction x=0.03-0.12, 0.02-0.08, and ∼0.04 with T_c^{max} of 23, 20, and 2 K for Co-, Ni-, and Cu-BFA, respectively [139, 129]. Zn-doped samples do not superconduct. Notably, T_c^{max} occurs near the extrapolated AFM quench concentration [139, 129]. For Co- and Ni-BFA, the magnetic order becomes an incommensurate spin-density wave before entering the SC state, which emphasizes itinerancy and import of FS nesting [140]. Cu-BFA remains commensurate [140]. And, no changes in the magnetism or FS are found in Zn-BFA [141]. In addition, there are stearic effects due to changing a and c lattice constants in I4/mmm structure. a is almost unchanged for Co-BFA and increases for Ni-, Cu-, and Zn-BFA. For Co-, Ni-, Cu-BFA c shrinks [142, 143, 144] and for Zn-BFA it increases [145].

Lastly, there is debate on whether M-BFA follows a rigid-band picture; and, if not, whether an effective Fermi level shift is still applicable. In a rigid-band model, the electronic structure is fixed to that of $BaFe_2As_2$, and the Fermi energy is raised by the amount of additional e/Fe for each dopant, as determined by their atomic number Z_i: Co (1e), Ni (2e), Cu (3e), and Zn (4e); the atomic species of the dopant becomes irrelevant (even though Z_i increases and changes the scattering properties relative to Fe), and all dopants should generate the same electronic effects for a given e/Fe. As such, a proper alloy theory can make clear assessments. While ARPES shows similar trends with nominal e/Fe for Co- and Ni-BFA, there are deviations from rigid-band for Cu- and Zn-BFA [85, 141]. By Luttinger's theorem [146], an effective e/Fe can be defined from changes in the experimentally measured FS. The phase diagrams of Co-, Ni-, and Cu-BFA have been found to approximately coincide in this manner [85]. Zn-BFA shows no measurable changes in FS and no superconductivity [141]. Comparing supercell calculations for Co- and Zn-BFA show that Co-BFA obeys rigid-band while Zn-BFA does not [147]. The rigid-band model is applicable as long as site-potential differences between Fe and dopant are much less than bandwidths. As we show, these differences are visible in a dopant's site-projected DOS, where significant overlap between Fe d-states and those of Co or Ni exists, less so for Cu, and almost none for Zn [148]. We find that the FS evolves similar to that expected from rigid-band for Co-, Ni-, and Cu-BFA but not for Zn-BFA; yet, deviations from rigid-band behavior are readily apparent in ΔE_f for PM Cu-BFA.

4.1.2 Computational Details

DFT calculations at 0 K were performed using an all-electron, KKR-CPA Green's function method [4, 5, 6]. To improve the usual site-centered basis set, empty spheres (E1, E2, and E3) were inserted at interstitial voids in the structure (Table 4.1). A local density approximation to DFT is used and the coherent potential

Table 4.1: Atomic coordinates and sphere sizes for atoms and empty spheres (E1-3). I4/mmm (Fmmm) has body-centered tetragonal (face-centered orthorhomic) unit vectors.

Site	Coordinates	Wyckoff	Radius (pm)
I4/mmm			
Ba	$(0.0000a, 0.0000a, 0.0000c)$	2a	225.1
Fe(M)	$(0.5000a, 0.0000a, 0.0000c)$	4d	136.5
As	$(0.0000a, 0.0000a, 0.3545c)$	4e	136.5
E1	$(0.5000a, 0.5000a, 0.0000c)$	2b	76.3
E2	$(0.0000a, 0.0000a, 0.2072c)$	4e	78.9
E3	$(0.2007a, 0.2007a, 0.1715c)$	16m	55.8
Fmmm			
Ba	$(0.0000a, 0.0000b, 0.0000c)$	4a	224.4
Fe(M)	$(0.2500a, 0.2500b, 0.2500c)$	8f	136.1
As	$(0.0000a, 0.0000b, 0.3545c)$	8i	136.1
E1	$(0.5000a, 0.0000b, 0.0000c)$	4b	76.1
E2	$(0.0000a, 0.0000b, 0.2072c)$	8i	78.6
E3	$(0.2007a, 0.0000b, 0.1715c)$	16n	55.7

approximation (CPA) is used to address chemical and magnetic disorder [149]. For PM states, uncorrelated, randomly-oriented local moments (site magnetizations $m_i \neq 0$) are described by a disordered local moment (DLM) state [150], where such site magnetic disorder can produce large energy broadening of the electronic states, which is reduced with magnetic short-range order included (beyond the CPA [151]), but changes FS nesting contributions to the magnetic susceptibility [152]. The DLM state is often a more appropriate representation of the PM state than the NM state ($m_i = 0$) typically assumed in theory for comparison to experiment [153, 98], such as for magnetic transition temperatures in magnetic metals [154, 149].

All results were obtained with a 8×8×8 Monkhorst-Pack k-point mesh for Brillouin zone (BZ) integrals [155], and using complex energy (E) contour integration with 25 E-points on a Gauss-Legendre semi-circular contour [156]. Fermi energies were determined from an analytic, integrated DOS (Lloyd's) formula [116] to yield an accurate electron count. The valence configurations were taken as Ba $5p^6 6s^2$, Fe $4s^2 3d^6$, Co $4s^2 3d^7$, Ni $4s^2 3d^8$, Cu $4s^2 3d^9$, Zn $4s^2 3d^{10}$, and As $4s^2 4p^3$. To match the e-per-volume of the $BaFe_2As_2$ samples probed in experiment, lattice constants (in pm) were fixed to experiment: [40] (I4/mmm) $a = b = 396.25$ and $c = 1301.68$, and (Fmmm) $a = 561.46$, $b = 557.42$, and $c = 1294.53$. As the alloy concentrations are sufficiently low, we fixed the lattice to minimize DFT (relative) error and isolate electronic and stearic effects.

Fermi surfaces were determined at E_F via the Bloch spectral function $A(\mathbf{k}, E) = -\frac{1}{\pi} \operatorname{Im} G(\mathbf{k}, E)$, where G is the single-particle Green's function. $A(\mathbf{k}, E)$ is the E- and $\mathbf{k}$-space resolved DOS and dispersion. In the limit of an ordered compound it reduces to Dirac δ-functions that define the band structure $E(\mathbf{k})$. In the presence of magnetic or chemical disorder there is $\mathbf{k}$-dependent spectral broadening and shifting due to

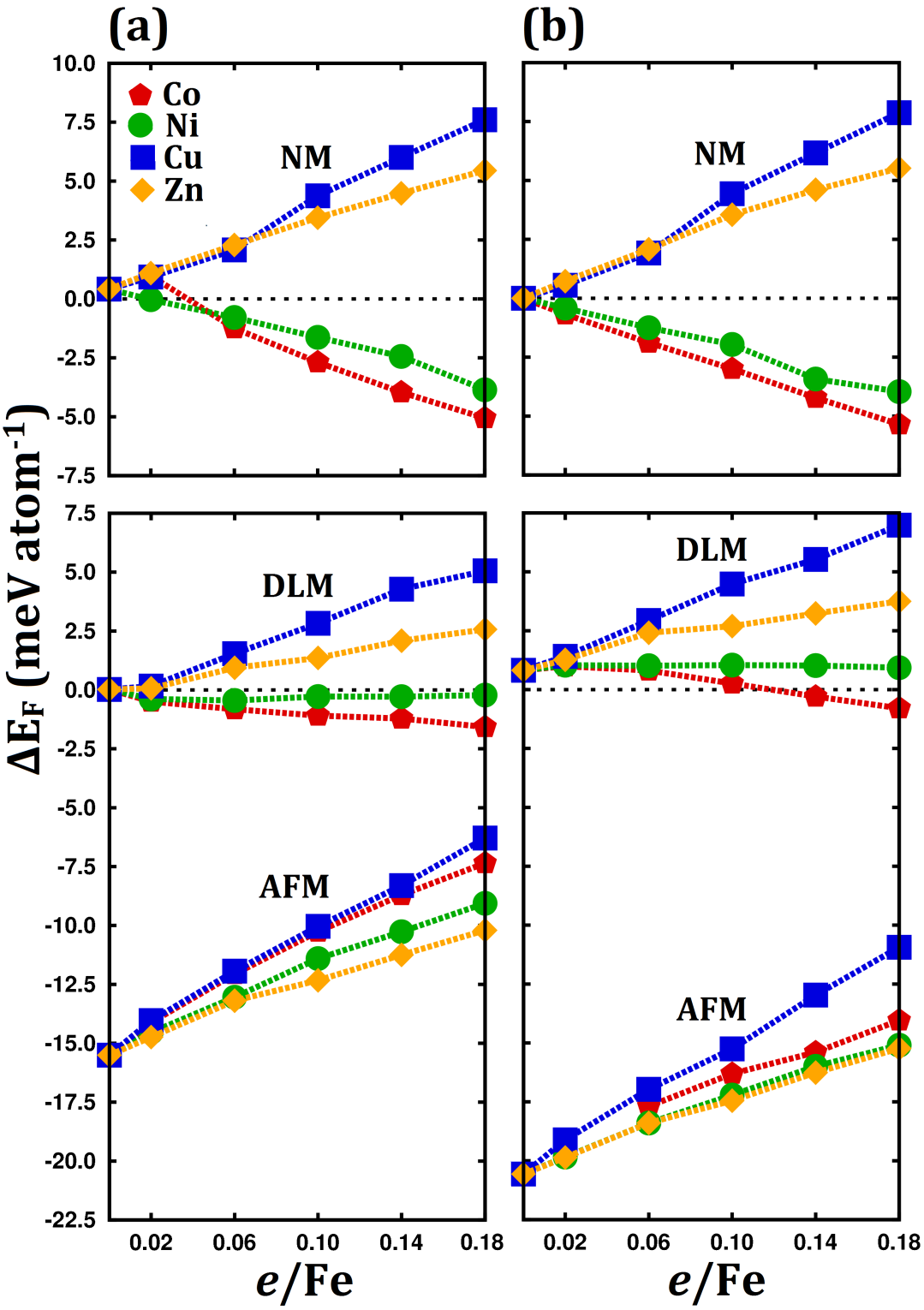

Figure 4.1: Formation energy (see Eq. (4.1) of NM, DLM, and AFM $Ba(Fe_{1-x}M_x)_2As_2$ relative to mixed phase NM endpoints $BaFe_2As_2$ and BaM_2As_2 in (a) I4/mmm and (b) Fmmm structural phases. Nominal e/Fe counting is used.

impurity scattering handled via the CPA. The spectral full-width at half-maximum with respect to energy is inversely proportional to the lifetime of electronic states [157, 158], which also dictate transport and SC properties. Spectral broadening also can support coexistence of AFM and SC, as found, for example, in binary Cr alloys, such as Cr-Ru [130].

4.1.3 Phase Stability with Alloying

For an alloy, the formation energies is defined relative to the concentration-weighted sum of the energy of the (Ba,Fe,M,As) constituents in their respective equilibrium structures. However, in a fixed host, ΔE_f trends for $Ba(Fe_{1-x}M_x)_2As_2$ versus x (or e/Fe) are more simply revealed referencing $BaFe_2As_2$ and BaM_2As_2, i.e.,

$$\Delta E_f = E^{\mathrm{Ba(Fe_{1-x}M_x)_2As_2}} - [(1-x)E^{\mathrm{BaFe_2As_2}} + xE^{\mathrm{BaM_2As_2}}]. \tag{4.1}$$

Figure 4.1 shows ΔE_f of the NM, DLM, and AFM states versus nominal e/Fe for each M, plotted relative to the mixed phase with NM $BaFe_2As_2$ and MFe_2As_2.

For no doping, the NM and DLM energies are nearly degenerate. At finite temperatures the DLM state will have a lower free-energy due to spin-disorder entropy. The AFM state is 16 (I4/mmm) or 21 meV/atom (Fmmm) below the NM state. In experiments on BFA, the magnetic and structural phase transition occur simultaneously in BFA at 140 K (or 12 meV) [139]. Previous DFT studies find 37 meV/atom (I4/mmm) using full-potential augmented plane waves (FLAPW) [31] or 70 meV/atom (Fmmm) using plane-wave pseudopotentials (PWP) [133], which is the available data.

For magnetism, we find Fe site moments (I4/mmm) are 1.4 μ_B (AFM) and 1.0 μ_B (DLM). For Fmmm, there is only a slight drop to 1.3 μ_B (AFM) and 0.95 μ_B (DLM). We do not find symmetry breaking to lead to a significant change of site moments. As a contrast, we note local, Heisenberg models, often fit to spin-wave spectra, find very different J_{1a} and J_{1b} nearest neighbor exchange parameters with broken symmetry [101, 89]. We see, however, that magnetic disorder leads to a large reduction in site moments, due to transverse components of the magnetization. The time-averaged ordered moment is 0.9 μ_B from neutron diffraction [95], which have some transverse components. Using core-electron spectroscopy to probe short-time scales (10^{-15} sec), the measured moment is 2.1 μ_B in the closely related $SrFe_2As_2$ [153]. This difference has been attributed to modest electron correlations [98] and magnetic excitations.[35] We see here that the disordered component of the site moment is substantial. Overall, the KKR results agree reasonably with previously computed AFM site moments of 1.8 μ_B (I4/mmm) from FLAPW; the moments from PWP are 2.6 μ_B (Fmmm).

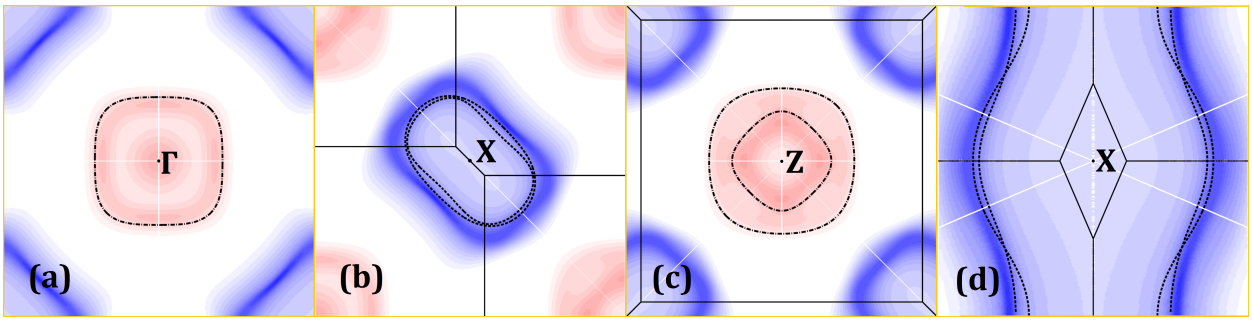

Figure 4.2: Bloch spectral function $A(\mathbf{k}, E)$ of $BaFe_2As_2$ in both NM and DLM states. Hole cylinders are depicted as dash-dot lines (NM) or false-color scaled red (DLM). Electron cylinders are dashed (NM) or blue (DLM). Solid lines indicate the BZ boundary. Cross-sections are normal to (a) [001] about Γ, (b) [001] about X, (c) [001] about Z, and (d) [$\bar{1}$10] about X. False coloring is mapped (in 10^3 states $Ryd^{-1}cell^{-1}$ $r.u.^{-3}$) as {0 ↔ RGB 0xFFFFFF (white), 100 ↔ RGB 0x770000 (light red), and 1000 ↔ RGB 0xFF0000 (red)} for hole pockets. And similarly for electron pockets. This choice was made to make as many features as possible visible across plots.

In this low-doping regime (e/Fe ≤ 0.18), the ΔE_f vary linearly with x or e/Fe for all magnetic states and structures. Furthermore, the resulting trends are robust whether considering the I4/mmm or Fmmm structures. In the NM state, there is a clear splitting in the behavior of Co- and Ni-BFA versus Cu- and Zn-BFA. Both Co- and Ni-BFA show the same, favorable formation energies for given e/Fe. Cu- and Zn-BFA also agree for given e/Fe but are unfavorable to mixing at zero temperature. Chemical mixing entropy does reduce formation enthalpies relative to endpoints $BaFe_2As_2$ and BaM_2As_2, increasing the favorability of the higher e/Fe compounds. In an ideal mixing model [159] this will reduce the free energy by 21, 13, 10, and 8 meV/atom for Co-, Ni, Cu-, and Zn-BFA at e/Fe = 0.18 and 1000 °C, a typical annealing temperature [139, 129]. This effect is not accounted for in the 0 K results in Fig. 4.1 so as to separate electronic (e/Fe) effects from entropic (dopant x) effects.

In the DLM state, a similar splitting persists, but energies are less pronounced. There is also less agreement in the energies of Cu- and Zn-BFA at a given e/Fe. We find no magnetic moments at the dopant atom and only marginally reducing moments on the Fe sites with increasing e/Fe. Neutron diffraction shows a rapid drop in Fe moment with doping [140]. This may be a result of the sensitivity of the moment to an increasing a lattice constant [72]. Experiments that demonstrate the incommensurability of the spin-density wave [140] on Co and Ni doping are done in the PM state. Cu-BFA does not become incommensurate. Our results show Cu mixing is, at best, weakly favorable. Thus, the lack of incommensurate splitting in Cu might arise not as a result of a FS effects, but rather due Cu clustering. In the AFM state, dopants decrease favorability relative to the PM state. This is in qualitative agreement with the known phase diagrams, where dopants suppress the AFM state and eventually lead to SC. The dopant species splitting here is even

less pronounced and all compounds follow nearly the same trend with e/Fe. This suggests an important difference in doping effects on the PM and AFM state. Note that prior DFT calculations for the doped compounds have been performed on the NM state [148, 147].

4.1.4 Fermi-Surfaces of PM States

Figure 4.2 shows the FS of NM and DLM $BaFe_2As_2$. NM surfaces are shown for electrons (dashed lines) or holes (dash-dot lines) – there is no FS broadening with no chemical disorder – and these surfaces agree with previous results. The Brillouin zone (solid lines) and labels correspond to the body-centered tetragonal lattice and can be found in the literature [83]. DLM surfaces for electrons (blue) or holes (red) show significant broadening due to local orientational disorder – in contrast to chemical disorder, which we see, below, is less significant. The approximate **k**-space broadening is 0.14 *r.u.* (reciprocal units defined as $2\pi/a$ units in **k**-space).

Note that DLM Bloch spectral peaks do not coincide exactly with the NM surface. The DLM hole (electron) pockets are reduced (enlarged) in size relative to the NM. This corresponds to an effective e-doping, as reflected in the DOS with a positive shift of E_F. The interior pocket near the Z point is pinched off near the Γ point. This can vary with choice of exchange-corrleation and lattice parameters. A strong pinching is also visible in prior DFT calculations [31] and ARPES [136, 85]. The outer cylinder is fairly uniform and gives rise to strong nesting with electron cylinders. The electron cylinders obey a 4_1 screw symmetry along the k_z-axis while the hole cylinders obey 90° rotational symmetry. The DLM broadening and E_F shift changes the strength of nesting between hole and electron cylinders. The large broadening can explain the reduced resolution of ARPES data, especially when compared to measurements made on CuO SCs.

To make a connection to nesting, we note that it is, in principle, possible to calculate the chemical, magnetic and magneto-chemical susceptibilities within the KKR-CPA using a thermodynamic linear-response theory [160], similar to phonon linear-response that uses infinitesimal displacements. For such susceptibilities in the high-symmetry (disordered) state, the correct functional form is $\chi^{-1}(\mathbf{q};T) \sim [1-\beta(1-m_i^2)S^{(2)}(\mathbf{q},T)]$, where $\beta = (k_B T)^{-1}$ and $S^{(2)}(\mathbf{q},T)$ is an exact second-variation of the electronic grand-potential with respect to fluctuations, e.g., site magnetizations. For an Ising-like system, $S^{(2)}(\mathbf{q},T)$ plays the role of a thermodynamically averaged pairwise $J(\mathbf{q})$. Such calculations have been done for solid-solutions [160, 161, 162, 163] and elemental FM [164] and AFM [165], but not yet for multi-sublattice cases.

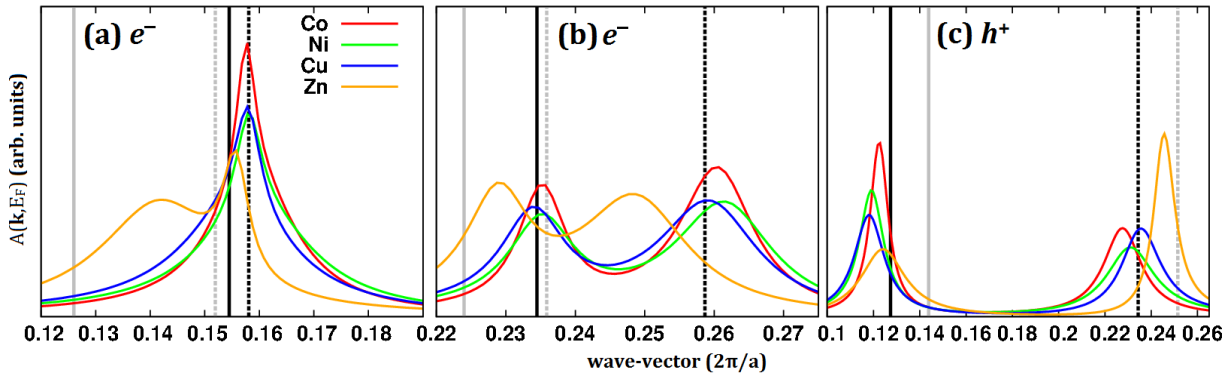

Figure 4.3: For NM Co-, Ni-, Cu-, and Zn-BFA at e/Fe = 0.10, the Bloch-spectral function $A(\mathbf{k}, E)$ along (a) X=[$\frac{1}{2}\frac{1}{2}$0] to Γ=[000] (electron), (b) X to Z=[010] (electron), and (c) Z to X (hole). These correspond to traversing the principal axes about the electron and hole cylinders. Black vertical lines correspond to rigid-band expectation at the same e/Fe: first (second) line is the inner (outer) cylinder. First (second) gray line is for the inner (outer) cylinder of parent BFA. Clearly, Zn is behaving differently than Co, Ni, Cu, or the rigid-band. In (c), hole states deviate notably from rigid-band behavior.

Nonetheless, $S^{(2)}(\mathbf{q}, T)$, with matrix elements $M(\epsilon)$ and Fermi factor $f(\epsilon)$, is a generalized susceptibility:

$$\begin{aligned} S^{(2)}(\mathbf{q};T) &\sim \int d\epsilon\ M(\epsilon) \int d\epsilon' \left[\frac{f(\epsilon;T) - f(\epsilon';T)}{\epsilon - \epsilon'}\right] \\ &\times \frac{1}{\Omega_{BZ}} \int d\mathbf{k}\ A(\mathbf{k};\epsilon) A(\mathbf{k}+\mathbf{q};\epsilon') \qquad (4.2) \\ &\to \int d\mathbf{k}\ A(\mathbf{k};E_F) A(\mathbf{k}+\mathbf{q};E_F). \qquad (4.3) \end{aligned}$$

In principle, all states in the valence contribute to (4.2). If only hole and electron states near E_F dominate, the bracketed factor [...] yields (4.3), which is a convolution of the Fermi surface states and the origin for "nesting" [152, 162]. Due to alloying, even in a metallic system, hybridized states well below E_F can drive ordering (NiPt [161]) or only features at E_F (CuPt [163]). For Cr, the NM state yields nesting with a incommensurate wavevector, as observed [54], while, for Cr-Ru the chemical disorder broadens the FS enough that the SDW now is commensurate, as observed, and coexists with SC.

This discussion was to motivate that the DLM state (with similar FS topology to the NM state) can create similar nesting due to larger volumes of the Brillouin zone contributing to the susceptibility integral, even though the peak overlap is reduced.

4.1.5 Fermi-Surface Nesting in NM State

We analyze the NM Fermi surface (electrons and holes) typically used for SDW stability analysis for a given e/Fe. A cross-section of $A(\mathbf{k}, E_\mathrm{F})$ for transition-metal alloys at fixed e/Fe = 0.10 are shown in Fig. 4.3 (in

r.u.), which traverses from the center of electron (hole) cylinders along principal axes $k_1 = [110]$ and $k_2 = [\bar{1}10]$. Only a range near the spectral peaks is shown in each case. The k-space broadening is $\Delta k \sim 0.03$ *r.u.*, much less than the DLM case. The NM rigid-band expectation corresponds to the vertical black lines, while the spectral peaks for the undoped-NM case are marked by vertical gray lines. For Co-, Ni-, Cu-BFA the peaks lie close to that of rigid-band for electron and hole pockets. Only Zn deviates, see Fig. 4.3. This suggests that Zn-BFA has a reduced electron-doping effect and less interaction with Fe and As bands. The reduction of effective e/Fe comes from the change in DOS due to the separation of Zn and Fe-host d states well below E_F, see DOS discussion below.

These effects are alternatively visible in Fig. 4.4, which shows the electron and hole FS at fixed e/Fe = 0.10 for Co, Ni, Cu, and Zn doping and compares to that expected from a rigid-band shift from the parent BFA. To show the potential convolution overlap for nesting, the electron surfaces have been shifted to align with hole cylinders for each doped compound. The shift used is the wave-vector connecting X to Γ, i.e., $\langle \frac{1}{2}\frac{1}{2}0 \rangle$. These plots show that the broadening at the Fermi energy is about the same across dopant species for a given e/Fe, as expected from Fig. 4.3. On doping the holes shrink and electrons grow. This improved "nesting" (or overlap) leads to a transverse splitting of the nesting vector along $[1\bar{1}0]$, as observed for Co- and Ni-BFA [140]. The Zn FS is sharper, indicating longer electron lifetimes. It is visibly shifted from rigid-band expectations, as in Fig. 4.3.

Electron states in Fig. 4.3(b) [4.3(a)] correspond to the vertical $\langle \bar{1}10 \rangle$ [horizontal $\langle 110 \rangle$] direction in Fig. 4.4 when traversing from the center. The convolution arises from the entire FS and depends on the broadening and similar widths of spectral features, which increase phase-space overlap volume; but, from the two electron peaks in Fig. 4.3(b) and second hole peak in (c) we can make an eye-ball estimate of the incommensurability expected from nesting at E_F from Eq. (4.2). Note that in (c) no hole states reflect rigid-band behavior. For Co-doping, the estimate is 0.01 [0.03] in $2\pi/a$ units, spanning that observed value [140]. For Ni, it is 0.01 [0.03], again spanning that observed. For Cu, it is near 0 [0.02]. For Zn, it is -0.02 [+0.01], but the two Zn spectral features are not well separated, smearing the convolution.

Notably, ARPES finds a disagreement between rigid-band lines and the FS of Cu-BFA [85], and no FS changes for Zn-BFA [141]. However, a DFT study using supercells found a significant shift in the FS of Zn-BFA [147], but the FS shows considerably more broadening than visible here. Thus, there is an apparent discrepancy in electron itinerancy and effective doping between DFT theory and ARPES. Our calculations too show that Zn FS does not coincide with that of the parent compound, Fig. 4.3, and the volume spanned by the electron surface are reduced compared to that expected from rigid-band, see Fig. 4.4. In fact, for the e/Fe of 0.10, the effective e/Fe is closer to 0.05 (a 50% reduction) from direct calculations; an eye-ball

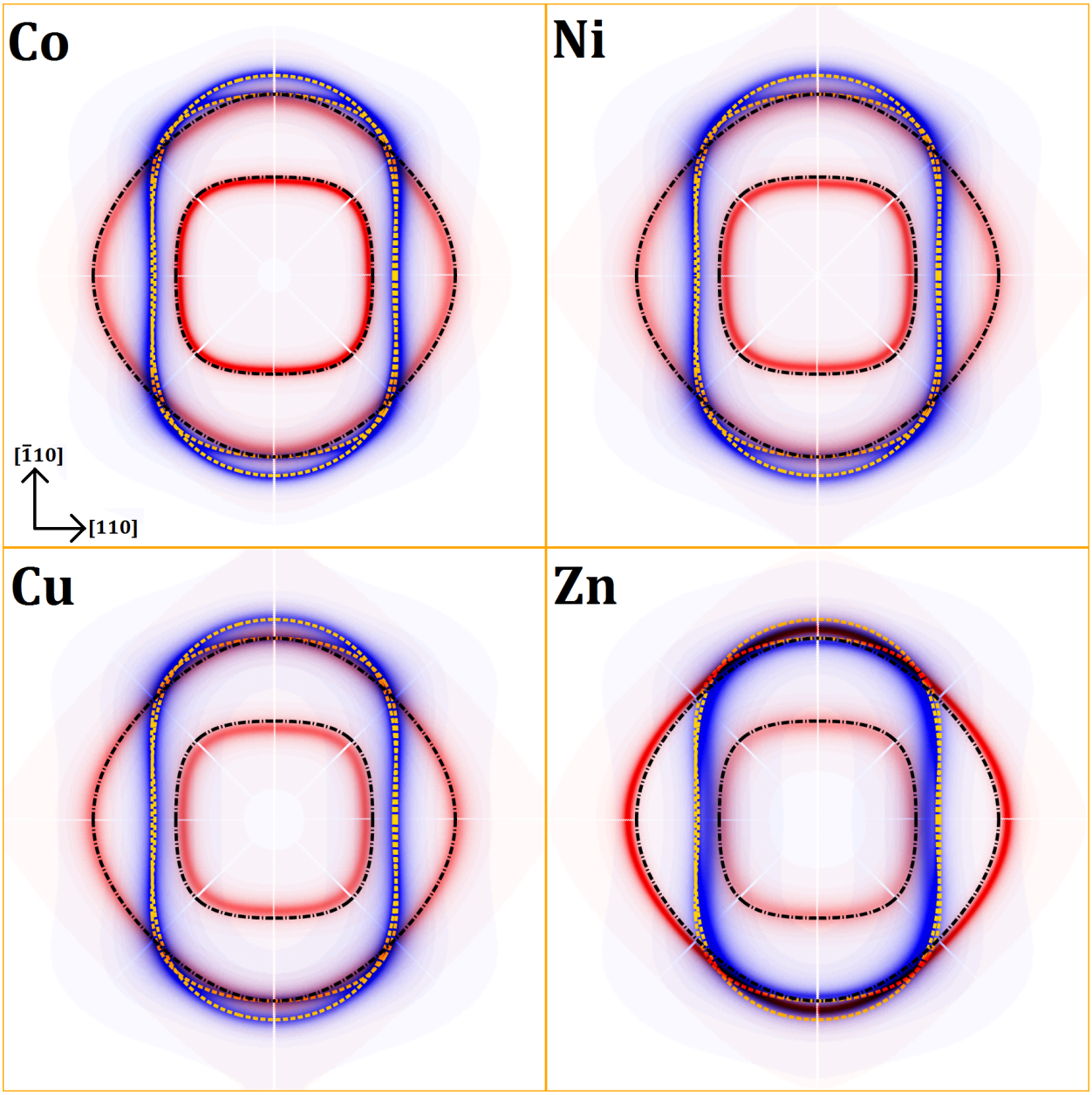

Figure 4.4: Overlapped electron (blue) and hole (red) pockets of NM doped compounds at e/Fe = 0.10. FS for rigid-band shifted NM at the same e/Fe are shown as dashed lines (gold) for electron and dash-dot (black) for hole cylinders.

estimate from Fig. 4.3 shows that the Zn spectral peaks are center between the vertical solid lines or the vertical dashed lines, which is expected for a rigid-band with e/Fe of 0.05, as calculated.

A warning to the reader, quantitative agreement with the experimental ARPES spectra from DFT electronic structure can be more reliably obtained by performing realistic photocurrent calculations that include a proper treatment of the surface electronic structure, energy-dependent matrix elements and lifetime effects, as has been done in KKR [166, 167]. For s-polarized light, for example, the surface can play only a minor role in photoemission and the measured spectra may follow the DFT quasiparticle dispersion. Otherwise the energy-dependent matrix elements, e.g., from Fermi's "Golden Rule" involving photocurrent and the single-site wave-functions, affect the calculated spectra from DFT dispersion. In short, the DFT electronic structure does not necessarily have one-to-one correspondence to that from ARPES, but sometimes it does. So, our above results may all be correct, but, in the future, a more careful comparison is needed with ARPES.

4.1.6 Density of States and Band Filling

For $BaFe_2As_2$ the valence DOS for NM, DLM, and AFM states are shown in Fig. 4.5, relative to their respective Fermi energies, E_F. The AFM DOS per primitive (i.e., NM) cell are used to ease comparison. From -6 to -3 eV there is strong similarity of the states, but with a shift of E_F due to a pseudo-gap forming below E_F for AFM state and, more weakly, for the DLM state. This shift is $+42$ meV (DLM) and $+126$ meV (AFM) relative to the NM. From -2 to 1 eV the DLM states are significantly broadened to due local spin disorder. Note the average slope for NM and DLM states near the Fermi level is negative. This can explain the apparent Fermi level shift of the DLM visible in Fig. 4.2. The negative slope and disorder broadening together result in a net reduction in filled states as disorder is turned on. This is compensated by an increased Fermi level. The AFM state shows the opening of a pseudo-gap below the Fermi level, which also explains a large positive shift. The density of states at E_F (i.e., $n(E_F)$) are 5.0, 5.2, and 4.8 states-cell^{-1}-eV^{-1} for NM, DLM, and AFM, respectively.

For the doped cases of $Ba(Fe_{1-x}M_x)_2As_2$, we focus on the valence DOS for NM states versus M in Fig. 4.5b. The Fe site-projected DOS do not change for all species M (they clearly lie on top of each other). There is significant overlap of Co and Ni site-projected DOS with Fe-site DOS (common-band behavior), there is clearly a split between states (split-band behavior) on Cu,Zn and Fe (Zn d-states are well below -6 eV and are not shown). These site projections agree with core-electron spectroscopy.

The shift for each dopant's d-states relative to Fe arises from the increasing ΔZ, where by $\Delta Z_{Cu} = +3$ the d-states are no longer in common energy range as Fe. With $\Delta Z_{Zn} = +4$ change in nuclear charge from

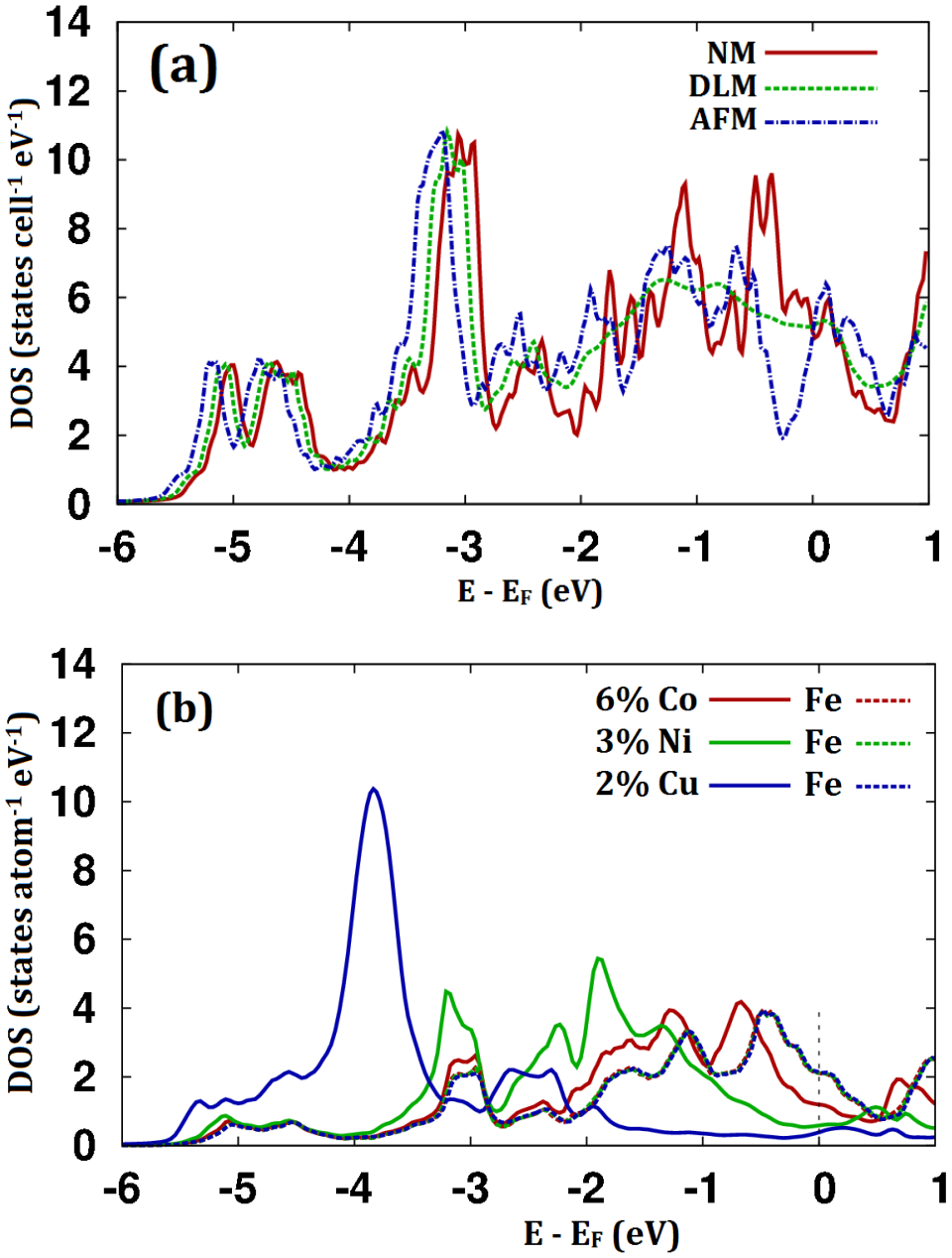

Figure 4.5: DOS relative to E_F for (a) $BaFe_2As_2$ NM, DLM, and AFM states, and (b) $Ba(Fe_{1-x}M_x)_2As_2$ M- or Fe- site-projected DOS for fixed e/Fe=0.06 (i.e., 6% Co, 3% Ni, and 2% Cu). Fe-DOS unaffected by choice of dopant. Zn states are below -6 eV with no overlap to Fe-As valence.

Fe, the Zn d-bands shifts lower in energy creating a split-band (relative to Fe), as will be evident in the DOS, leading to stronger difference in d potentials between Fe and Zn (less so for Cu). The common band behavior of Fe and Co,Ni leads to weak impurity scattering and a limited effect on electronic lifetimes and band structure. Conversely, the split band character of Fe and Cu,Zn leads to strong scattering. These electronic effects are reflected in ΔE_f trends for PM states in Fig. 4.1, where both Cu and Zn have positive ΔE_f (unfavorable to mixing with Fe) but Zn less so due to the separation of Zn and Fe-host d states well below E_F. This changes the overall energetics and outlines the origin for deviations of Cu,Zn formation energies from Co,Ni in the PM state.

In summary, using the all-electron KKR-CPA within DFT, we examined the phase stability, electronic structure, and Fermi-surface evolution of $Ba(Fe_{1-x}M_x)_2As_2$ (BFA) with M=Co, Ni, Cu, Zn for nonmagnetic, paramagnetic, and antiferromagnetic states in high-T tetragonal and low-T orthorhombic structures. Hence, both chemical (alloying) and magnetic (orientational) disorder was addressed. Properties were assessed in terms of additional electrons-per-Fe (e/Fe), expected from Hume-Rothery or rigid-band-like behavior. The paramagnetic phase was approximated by a single-site, disordered local moment state that has a finite, randomly oriented moment on each site, which is in contract to the NM state with zero moments. Magnetic effects are pronounced, leading to significant broadening of the Fermi surface and, so, a reduction in coherent carriers; yet, DLM is expected to support the same Fermi-surface nesting effects as from the NM. For the NM state, typically assessed for Fermi-surface nesting instabilities, we find differences versus nominal e/Fe in the formation energies, electronic structure, and Fermi-surface properties for Co- and Ni-BFA versus Cu- and Zn-BFA, due to well-known "split-band" behavior. Notably, while Cu-BFA deviates from rigid-band in its formation energetics, it continues to follow the rigid-band expectation in the Fermi-surface evolution; but, Zn-BFA does not follow rigid-band in either formation energetics or Fermi surface behavior; we showed that Zn has an effective e/Fe that is 50% of that expected from rigid-band theory due to alloying effects. This systematic assessment of the electronic properties for all competing states and structures in BFA should help resolve conflicting interpretations based different experiments and theories. Yet, for better comparison to experiment photoemission current calculation using the DFT dispersion would be the best.

4.2 (Ba-K)Fe_2As_2: Lifshitz transition and chemical instabilities

Superconductivity in Fe-based superconductors (Fe-SCs) is achieved by chemical substitution or applied pressure to tune geometry and charge.[16, 12, 168, 14, 17, 169] Lifshitz transitions can mark the onset of SC [170, 171, 137]. Among Fe-SCs, $Ba_{1-x}K_xFe_2As_2$ (BKFA) stands out for featuring a number of anomalies

in the heavily over-doped (HOD) regime, including an apparent Fermi-surface transition, and violation of "universal" trends found in most Fe-SCs. Making homogeneous samples of HOD-BKFA has proven difficult, which has not been explained. Reliable comparison of electronic properties between various experiments has also been an issue.

For non-magnetic, tetragonal ($I4/mmm$) BKFA, we use DFT to detail the Fermi-surface topology and character, and locate dissolution of electron pockets and onset of hole blades. The Fermi- surface is mapped from over-doped x $\geq$ 0.6, and exhibits a Lifshitz transition near x = 0.9. In Fe-SCs, the $s^{\pm}$ gap symmetry is considered closely tied to intra-band transitions among hole and electron surfaces [172, 173]. The loss of these transitions in HOD-BKFA could result in a weakening of spin-fluctuation-mediated pairing and signal competition with orbital fluctuations. Formation energies are calculated for all x, which show chemical instabilities at both under-doping and heavy over-doping. The instabilities highlight the difficulty in preparing uniform samples, explaining the discrepancies between various observed electronic structure. We verify that paramagnetism given by "disordered local moment" (DLM) state exhibits similar behavior, with no change in conclusions.

Common FeSCs features/trends have been identified. The electronic structure is a hybridization of Fe $3d$ and As $4p$ orbitals, which is sensitive to lattice parameters and internal (Fe-As) coordinates. At the experimental lattice parameters, the DFT Fermi-surface of the paramagnetic state often exhibits two or three hole cylinders at the zone center (Γ point) and two electron cylinders at the zone corner (X point), which agree well with angle-resolved photo-emission (ARPES), e.g., for LiFeAs (LFA), $BaFe_2As_2$ (BFA), and LaFeAsO (LFAO) [91, 31, 45, 39]. This electronic structure plays a key role in defining the magnetic and SC groundstates. In BFA and LFAO there is prominent (π,π) nesting between hole and electron cylinders, in correspondence with the observed antiferromagnetic (AFM) ordering [40, 174]. Moreover, when nesting becomes imperfect, as in $Ba(Fe_{1-x}Co_x)_2As_2$ (BFCA), the magnetic ordering becomes incommensurate spin-density wave [140]; in LFA, where nesting is absent, the ground state is non-magnetic.[45] Also, spin fluctuations (SF) in this mode have been correlated to SC [104, 137]. Taking this SF as the dominant pairing mechanism requires an $s^{\pm}$ gap symmetry, i.e., cylindrical nodes [172], as also evidenced from a resonance in spin susceptibility.[175, 176, 177] Further universality includes a common trend between the As-Fe-As bond angle and the critical temperature T_c [28], and the linear BNC scaling [109], i.e., specific heat jump $\Delta c_S \propto T_c^3$.

In KFe_2As_2 (KFA) there are well-defined vertical line-nodes on one of the hole cylinders and a total dissolution of electron pockets [178], and hole-blades appear about X [179]. Application of pressure shows critical behavior in the T_c response [180]. Universal heat-conduction is suggestive of a d-wave symmetry

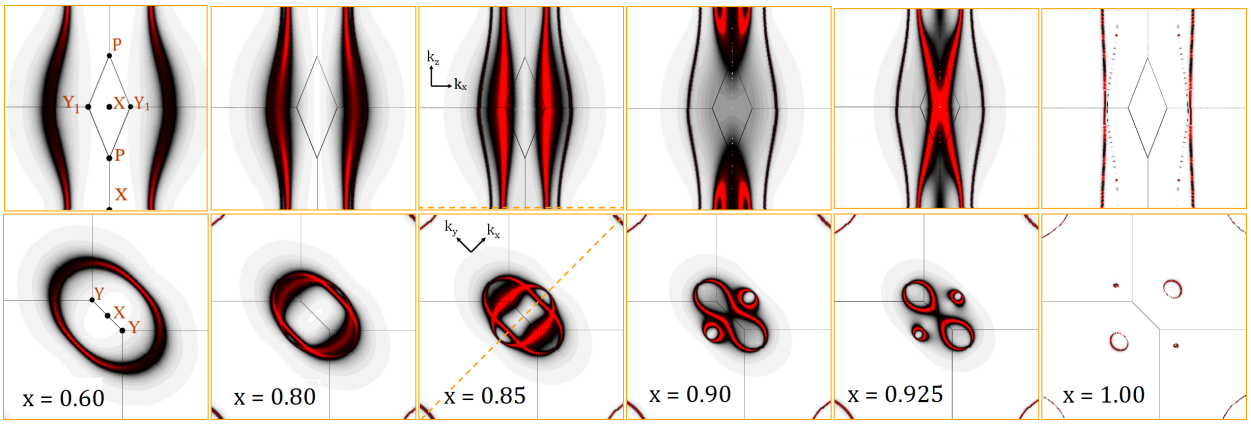

Figure 4.6: $Ba_{1-x}K_xFe_2As_2$ Fermi-surface evolution of electron cylinders versus K content. Intensity is in units of 10^3 states $Ryd^{-1}cell^{-1}$, with scale bar in Fig. 4.7. Top [bottom]: Bloch spectral function along (010) [(001)] planes in k-space. Solid lines indicate BZ boundaries. Thick dashed lines indicate corresponding cuts between top and bottom panels.

and possibly a neighboring quantum critical point [65, 181, 66, 182]. The K concentration (x) at which this transition occurs and what characterizes the transition is still under debate. In one study BKFA fails to follow the BNC scaling at x = 0.7-0.8 [183] An ARPES study sees an abrupt change in the gap magnitude occurring near x = 0.6, simultaneously with a Lifshitz transition [184]. Still other studies continue to see electron pockets without hole blades at x = 0.7 and estimate a transition at x = 0.8-0.9 [185]. Andreev reflection finds no transition up to x = 0.77 [186]. And, some studies see hole blades as early as optimal doping (x=0.4) [187], and others do not [188]. Complicating measurements is the instability of homogeneous samples at HOD and low T_c [60].

The BKFA phase-diagram ($0 \leq x \leq 1$) is known [29, 189]. BFA is a compensated metal in a low-temperature $Fmmm$ structure with striped AFM [40]. KFA is a non-magnetic SC in $I4/mmm$ structure exhibiting only hole carriers [179]. Optimal doping is achieved at x = 0.4 with T_c = 38 K. A co-existence between AFM and SC exists for $0.1 < x < 0.25$, though evidence suggests this is due to inhomogeneity in the sample [29]. Optimal doping has the hallmarks of an FeSC, including nested hole and electron cylinders and $s^{\pm}$ gap symmetry [190, 188]. Nested surfaces have the same energy gap, suggesting active transitions between these states [173]. Stearic effects, e.g., As-Fe-As bond angle, can account for optimal doping at x = 0.4, where $FeAs_4$ form ideal tetrahedra, and also for diminishing T_c with $x > 0.4$ [29]. However, it does not explain the transition to nodal SC and other HOD anomalies.

Table 4.2: For each sphere, Wyckoff ($I4/mmm$) positions and coordinates in face-centered cell with Ba at the corners.

E1	2b	(0.5000a, 0.0000a, 0.0000c)
E2	4e	(0.0000a, 0.0000a, 0.2072c)
E3	16m	(0.2007a, 0.0000a, 0.1715c)

4.2.1 Computational Details

DFT calculations were performed using an all-electron, KKR-CPA Green's function method [4, 5, 6]. The methods applied here have explained the spin-density wave behavior and scattering data in $Ba(Fe_{1-x}M_x)_2As_2$ versus solute (M=Co, Ni, Cu) [140], and the quantum criticality in $NbFe_2$ from an alloying-mediated Lifshitz transition at an unconventional band critical point [191]. To improve the basis set, empty spheres (E1, E2, and E3) were inserted in the structure (Table 4.2). Sphere sizes were maximized in the order Ba, Fe (=As), E1, E2, and E3. The same sphere positions were used for the orthorhombic ($Fmmm$) structures. All results were obtained with a 16×16×16 Monkhort-Pack k-point mesh for Brillouin zone (BZ) integrals [155], and using complex energy (E) contour integration with 25 E-points on a Gauss-Legendre semi-circular contour [156]. The valence configurations were taken as Ba $5p^6 6s^2$, K $3p^6 4s^1$, Fe $4s^2 3d^6$, and As $4s^2 4p^3$. Fermi energies were determined via the analytic Lloyd's formula for an accurate electron count.[192] To avoid DFT sensitivity to structure, we used measured structural parameters versus x for both $Fmmm$ and $I4/mmm$ structures [189]. However, for $I4/mmm$, the experimental data is limited versus x, but shows that Vegard's law [193] is invalid. But, two linear regimes match experiment well: (1) from $x = 0 - 0.3$, and (2) from $x = 0.3 - 1.0$.

Fermi-surfaces are determined via the Bloch spectral function $A(\mathbf{k}, E) = -\frac{1}{\pi} \operatorname{Im} G(\mathbf{k}, \mathbf{k}, E)$, where G is the single-particle Green's function. $A(\mathbf{k}, E)$ is the E- and $\mathbf{k}$-space resolved density of states and dispersion. In the limit of an ordered compound it reduces to Dirac δ-functions that define the band structure $E(\mathbf{k})$. For $x \neq 0$ or 1 there is $\mathbf{k}$-dependent spectral broadening and shifting due to chemical disorder (impurity scattering) handled via the CPA. The spectral full-width at half-maximum with respect to energy is inversely proportional to the lifetime of electronic states.

4.2.2 Lifshitz Transition

For $Ba_{1-x}K_xFe_2As_2$ ($x \geq 0.6$), we find a Lifshitz transition in the Fermi-surface evolution (Fig. 4.6), as is clearly evident at the X-point near $x = 0.9$. Spectral intensity is scaled according to a false color map given in Fig. 4.7a. The BZ with high-symmetry labels is provided in Fig. 4.7a. Cross-sections in Fig. 4.6 are along k_x-k_z (top) and k_x-k_y (bottom) plane. A corresponding cut in both planes is shown as a dashed line

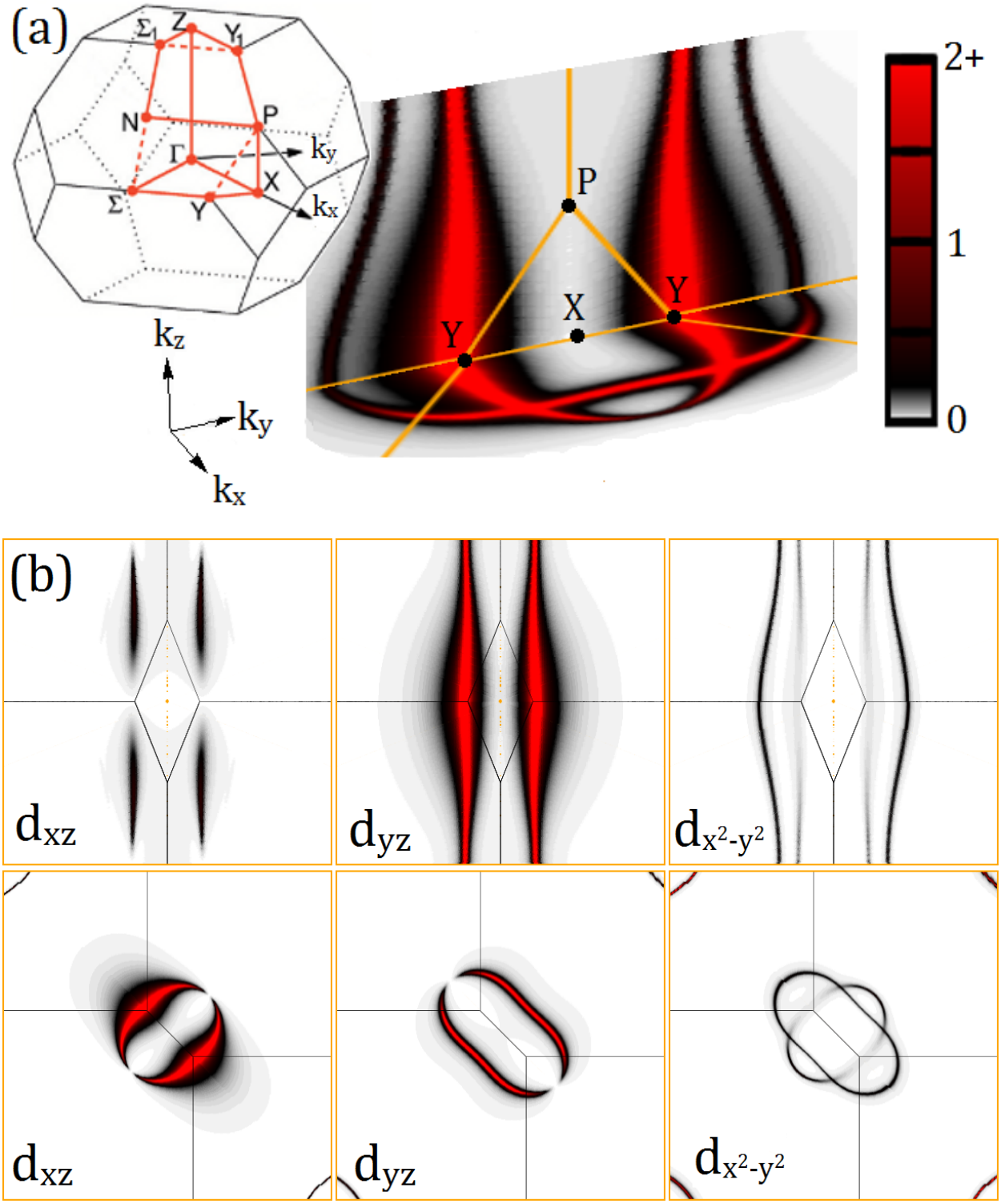

Figure 4.7: (a) Fermi-surfaces near X-points (3D perspective) for non-magnetic, tetragonal $Ba_{0.15}K_{0.85}Fe_2As_2$ in units of 10^3 states $Ryd^{-1}cell^{-1}$. Cylinder-like electron sheets are evident. Inset shows BZ with symmetry labels (the BZ height shrinks as x increases). (b) Electron cylinders are decomposed into Fe-site orbital projections. x- and y- directions in real-space coincide with neighboring Fe-Fe bonds in the Fe square net. Spectral intensities projected by character do not follow the symmetry of the crystal.

at x = 0.85. A 4_1-screw symmetry along k_z is obeyed at the X point.

As BKFA approaches KFA (i.e., x $\rightarrow$1), holes centered at Γ grow and electrons at X shrink. Near the critical concentration $x_c = 0.9$ the electrons disappear and hole blades appear. We find from x = 0.6 to 0.85 the electron pockets have shrunk without topological change. Just before the transition the bands flatten. Each electron pocket maintains its own character (c.f. Fig. 4.7) and undergoes transitions separately. The electron cylinder with major axis along k_x splits first between $0.85 < x < 0.90$. Three dimensionality at x = 0.9 is apparent in the top frame. Hole pockets then appear lateral to X. The second electron cylinder with major axis along k_y undergoes a split between $0.90 < x < 0.925$. Subsequently, two additional hole cylinders are established just before x = 1, and at the endpoint all Fermi-surfaces are hole-like. The density of states n(E) is not peaked at the Lifshitz point, suggesting a more involved relation to SC.

For further perspective, at x = 0.85, just before the Lifshitz transition, we plot the orbital decomposition (Fig. 4.7b) and the dispersion (Fig. 4.8). The evolution of the transition can be more reliably ascertained at this concentration (rather than the end compounds) by shifting the Fermi energy (E_F) in Fig. 4.8 up across the Lifshitz transition (e^- doping) or down (h^+ doping). The "band" broadening is ∼50 meV in energy, comparable to the band shifts needed to match DFT and ARPES [12]. The k-space broadening is ∼0.03 reciprocal lattice units. The electron and hole pockets are osculating; the dissolution of electrons and appearance of holes is nearly simultaneous. Traveling from Γ to X across E_F, the first three band crossings correspond to hole cylinders about Γ. The next two crossings represent either the outer and inner e^- pockets about X (above E_F), or a single hole cylinder (below E_F). Similar crossings occur traveling from Z to X. The "bands" that cross E_F arise from Fe 3d orbitals. The character of electron pockets (Fig. 4.7b) is majority d_{xz} and d_{yz} character, with some $d_{x^2-y^2}$ hybridization. There is a modest d_{z^2} hybridization on the middle band of the hole pocket about Γ (not shown), which compares favorably to line nodes on this hole cylinder found in ARPES.[178] However the experiment places the d_{z_2} band closer to E_F, and crossing at KFA. The $d_{x^2-y^2}$ correspond to direct Fe-Fe σ-bond.

4.2.3 Chemical Instabilities

Finally, formation energies (ΔE_f) for $Ba_{1-x}K_xFe_2As_2$ solid solutions at 0 K are shown in Fig. 4.9. A negative ΔE_f indicates that the sample is more favorable than segregating to the endpoint compounds; however, only those alloys below Maxwell tie lines are globally stable at 0 K, e.g., x = 0.35, which is close to optimal doping and where $FeAs_4$ form ideal tetrahedra. This stability is likely enhanced by spectral peak overlap of the two electron cylinders about X near x = 0.4 (Fig. 4.11). At small x, we find, as observed, the orthorhombic phase is more stable than the tetragonal phase. Tetragonal solid solutions whose ΔE_f lies above the Maxwell

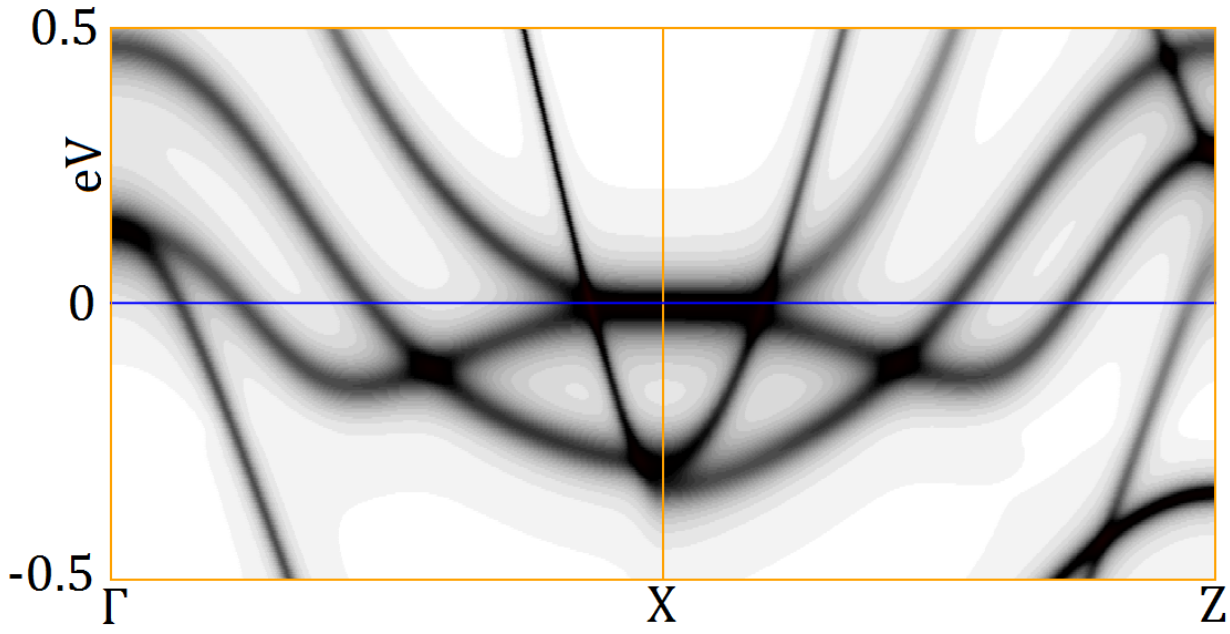

Figure 4.8: Electronic dispersion (Bloch spectral functions) of $Ba_{0.15}K_{0.85}Fe_2As_2$ near Fermi energy (0 eV) from Γ=[000] to X=[100] to Z=[110]. Spectral broadening is evident.

tie line are unstable at 0 K to a mixed compound formed from concentrations at the endpoints of the line segment on the tie line. The Maxwell tie line consists of two segments: one from x = 0 to 0.35 and another from x = 0.35 to 1.0. This unusual curve reflects in part the variation of the lattice constants versus x, whose slopes change near x = 0.3, see Fig. 4.12. For under-doping (0.15–0.3) the high-T, tetragonal phase form is slightly unstable to segregation, in agreement with experiment [183]. At non-zero temperatures entropy will favor the disordered states. To account for this, the free energy [159] at the experimental annealing temperature of 1000 K is also shown in Fig. 4.9, which exhibit similar behavior to ΔE_f(0 K). While the most stable (global) configuration for x$\geq$ 0.35 should be an admixture of $Ba_{0.65}K_{0.35}Fe_2As_2$ plus KFe_2As_2, the free energy difference to drive this diffusion-limited state is weak, which explains the large range of concentrations in samples and conflicting reports on properties. For x > 0.6, there is a stronger segregation instability, with a maximum near x = 0.8 (Fig. 4.9 inset). Experiments indicate a possible miscibility gap from x = 0.64 to 0.82 at a growth temperature of 1000 °C [194].

For completeness, in Fig. 4.9 we include calculations of ΔE_f(0 K) versus x for the paramagnetic DLM state in which Fe moments of 1.0 μ_B are randomly oriented, from a self-consistent electronic structure with spin disorder. These results show very similar energetics to the non-magnetic ones, indicating both paramagnetic states lead to similar results. Either way, our formation energy results certainly clarify some of the difficulty of controlling sample composition and quality, which is reflected in the associated conflicting

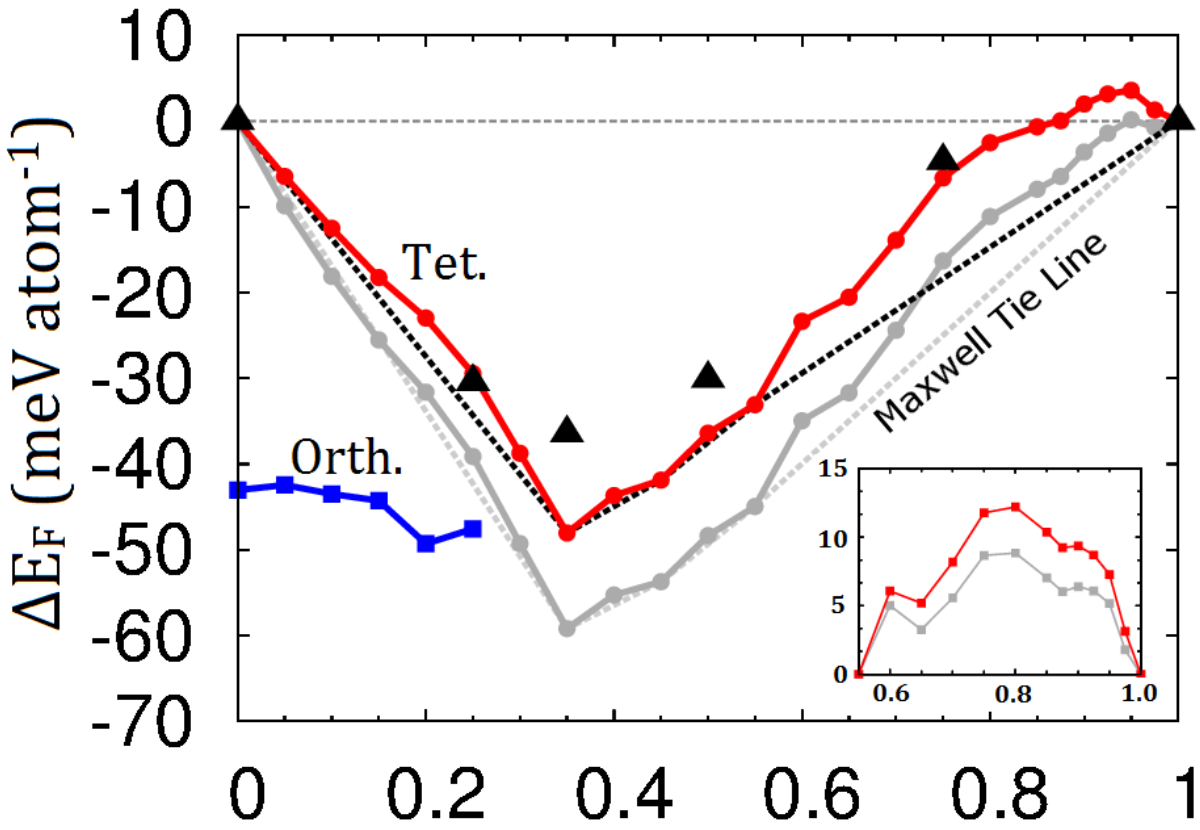

Figure 4.9: ΔE_f(0 K) versus x (red symbols/lines) for $Ba_{1-x}K_xFe_2As_2$, relative to endpoint alloys. The Maxwell tie (dashed) lines are indicated. At 1000 K, the free energy (grey line), using ideal mixing entropy [159], follows the 0 K behavior. At the Ba-rich side, orthorhombic $Ba_{1-x}K_xFe_2As_2$ (blue symbols/lines) is favored, as observed. The DLM states (triangles) show similar behavior to the non-magnetic cases. Inset shows ΔE_f relative to tie line between $x = 0.55$ and 1, exhibiting local instability to segregation with maximum at x$\sim$0.8 for $0 - 1000$ K.

results on experimentally characterizing the electronic structure of BKFA.

More ARPES studies in this regime, and indirect bulk measurements of the Lifshitz transition, such as the Hall coefficient, would connect directly to our results. A reversion from nodal SC to standard $s^{\pm}$ may occur under the application of pressure to KFA [180]. This may also be due to a Lifshitz transition, as electron doping has been found to correlate with pressure for FeSCs [195]. Studying the Fermi-surface response to pressure to see if a Lifshitz response can be ruled out may resolve this. However, the response of T_c with e^- doping is continuous, while response under pressure is discontinuous, suggesting these changes have different origins.

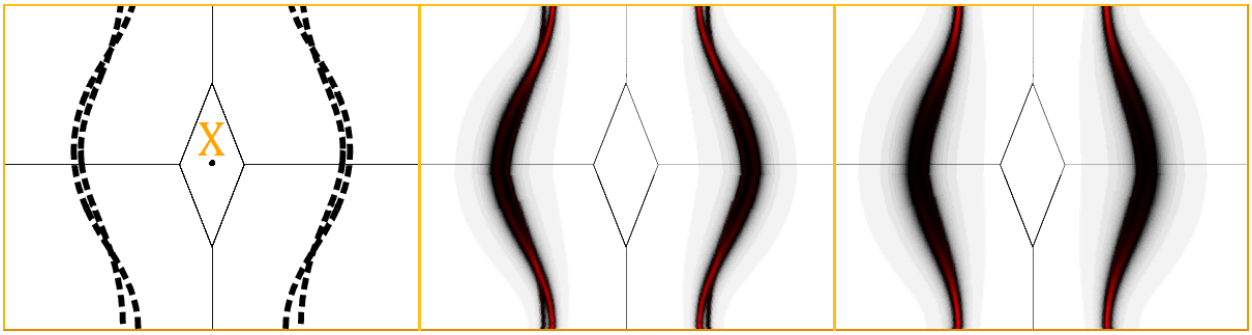

Figure 4.10: Fermi-surface evolution of $Ba_{1-x}K_xFe_2As_2$ electron cylinders in the (010) plane versus K content x= 0, 0.2, and 0.4. Intensity units, BZ boundaries, and false-color map are given in Fig. 4.7.

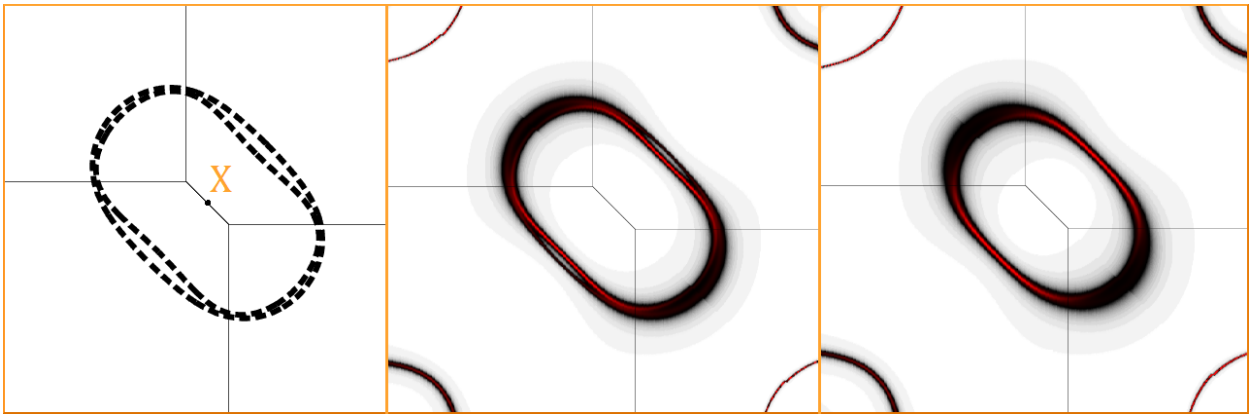

Figure 4.11: $Ba_{1-x}K_xFe_2As_2$ Fermi-surface evolution of electron cylinders in (001) plane versus K content for x= 0, 0.2, and 0.4.

4.2.4 Low Concentrations and Structural Cell Parameters

For completeness, we provide the non-magnetic, tetragonal BKFA Bloch spectral function $A(k, EFermi)$ at x= 0, 0.2, and 0.4 in both the (010) and (001) k-space planes (c.f. Figs. 4.10 and 4.11). We include the total density of states for three K concentrations (c.f. Fig. 4.13). We show also the deviation from Vegards law for the tetragonal system, permitting good agreement with experiment for two linear fits versus x for the tetragonal structural parameters (c.f. 4.12). As is clear the Fermi-surface topology remains that for $BaFe_2As_2$, with only a modest reduction of the electron cylinders is visible from x=0 to 0.4. Comparing the Fermi-surface evolution here with Fig. 1 for the Fermi-surface with x = 0.6 to 1.0 shows that there is a clear Lifshitz transition near the critical K concentration of 0.9.

The density of states (Fig. 4.13) exhibits a peaked structure at -3 eV in BFA that is substantially diminished in KFA. The $Ba_{0.5}K_{0.5}Fe_2As_2$ density of states is approximately a weighted average of the endpoint compounds with broadening and spectral shifts due to chemical disorder on the Ba sublattice.

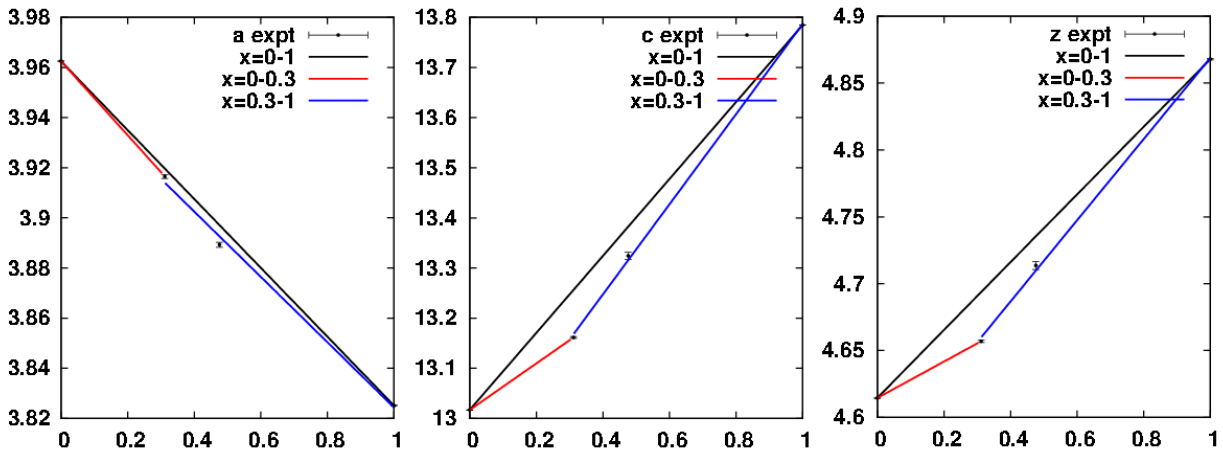

Figure 4.12: Structural parameters a, c, and z (in Å) versus K content for $Ba_{1-x}K_xFe_2As_2$. Error bars indicate experimental error due to composition and diffraction measurements.

Finally, the measured structural parameters for tetragonal alloys versus x are provided (c.f. Fig. 4.12). Notably, Vegards law (linear variation for x = 0 to 1) is invalid; yet two linear fits for x = 0 to 0.3 and x = 0.3 to 1 provide reasonable agreement to experiment, which brings the error below the sensitivity of DFT. In experiment, there is a direct error from the diffraction measurement and an error due to uncertainty in the composition, see Fig. 4.12. The existence of two regimes is likely tied with the onset of the low-T orthorhombic structure. Note that the inflection point in the formation energy is at x = 0.35, not x = 0.3; therefore, while there may be a connection between the concentration variation of the lattice parameters and inflection point, it is not a direct one.

4.2.5 Concluding Remarks

In summary, among FeSCs, BKFA is of particular interest because it undergoes a transition at heavy over-doping that has yet to be fully understood, and deviates from known FeSC trends. Making homogeneous samples in this concentration range has proved difficult, as explained via our results on stability. Using KKR-CPA methods, we have gone beyond the rigid-band approximation to explore the full concentration range. We find a Lifshitz transition near x = 0.9 that occurs in parts; both electron cylinders disappear at slightly different x. The Lifshitz transition marks a reduction of inter-band transitions and likely a weakening of SF-mediated pairs. Orbital character of the dispersion near the transition is strongly pronounced, unlike that observed on the under-doped side.[91] This may suggest increased competition of spin and orbital fluctuations; there has been SFs observed in KFA at the (π,π) mode [196]. We also find the electronic disorder broadening is comparable to band shifts required for DFT to ARPES to match. The Lifshitz

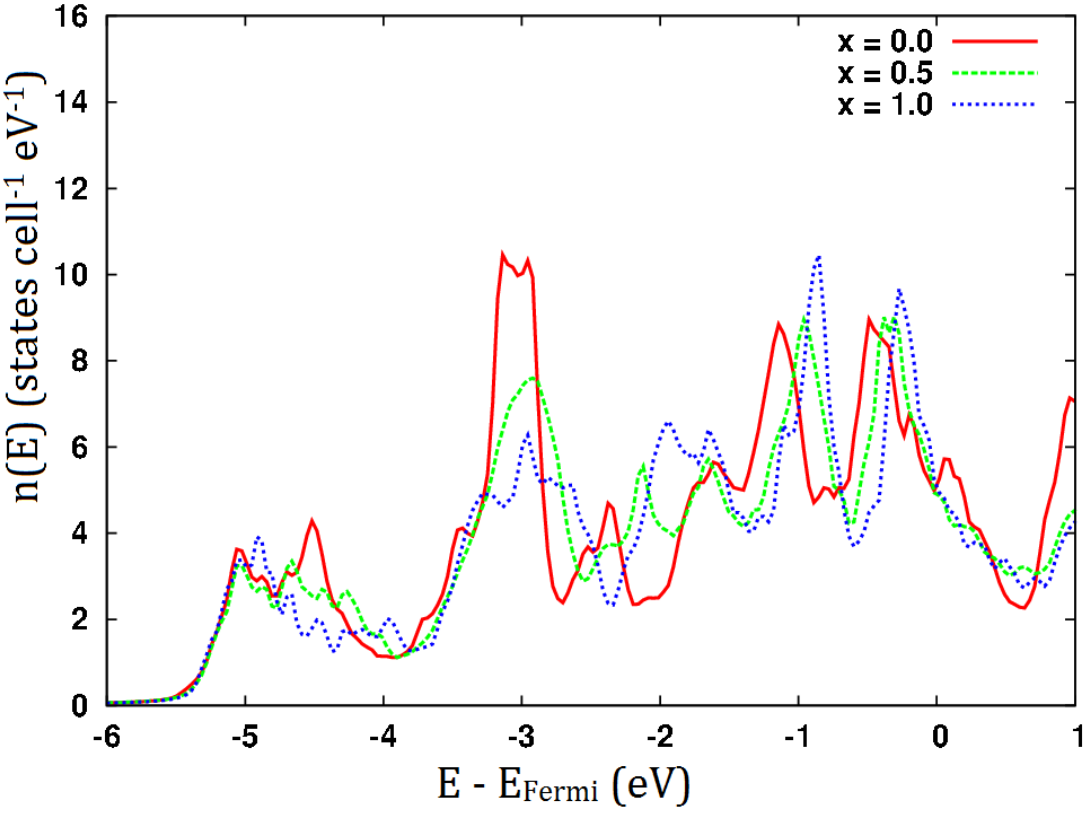

Figure 4.13: Total density of states for $Ba_{1-x}K_xFe_2As_2$ at x = 0, 0.5, and 1.

transition behavior detailed here also suggests an explanation for the observed deviation from the linear BNC scaling [109].

More ARPES studies in this regime, and indirect bulk measurements of the Lifshitz transition, such as the Hall coefficient, would connect directly to our results. A reversion from nodal SC to standard $s^{\pm}$ may occur under the application of pressure to KFA [180]. This may also be due to a Lifshitz transition, as electron doping has been found to correlate with pressure for FeSCs [195]. Studying the Fermi-surface response to pressure to see if a Lifshitz response can be ruled out may resolve this. However, the response of T_c with e^- doping is continuous, while response under pressure is discontinuous, suggesting these changes have different origins.

Chapter 5

Stability of Magnetic Defects

Fe-based superconductors (FeSCs) provide another avenue to understand unconventional superconductivity.[16, 17, 169, 14, 12] Due to its ease of synthesis, $BaFe_2As_2$ is a prototype for these systems, where its low-temperature (T < 140 K) ground state is a striped, antiferromagnetic (AFM) orthorhombic ($Fmmm$) structure,[40] often called a spin-density wave (SDW), and which is reproduced in Density Functional Theory (DFT) calculations.[31] At Neél T_N (140 K), both a magnetic and structural transition occurs to a tetragonal ($I4/mmm$) paramagnet.[40] By doping with a transition-metal on the Fe-site or others on Ba- and As-sites, superconductivity (SC) can be achieved, and similarly with pressure.[128, 129, 74, 197]

There are strong connections between the magnetism and SC. Dopants weaken the magnetic state and Cooper pairing is, perhaps, driven by increased magnetic fluctuations out of the ground state.[198, 199] DFT has proven successful in modeling the geometry, magnetic ordering, and electronic structure of FeSCs. The magnetic ground states of LaFeAsO, $BaFe_2As_2$, NaFeAs, and FeTe are all correctly predicted.[32, 31, 200, 201] Fermi-surface (FS) nesting is apparent from DFT calculations and agrees with angle-resolved photoemission (ARPES), suggesting an itinerant nature[82, 85, 135] and which is supported from the spin-wave dispersion.[101, 202] Furthermore, DFT explains quantitatively effects of doping on FS nesting, and why Cu doping behaves differently than Co and Ni.[140] $K_xFe_2Se_2$ (isostructural to $BaFe_2As_2$) does not have the hole pockets needed for FS nesting,[47] as DFT finds.[203]

DFT results for $BaFe_2As_2$ show a strong coupling between the structure and magnetism.[82, 133] Planar defects, thus, have been proposed to explain key features in magnetic and transport properties of FeSCs near/below the structural transition. Mazin and Johannes[35] suggested a model in which low-energy magnetic anti-phase (APBs) and 90^o domain (DBs) boundaries proliferate (Fig. 5.1), which have yet to be tested. So, are structural and magnetic planar defects energetically favorable and what are their properties? To answer, we use DFT to model potentially operative magnetic (structural-induced) defects, both isolated and extended, and explore their stability and properties by varying the structural parameters.

5.1 Controversy on Magnetism

Defects can be very important in realistic materials, like $BaFe_2As_2$. Above T_N, the paramagnetic state may be realized by mobile APBs and DBs; below T_N, with interlayer coherence, APBs become pinned and DBs thermodynamically inaccessible, possibly explaining sensitivity to interlayer elements, large magneto-resistance, features in the differential resistivity ($d\rho/dT$), and invariance of resistivity anisotropy. With orthorhombic distortions ($a > b$), both structural and concomitant magnetic twins (Fig. 5.2) are observed in $BaFe_2As_2$ along $\langle 110 \rangle$ with 100-400 nm[204] up to 10-50 μm[42] between boundaries. With stress, samples detwin, but twins return upon its removal;[205] as in $YBa_2Cu_3O_{7-\delta}$,[206] $(1\bar{1}0)$ twins terminate on (110) twins. Twins cause anisotropic scattering near AFM wavevectors, giving 2-dimensional spin fluctuations. Twins also create stripes of increased diamagnetic response,[207] and nucleate SC at their boundaries.[43] Recently, Niedziela et al.[208] found by Rietveld analysis a bigger orthorhombic ratio (O $=(a-b)/(a+b)$) for local structural fits (O = 1.38%) than global fits (O = 0.78%); they proposed a high density of *nano*-twins (Fig. 5.2) account for this discrepancy by its better match to measured pair distribution functions (PDF). We show that displacements at the *nano*-twin boundary affect spin alignment, reducing the average "ordered" moment.

For completeness, we note that, while DFT supports the observed SDW for the parent compound, the Fe moment ($1.6-1.9\ \mu_B$)[209, 31] is twice that assessed for the average ordered moment from neutron diffraction ($0.8-1.04\ \mu_B$).[95, 210, 93] In fact, various experiments assess very different Fe moments. Core-electron spectroscopy[153] finds 2.1 μ_B, like DFT, while ^{57}Fe Mössbauer[40] and nuclear magnetic resonance[211] find 0.81 μ_B, as in diffraction assessments. For Fe-based magnets such a large discrepancy between ordered moments from theory and experiment is unusual. Spin-orbit and hybridization (controlled by Fe/As planar spacing) in a DFT+U model explained the small in-plane moments in Fe-pnictides.[72] Yet, our DFT moments are reduced ∼10% from spin-orbit, but 50-100% by slightly reduced Fe-As spacing. DFT predicts correct moments at short times ($\sim 10^{-15}$ s) necessary to yield lattice constants that agree with experiment.[35] Dynamical mean field theory (DMFT) explains the discrepancy from DFT as a result of dynamical fluctuations at the Fe sites that reduce the observed moment over longer time scales ($\sim 10^{-9}$ s),[79] and reproduces the trends in reduced Fe moments and renormalized mass across various FeSCs.[98] DMFT finds FeSCs are correlated due to intra-atomic exchange from Hund's coupling J (0.3 - 0.6 eV)[212, 213, 214, 215] (which reduces the coherence temperature for Fermi liquid behavior[214]), not from especially large U (2.8 - 5.2 eV, as derived from a five band constrained Random Phase Approximation)[213, 215, 216, 217] or proximity to a Mott insulating state. Below the coherence temperature, high electron mobility results in moment screening (over $10^{-9}s$). Notably, this scenario does not consider spatial fluctuations, defects, nor their effect

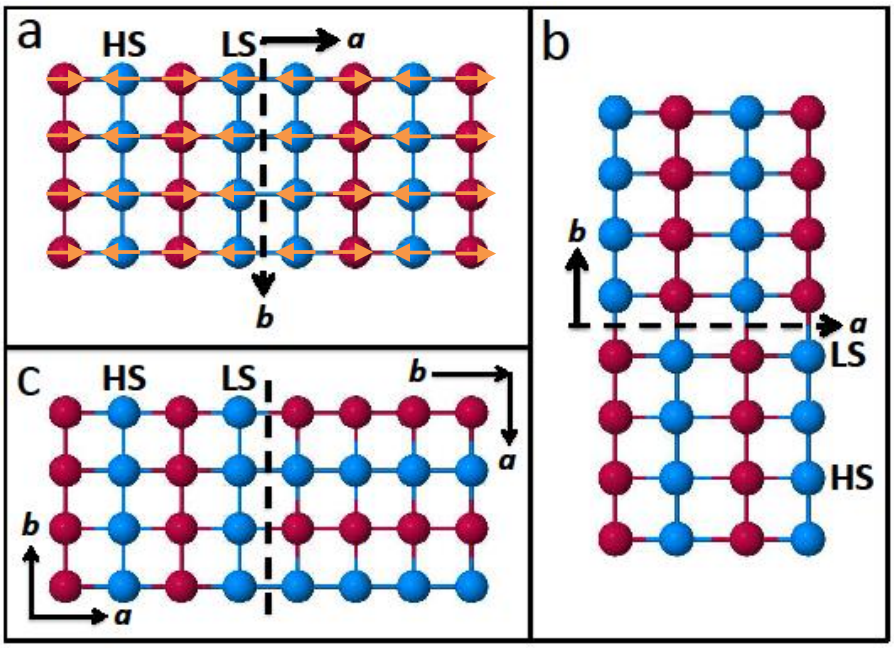

Figure 5.1: (Color online) APB in the (a) *bc*-, (b) *ac*- planes, and (c) 90^o DB with no strain (a=b). Red (blue) circles are "up" ("down") in-plane moments, as indicated in (a). HS, MS and LS indicate Fe-sites with high-, medium- and low-spin states.

on magnetism near/below the phase transition, as explored in the present work.

5.2 Methods: Defects and DFT

We use DFT to simulate various magnetic planar defects, *i.e.*, two types of APBs, a 90^o DB, twin boundaries, and our modified *nano*-twin, which are all low-energy excitations of the SDW. Figure 5.1a and 5.1b shows two APB boundaries in the Fe-plane – parallel to the *bc*- or *ac*-planes – and Fig. 5.1c shows a locally unstrained 90^o DB. Figure 5.2a shows a typical example of an ideal twin. A modified *nano*twin with 2-dimensional structural distortion (consistent with that suggested by Niedziela *et al.*[208]) is shown in Fig. 5.2b with a series of static displacements along a- and b-axis in the supercell. The undisplaced nanotwin with 1-layer of Fe separating defect planes is really a magnetic stacking fault (SF); a nanotwin supercell has very different boundary conditions than a twin, with different far neighbors and distances between defect pairs; indeed, "ideal twin" supercells formed with 1-layer separation between defect planes (a high density of SFs) has local environments like the nanotwin, except that twin has symmetric relaxations governed by the supercell periodicity, whereas the nanotwin has asymmetric, localized distortions to match the PDF. While we show the defect energies are similar, a nanotwin, due to its boundary condition and supercell, may be considered

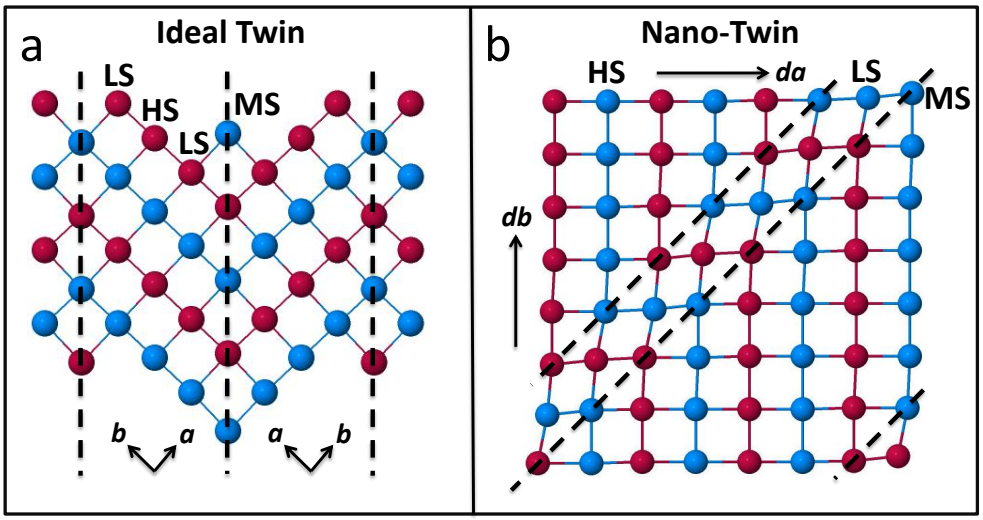

Figure 5.2: (Color online) (a) Twin boundary, without strain, separated by three Fe layers. (b) Nanotwin with boundary $\perp$ to (110), where atom positions in a distorted cell are barycentric weights of the cell corners. HS, MS and LS are indicated.

a fluctuating twin nuclei, which can have low-spin Fe-sites unavailable in the ideal twin supercell.

For nondefected (parent) and defected cells we calculate energy per atom and the associated magnetic moments (bulk is 1.6 μ_B). From this we derive the planar defect energy, γ, defined as $\gamma = (E_{\rm def} - E_0)d/V$, where $E_{\rm def}$ and E_0 are the total *energy per atom* of the defected and nondefected cell, respectively. d is the distance between defect planes and V is the volume per atom. While the energy per atom is helpful, γ is the appropriate comparison for cost of creating the defect interface and its dependence on defect density and defect volume. Note that 2 defect boundaries are created for twins, hence, 2γ is appropriate defect energy.

To do this, we use VASP[218] with plane-wave pseudopotential projected augmented wave (PAW) basis,[219] with an energy cut-off of 380–420 eV. A Monkhorst-pack Brillouin zone integration with a 16^3 **k**-mesh is used for the SDW ($Fmmm$) structure. Smaller **k**-meshes are used for supercells depending on the length coverage along each axis.

For APBs, we constructed doubled (2×1×1), quadrupled, and octupled supercells to examine excitations, denoted by 2-APB, 4-APB and 8-APB, respectively (Fig. 5.3). For APBs (Figs. 5.1a,b), we use measured lattice parameters[40] (a=5.6146, b=5.5742 and c=12.9453 Å). For a 90^o DB, we set $\bar{a} = \bar{b} = (a + b)/2$ = 5.5944 Å to reduce local strain effects, and construct supercells similar to the APBs, denoted as 2-DB, 4-DB, and 8-DB. Twin ($4[1 + n]$×2×1) supercells (n=0, 1, ...) are denoted by $(3 + 4n)$-N Fe-layers between defect planes, and have $4(1 + n)$ unit cells along a and $8(1 + n)$×10 atoms/cell. Nanotwin supercells are denoted 3-N, 5-N, 9-N, and 13-N for Fe-layers between isolated nanotwin pairs; the supercells with the static displacements suggested by Niedziela *et al.* are more complex because the local distortions must be

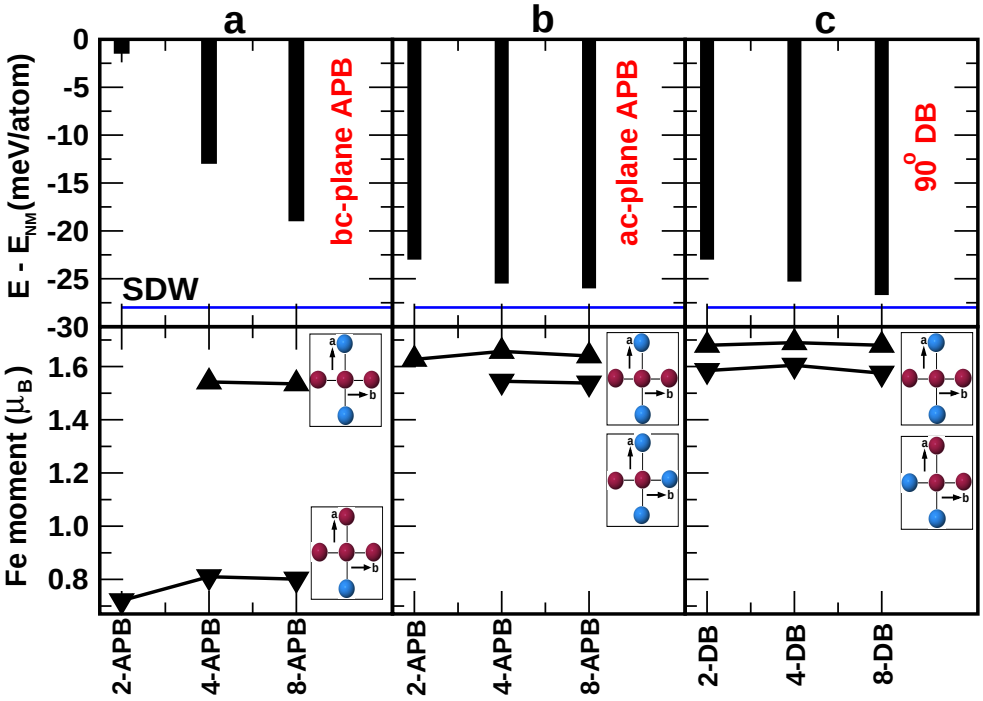

Figure 5.3: (Color online) Energies relative to NM state (top) and Fe moments (bottom) for APBs (labels defined in text) in the (a) *bc*-plane (b) *ac*-plane, and (c) 90^o DB. SDW indicates the AFM ground state. Insets depict the local Fe environment.

compensated within the cell (Fig. 5.2b).

5.3 Energetics and Moments

The energies and moments for APB and DB defects relative to the non-magnetic (NM) state are shown in Fig. 5.3 (top), and compared to the AFM ground state (SDW). In all cases, Fe moments have two behaviors: a high-spin state (HS in Fig. 5.1) at sites away from boundaries and a low-spin state (LS in Fig. 5.1) at/near boundaries. For APB(bc), the LS moment falls substantially to 0.8 μ_B from 1.6 μ_B, similar to that found by Yin *et al.*[220] While for APB(ac), the LS moment decreases only to 1.54 μ_B. The two spin states depend on local magnetic environments (inset Fig. 5.3). Moments do not vary much with the size of the supercells, but these two structures energetically compete with the ground state SDW ($\leq$ 9 meV/atom). For 90^o DB (Fig. 5.1c), the HS state has a higher moment of 1.7 μ_B due to global strain from changed lattice parameters. The LS moment decreases slightly to 1.57 μ_B near the boundary. This defect requires within 2 meV/atom excess energy to form compared to the SDW. It is energetically competing with the APB(ac). Both defects are then expected to be present at the same temperature. The local environment does not play a significant role, suggesting simple models such as counting the number of aligned neighbors

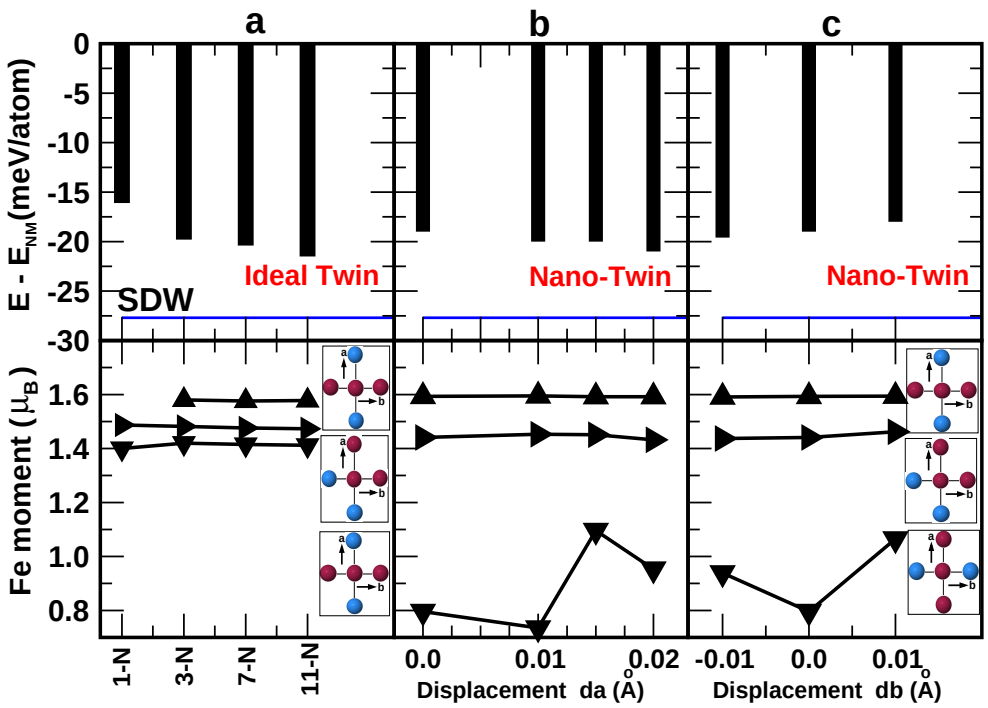

Figure 5.4: (Color online) Same as Fig. 5.3 but for (a) twins (labels defined in text), and nanotwins (3×3×2 supercell) with displacements along (b) da and (c) db axes. Fe has HS, MS, and LS states due to local environment (insets).

is not sufficient to characterize the moments.

The energy and moments for twins are shown in Fig. 5.4a. Interestingly, an Fe-atom in a twin has three spin states depending on the local environment. Fe-atoms at the boundary remain in a medium-spin state (MS in Fig. 5.2a). A LS state occurs on Fe-sites adjacent to the boundary (Fig. 5.2a). These Fe-sites have the same nearest-neighbor environment as the bulk HS states but differ in the farther neighbors. These defects can form at a few meV/atom, albeit γ is more critical, see below.

The nanotwin energies and moments versus distortion along $a-$ and $b-$axis (in Å) are shown in Fig. 5.4(b,c). Similar to twins, there are three Fe spin states: a HS bulk (1.6 μ_B), a MS (1.42 μ_B) at the boundary, and a LS ($0.8 - 1.0$ μ_B) in the vicinity of the distorted side of the boundary. The structural perturbations show a stronger effect on the LS moments near defect boundaries, decreasing to as low as 0.8 μ_B. Isolated (fluctuating) nanotwins are equally competitive to form as dense twins but with much reduced moments. Energies are affected mostly by the changed magnetic configurations and very little by spatial distortions. So, magnetic defects drive the short-range structural distortion (not the other way around) and can help quench magnetization.

Planar defect energies (γ or $2\gamma_{twins}$) are compared in Table 5.3; they give the relative *order in which magnetic defects can form and remain after processing.* Structural defects can act as pinning sites for magnetic

Table 5.1: γ (2γ for twins) for various planar defects (in $m\mathrm{J/m}^2$). Energies (meV/atom) are relative to SDW. γ_{twin} is dominated by d increasing faster than the decrease in $(E_{\mathrm{def}} - E_0)$, unlike for APBs or DBs.

defect type	supercell	energy	$(2)\gamma$
	2-APB	26.5	118
APB (*bc*-plane)	4-APB	15.0	133
	8-APB	9.0	160
	2-APB	5.0	22
APB (*ac*-plane)	4-APB	2.5	22
	8-APB	2.0	35
	2-DB	5.0	22
90^o DB	4-DB	2.7	24
	8-DB	1.3	22
"twin" (ideal)	0-N	18.3	57
"twin" (relaxed)	1-N	9.9	62
"twin" (ideal)	1-N	11.9	74
	3-N	8.2	102
	7-N	6.6	165
twin (ideal)	11-N	6.1	228
	15-N	5.0	(max) 252
	19-N	3.7	231
	23-N	3.0	222
	27-N	2.4	210
	3-N	9.2	86
nanotwin	5-N	6.4	80
(undistorted)	9-N	4.1	77
	13-N	2.5	63
NM bulk	10 atom	28.0	n/a

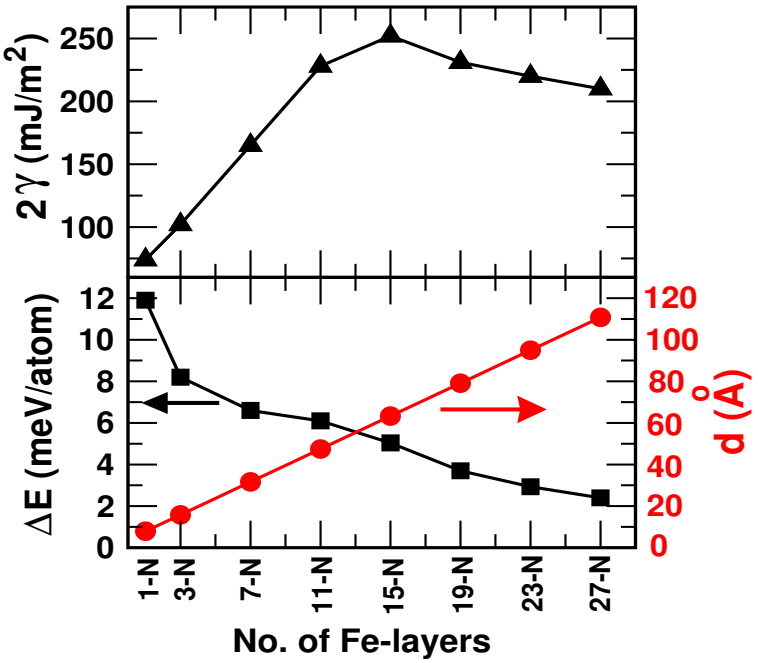

Figure 5.5: Figure 5. (Color online) Twin energy 2γ (top) and $\Delta E = (E_{def}\text{-}E_0)$ and "d" (bottom) versus number of Fe-layers.

domain walls. Energetically, APB(ac), 90^o DB and nanotwins (low-energy spin excitations) are the most favorable and most likely to persist after annealing. Interestingly, densely-pack twins of a single tetragonal variant are also remarkable very low energy. These nanoscale defects compete with widely separated twins (spin kinks), which are observed. Such small fluctuating defects will affect the observed average moments, whereas separated twins will affect the magnetic correlation length, see below. Separated twins do form and are stabilized by lattice strain arising from disclinations formed when twins oriented 90^o apart (from the two tetragonal variants) intersect.[206] It is the twin-twin interactions that stabilize the mesoscale twins.

Typically in metals, the calculated $2\gamma_{\text{twin}}$ is monotonically decreasing versus d (the separation of the twin boundaries) until it plateaus at the measured twin boundary energy; essentially, the defects interact (costing energy) until separated enough that they are screened from one another. Strikingly in $BaFe_2As_2$, separated twins are higher in energy than dense twins, until a d of 16 unit cells (15 Fe-layers), where $2\gamma_{\text{twin}}$ reaches a maximum (Table 5.3 and Fig. 5.5), after which there is a slow convergence of $2\gamma_{\text{twin}}$ versus d (Fig. 5.5). At 28 unit cells ($\sim$11 nm), $2\gamma_{\text{twin}}$ has not yet converged, emphasizing the long-range interactions among twins. Observed structural twins[42, 204] are extended well beyond the ones computationally feasible. Thus, higher-density twins should become prominent near the phase transition, where they compete with the ground state.

5.4 Twin separation

Twin separation d is also affected by stress. Equilibrium is typically reached when the applied stress is $\sim 2\gamma_{\rm twin}d$, which is, however, exceedingly small for isolated twins in $BaFe_2As_2$. In real samples twins appear in 90^o oriented pairs, where $(1\bar{1}0)$ twins terminate on (110) twins; this configuration is stabilized by lattice strain arising from disclinations,[206] where the strain is reduced at the cost of increased d. With stress (estimated roughly from a set of disclinations,[206] and orders of magnitude larger than $2\gamma_{\rm twin}d$), samples detwin, but twins would (and do) return upon its removal.[205]

Twins cause anisotropic scattering near AFM wavevectors, giving 2-dimensional spin fluctuations, and create stripes of increased diamagnetic response.[207] While twin separation depends on local defects and stress, it is expected to get a peak in the magnetic susceptibility $\chi(q)$ at $q = 2\pi/\hat{\rm d}$, where $\hat{\rm d}$ is the average twin-twin separation where 2γ saturates. The direction of q is perpendicular to twin boundaries (i.e., 45^o to reciprocal-space k_x- and k_y-axes, where x (y) is along a- (b-) axis). While the twins dictate the magnetic correlation length, we suggest that small, low-energy excitation can further depress average moments by spatial and temporal averaging, beyond those due to dynamic fluctuations.

Nanotwins (Fig. 5.2b) with no local distortion are like an isolated, ideal defect pair, not a dense set of twins. To understand the effect of short-ranged structural distortion, we have studied a 1-N ideal twin with(out) relaxation in ab-plane for only those atoms near the boundary, more localized than in the nanotwin supercell. The planar defect energy with(out) relaxation is 62 (74) $m{\rm J/m}^2$. Relaxations along a- and b-axis lie within 0.9% of ideal, close to the best fit to measured PDF,[208] so the twin and nanotwin are very similar in energy and local structure. Unlike for ideal twins, the nanotwin surface energy decreases to its limiting value as the nanotwin-nanotwin distance grows (Table 5.3), and it is much lower in energy than extended twins. Thus, a nanotwin may be considered a fluctuating twin nuclei, which has many more LS sites (Fig. 5.4) not available in a twin supercell, with moments as low as 0.8 μ_B near the defect, similarly to the assessed values in $BaFe_2As_2$. Our calculations support Niedziela et al.'s suggestion[208] that nanotwins constitute an important fluctuating excitation in $BaFe_2As_2$.

Because the local magnetic configurations play the key role in determining the spin states of Fe, we calculated the site- and l-projected density of states (DOS) to understand the electronic-structure origin. Figure 5.6 shows the Fe d-projected DOS for HS and LS states. For the bulk (HS) states, the major contribution at Fermi energy E_F arises from Fe d_{xz} and $d_{3z^2\text{-}r^2}$, also evidenced from ARPES.[221] All the other orbital components exhibit a pseudo-gap near E_F. For LS-Fe compared to HS-Fe, all the projected DOS are shifted towards E_F. The most pronounced effect occurs for d_{xz} and $d_{3z^2\text{-}r^2}$ character, where majority states for LS fall into a pseudogap for d_{xz} but are peaked for $d_{3z^2\text{-}r^2}$. Although the change of these orbital

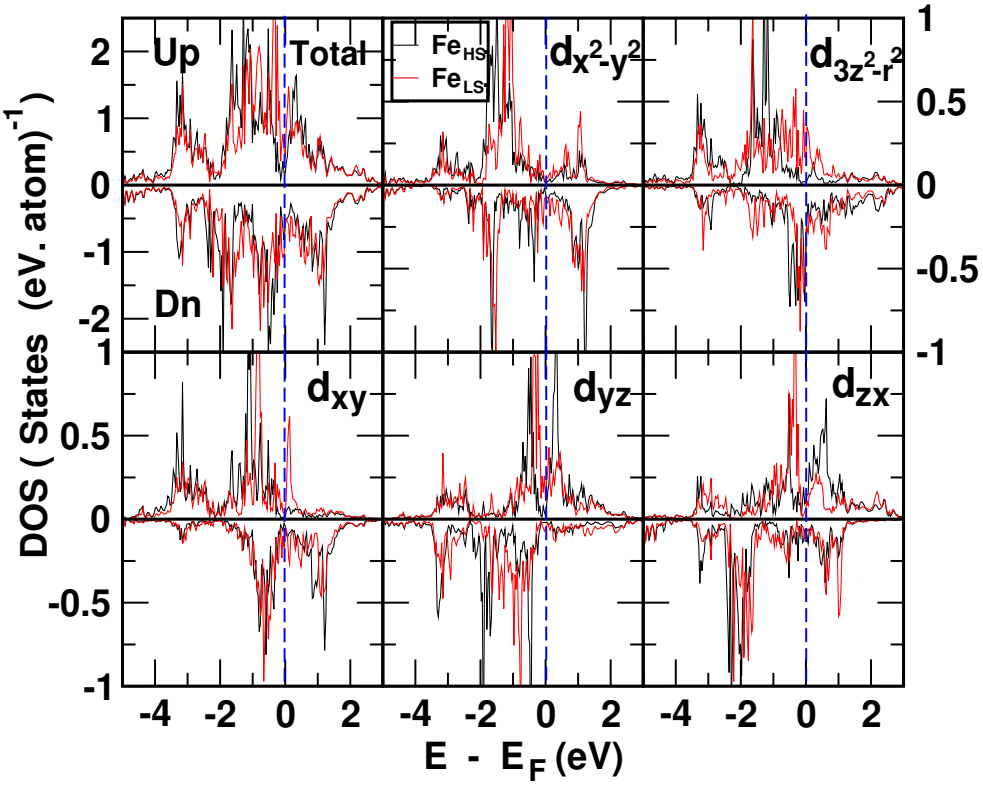

Figure 5.6: (Color online) d-orbital and spin-projected DOS of an undistorted nanotwin on HS (black, heavy line) and LS (red, light line) Fe-sites, with majority (minority) DOS plotted on positive (negative) vertical axis. Fermi energy is indicated by vertical dashed line. x, y, and z directions correspond to a, b, and c respectively.

states is dominated by in-plane Fe-spin configurations, small contributions also arise from the hybridization with As p_x and p_y orbitals (out of the Fe-plane), eventually altering the FS. The large difference in the near E_F (majority) DOS between the HS and LS state points to the orbital dependent electronic origin for quenched moments.

In summary, we studied competing low-energy, magnetic planar defects in $BaFe_2As_2$. The favorable defects are APB(ac), 90^oDB, and nanotwins, but twins (which are observed) are favorable through the mesoscale. The most pronounced reductions in Fe-moment are near the boundaries of APBs(bc) and nanotwins. We find that isolated closely-spaced twins (twin nuclei) are energetically favorable and correspond to a recently proposed nanotwin suggested to match the pair distribution function from scattering experiment.[208] Nanotwins are energetically insensitive to microscopic displacements near the boundary, in contrast to sensitivity to the As z coordinate. APBs along bc-planes and ac-planes are not equally favorable, an anisotropy not anticipated in the Mazin and Johannes model.[35] These defects can reduce the Fe moment from spatial averaging, an environmental dependence which is not included in DMFT.[79, 98] Assessing these defects and their dynamics can affect magnetism, which can be evaluated via Monte Carlo simulations, and which are planned.

Chapter 6

Conclusion

6.1 Summary

In this thesis we addressed issues regarding the Fe-based superconductors, in particular the effects of chemical and magnetic disorder, as well as spin excitations and magnetic planar defects that proliferate at low temperature. We detailed alloying for electron- and hole-doped variants of $BaFe_2As_2$.

On the electron-doped side we found the limitations of the rigid-band model, which is frequently and incorrectly applied in the literature. Furthermore, even when the Fermi-surface nesting does evolve according to rigid-band concepts, there is significant broadening of states due to magnetic and/or chemical disorder, reducing the magnetic susceptibility and thus instability to AFM ordering. This instability is critical; as it becomes less pronounced, spin fluctuations increase and superconductivity is turned on. We found the origin for these differences in the electronic structure (generalized dispersion) and in the site-projected density of states of different transition-metal dopants. Those metals whose valence states have strong overlap in energy with Fe (e.g., Co,Ni) follow a rigid-band model closely, while those that due not (e.g., Cu,Zn) show deviating trends in their formation energetics. Physically, the large energy difference of Fe and Cu,Zn valence states (due to increasing atomic number and shift of valence levels) leads to large impurity scattering and reduced favorability to mixing. These results agree with measurements of the spin-density wave incommensurability and ARPES on carrier densities with doping [85, 140].

On the hole-doped side, a topological transition occurs near the Brillouin zone X point for high concentrations. Here, the two electron cylinders "dissolve" and become four hole-like, lobe-shaped cylinders, symmetrically positioned about X. This transition has been tied to a change in the SC gap symmetry; and, therefore, the stable SC phase. The $s-$ and $d-$ wave SC symmetries are competitive in this regime, suggesting the presence of a quantum critical point. There has been experimental controversy in characterizing where this transition occurs. Experiments have been limited by the number and quality of samples, and by the limitations of ARPES as a surface probe. Here we find the transition occurs at 90% K content. We also see that, despite the involved nature of the transition, the orbital character remains unchanged

throughout the transition. The change in SC state associated with the disappearance of electron cylinders strongly suggests the importance of interband transitions in creating $s^{\pm}$ Cooper pairs from spin fluctuations. We were also able to address issues associated with sample quality on the K-rich side, where the transition occurs. By outlining the complete free energy of the $Ba_{1-x}K_xFe_2As_2$ compounds we explained why there is an observed tendency to optimal doping at x near 0.4 and chemical instabilities near 0.7.

We then looked at spin excitations and planar magnetic defects in $BaFe_2As_2$. In $BaFe_2As_2$, twins are observed to proliferate below the Néel transition. Furthermore, spin fluctuations are observed well above the nematic phase boundary. Superconductivity was even found enhanced near the the twin boundaries. Rapid spin fluctuations, along with electronic correlations, are considered responsible for a reduction of magnetic moments. We found many of these excitations are indeed low energy, corroborating their presence at temperatures above the Néel transition. We also find a peak in the energetics for twins separated by fifteen or more Fe layers, in approximate correspondence with the observed magnetic correlation length. Lastly, we detailed the properties of twin fluctuating nuclei, i.e. nanotwins, which are very low-energy excitations that explain the details of the pair distribution function measured in neutron diffraction [208].

6.2 Future Directions

To improve our understanding of the Fermi-surface driven nesting, it would be a priority to develop code that performs susceptibility calculations within a linear response approximation. Direct calculation of susceptibility for all wave-vectors, indicating where peaks exist for unstable ordering modes and determination of how and why commensurate to incommensurate transitions occur. Further code development, such as relaxations on atomic locations, would enabled improved, automated calculations for the magneto-structural coupling in these compounds. As we found, Cu,Zn-doped samples are unfavorable to mixing. Thus inclusion of short-range ordering effects via the dynamical cluster approximation [151] would be an even better description of these compounds than the CPA. Modest correlations in these compounds could be captured by a quantum Monte Carlo and DFT hybrid approach. This would share some similarities with dynamical mean-field theory codes, but also differences that would allow for a different perspective and opportunity for further comparison.

An obvious continuation of these calculations is to explore electron- and hole-doping in the 1111 compounds, which are the other major class of Fe-SC. It would be interesting to see which of our results continue to hold true in that case; and, if not, what are the differences. For example, I expect rigid-band approximations and stearic effects to hold better for rare-earth substituted 1111 samples because substitutions are

not in the active layers. However, for hole doping, we should also expect to see a transition in the electron pockets and similar change in SC phase. One of the differences in these compounds is that they are more correlated than the 122, with further depressed moments. That makes them more difficult to study by direct DFT calculations, but also makes spin-wave and defect calculations even more relevant.

Going forward there has been recent interest at Ames laboratory by M. Tanatar and R. Prozorov in calculating the resistive anisotropy on the K-rich side of $Ba_{1-x}K_xFe_2As_2$. Experiments observe peaks in thermodynamic quantities (e.g., thermal expansion coefficient) as a function of temperature in pure KFe_2As_2. While there are no such peaks in the in-plane resistivity, which is most commonly measured, recently there have been found to be peaks in the resistivity as measured along the c-axis. It has been suggested this is tied to the warping on the hole bands at the K-rich end. Therefore, it is of interest to perform calculations of the out-of-plane resistivity for K-rich compounds using the calculated band structure and Fermi velocities. To do this, transport expressions with chemical disorder can be derived in KKR-CPA, e.g. Kubo-Greenwood formalism, will need to be implemented in the code. In addition, there needs to be a means to adjust our bands (e.g., LDA+U) to quantitatively match quantum oscillation and ARPES experiments. These together will then allow a means for a realistic calculation of the transport properties, to confirm the source of resistive anomalies, and thus to show what electron ordering is driving these transitions.

Appendix A

Superconductivity

A.1 Phenomena of Superconductivity

Superconductivity was discovered in 1911 by Kamerlingh Onnes on cooling solid Hg. He was investigating the electrical properties of metals at low temperatures. While it was expected the resistance would diminish, it was thought it would happen gradually, and then only for pure specimens. Instead, at 4.2 K, there was a sudden drop in resistance to zero. This is characteristic of a phase transition. Superconductivity is a thermodynamically distinct state featuring two major properties. The first is *perfect conductance*. It has been shown whatever resistance exists must be at least 10^{-18} times smaller than for ordinary copper at room temperature. An important consequance of this is that the total flux threading a closed superconducting circuit cannot change. The second, identified 22 years later, is the "Ochsenfeld-Meissner" (or simply Meissner) effect. This is perfect diamagnetism, or the *complete expulsion of magnetic fields* from the interior. In ordinary metals an applied magnetic field will totally permeate the sample after some transitory period. A consequance of the Meissner effect is that all SC currents must flow near the surface of the sample. This is in analogy to charge scattering to the surface in an ordinary metal. Superconductivity is not a rare phenonmenon. Many elemental metals will SC at sufficiently low temperatures ($T_c \sim$ 0-10 K).

The SC state can be destroyed by application of a large magnetic field (H_{c1}) or current density (J_c), both of which are temperature dependent. In fact the latter implies the former since the Meissner effect is sustained by surface currents. The behavior of SCs in the presence of magnetic fields subdivides them into two categories, labeled Type I and Type II. Both types exhibit a sudden expulsion of interior fields below H_{c1}. However, in Type II SCs, an inhomogenous state can occur for fields satisfying $H_{c1} < H < H_{c2}$. In this regime a regular lattice of microscopic vortices of "normal" regions enclosing quantized flux penetrates. The T_c, H_c, and J_c values, and their anisotropies, give a macroscopic characterization of a SC. Improving these traits is one key to technological applications. There are also *micro*scopic characterizations of a SC. One is the penetration depth of a magnetic field near the surface of a SC, which falls off exponentially. The penetration depth is temperature dependent and typically one refers to the zero temperature quantity.

Another length scale is coherence length of a SC, in other words the response distance of a SC in the presence of an external perturbation, such as an impurity. Whether a SC has Type II behaviour depends on the relative size of the penetration depth and coherence length. All high-T_c SCs are Type II.

Superconductors find use in MRI, NMR, magnetometers (SQUID), particle accelerators, maglev trains, and sensitive electronics. Given the serendipitous discovery of most SCs to date, it is almost certain there are undiscovered SCs with improved properties that will further benefit existing applications and find new domains of use.

A.2 Electrodynamics

The phenomenology of SCs can be used to understand electrodynamics in the presence of a SC, especially making connections to the penetration depth and coherence length. Brothers F. London and H. London (1935) were the first to do this. They ascribed SC to a fluid of "superelectrons" (later identified as Cooper pairs) that experience no drag. By Newton's law, the rate of change of superfluid current is $\dot{\mathbf{J}}_s = (n_s q^2/m^*)\mathbf{E}$. *This is in contrast to Drude-Lorentz equation for a metal*, which contains a mean-free time τ to scattering. Insertion into Maxwells equations followed by straightforward manipulations gives

$$\nabla \times (\nabla \times \frac{\partial}{\partial t}\mathbf{H}) + (\frac{1}{\lambda_L^2} + \frac{\epsilon}{c^2}\frac{\partial^2}{\partial t^2})\frac{\partial}{\partial t}\mathbf{H} = 0, \tag{A.1}$$

where $\lambda_L = (4\pi n q^2/m^* c^2)$ is the London penetration depth. To incorporate the Meissner effect, the London brothers integrated (A.1) and *set the integration factor to zero.* For time-invariant fields the London equation is then

$$\nabla \times (\nabla \times \mathbf{H}) + \frac{1}{\lambda_L^2}\mathbf{H} = 0. \tag{A.2}$$

A consequance of their equation is that magnetic fields fall off as $\mathbf{H}(z) = \hat{\mathbf{x}} H_x(0) e^{-z/\lambda_L}$ near the surface of a SC. When stated in the London gauge (i.e. $H = \nabla \times A, \nabla \cdot A = 0$)) it becomes $\mathbf{J}_s = -(nq^2/m^* c)\mathbf{A}$. Later, Pippard generalized this relation to a non-local one

$$\mathbf{J}_s = -\frac{nq^2}{m^* c}\frac{3}{4\pi\xi_0}\int \frac{\mathbf{A}(\mathbf{r})\mathbf{r}}{r^4} e^{-r/\xi_0} d\mathbf{r} \tag{A.3}$$

by introducing an empirical coherence length ξ_0. Pippard's description becomes relevant when $\lambda_L \ll \xi_0$.

An alternative phenomenological approach was developed by V. Ginzburg and L. Landau (1950). They reasoned that SC was a macroscopic quantum state. This meant one could ascribe a relative phase difference between macroscopic points in a superconducting body. Further, an amplitude could be assigned at each

point proportional to the number of superelectrons. Thus they introduced a complex order parameter $\psi(\mathbf{r})$ to describe an inhomogenous SC state. This order parameter was used in an expansion for the free energy according to the Landau theory of phase transitions. In other words

$$f_s(T,\psi) = f_N(T) + \alpha(T)|\psi|^2 + \frac{1}{2}\beta(T)|\psi|^4 + \frac{1}{2m^*}|(\mathbf{p} - \frac{q}{c}\mathbf{A})\psi(\mathbf{r})|^2, \tag{A.4}$$

where $\alpha(T)$, $\beta(T)$ are phenomological coefficients and $f_N(T)$ is the free energy density of the normal state. In analogy with the quantum mechanics of a charged particle, the third term is a minimal coupling to the electromagnetic field. When the free-energy is minimized with respect to variations of the order parameter $\psi(\mathbf{r})$ and vector potential $\mathbf{A}(\mathbf{r})$, it yields constraints on $\psi(\mathbf{r})$ and $\mathbf{J_s}(\mathbf{r})$:

$$\frac{1}{2m^*}(\mathbf{p} - \frac{q}{c}\mathbf{A})^2\psi(\mathbf{r}) + \beta|\psi(\mathbf{r})|^2\psi(\mathbf{r}) = -\alpha(T)\psi(\mathbf{r}) \tag{A.5}$$

$$\mathbf{J_s}(\mathbf{r}) = |\psi(\mathbf{r})|^2\left[\frac{q\hbar}{m^*}\nabla\theta(\mathbf{r}) - \frac{q^2}{m^*c}\mathbf{A}(\mathbf{r})\right], \tag{A.6}$$

where $\theta(\mathbf{r})$ is the phase of $\psi(\mathbf{r})$. The Ginzburg-Landau theory can be used to derive its own penetration depth and coherence length,

$$\lambda_{\text{eff}}^2 = \frac{m^*c^2\beta}{4\pi q^2|\alpha(T)|} \quad \text{and} \quad \xi_{\text{GL}}^2(T) = \frac{\hbar^2}{2m^*|\alpha(T)|}. \tag{A.7}$$

Both λ_{eff} and ξ_{GL} diverge $(T_c - T)^{-1/2}$ for $T < T_c$. The theory has been successful in describing the effects of inhomogeneities on a SC, flux quantization, and the Josephson effect.

A.3 Thermodynamics

Superconductivity is a thermodynamic state completely characterized by the temperature T and applied field H. As mentioned, sufficiently high fields and temperatures can destroy SC. The critical temperatures and field are often related by the empirical relation $H_c(T) = H_c(0)(1 - T^2/T_c^2)$. At zero field the transition is second-order, with a jump in specific heat but no latent heat. At finite fields the transition is first order. The Meissner effect implies $M = -H$, making it simple to derive the Gibbs free energy density

$$g_s(T,H) - g_s(T,0) = \int (\frac{\partial g}{\partial H})\Big|_{T,p} dH = -\int \mu_0 M dH = \int \mu_0 H dH = \frac{1}{2}\mu_0 H^2. \tag{A.8}$$

At transition, the free energy of the normal state, which is independent of H, and of the superconducting state must equal. Therefore

$$g_n(T) - g_s(T,H) = g_s(T,H_c) - g_s(T,H) = \frac{1}{2}\mu_0(H_c^2 - H^2). \tag{A.9}$$

From these considerations, connections follow to the entropy difference $\Delta s = -\mu_0 H_c\, dH_c/dT$, specific heat jump $\Delta C|_{T_c} = v\, T_c\, \mu_0 (dH_c/dT)^2|_{T_c}$, and latent heat $L = -v\, T\, \mu_0 H_c (dH_c/dT)$ of the normal to superconducting transition, where v is the specific volume. Due to the reduced interaction of superelectrons and the lattice, the thermal conductivity is orders of magnitude smaller in the SC state.

An important feature of SCs is the opening of an energy gap near the electronic Fermi level. There is in fact no observed photoabsorption for frequencies below $\Delta \sim 10^{-3}$ eV. In ordinary metals, the low-temperature electronic specific heat goes as $C_n = \gamma T$, where $\gamma = \frac{\pi^2}{3} D(E_F) k_B^2 T$ and $D(E_F)$ is the density of states at the Fermi level E_F. In a SC $C_s \sim a e^{-b/T}$, which is further evidence of an energy gap. Both are in analogy with the infrared absorption and specific heat of semiconductors. Unlike for semiconductors, this gap does not arise from band structure arguments. Instead, most SCs are metals with a well-defined Fermi surface. As discussed below, the gap plays a central role in the theory of SC.

A.4 Cooper Pairing

Leon Cooper (1957) showed a free electron gas is unstable in the presence of an effective, *attractive* interaction to the formation of bound electron pairs (Cooper pairs). This reasoning is applicable even when the Fermi sea is strongly modified by the presence of a lattice. The band structure might then, for instance, display multiple electron and hole pockets. In this case the starting point is the quasiparticles predicted by band theory. The instability becomes manifest on solving the Schrödinger equation for two quasiparticles in the backdrop of the filled Fermi sea. An unspecified interaction $U_{\mathbf{k},\mathbf{k}'}$ between quasiparticles $\psi_{\mathbf{k}}$ and $\psi_{\mathbf{k}'}$ is posited. $U_{\mathbf{k},\mathbf{k}'}$ may be repulsive at some $\mathbf{k}$ points, but must otherwise be attractive. Whatever the interaction, it will obey the translational and rotational symmetries of the underyling lattice. For conventional SCs, $U_{\mathbf{k},\mathbf{k}'}$ is almost spherically symmetric. For the Cu-SCs and Fe-SCs, the lattice obeys a tetragonal symmetry, therefore $U_{\mathbf{k},\mathbf{k}'}$ will be invariant to symmetry operations under point group C_{4v}. Translational symmetry demands the interaction preserve the total Bloch momentum $\mathbf{k_1} + \mathbf{k_2}$ of the pair. Because $U_{\mathbf{k},\mathbf{k}'}$ does not depend on spin, the orbital and spin degrees of freedom may be separated. The pairs may then be combined as a singlet or triplet. In superfluid ^{3}He the pairs are known to combine as triplets. However, in conventional SCs, and also evidence shows for the Cu-SCs and Fe-SCs, the pairing occurs as a singlet. By combining the bound state so

that the total Bloch momentum is zero the energy of the pair is minimized. If the interaction is nonzero only within a narrow energy range of the Fermi level, as is the case for conventional SCs, then zero momentum pairing also maximizes the number of available scattering states. The singlet pairing is why magnetism can be strongly disruptive to SC. The most general pair singlet can be rewritten as a linear combination $g(\mathbf{k})$ of zero momentum states, that is, with V the volume of the sample

$$\Phi(\mathbf{r_1}\sigma_1, \mathbf{r_2}\sigma_2) = \frac{1}{V}\sum_{\mathbf{k}} g(\mathbf{k}) e^{i\mathbf{k}\cdot(\mathbf{r_1}-\mathbf{r_2})} \chi_{\text{singlet}}(\sigma_1, \sigma_2) \tag{A.10}$$

with the requirements that $g(\mathbf{k}) = g(-\mathbf{k})$ is even and $g(\mathbf{k}) = 0$ for $E_{\mathbf{k}} < E_F$ in order to satisfy antisymmetrization constraints. In this basis the two-particle Schrödinger equation becomes

$$(2E_{\mathbf{k}} - E)g(\mathbf{k}) + \sum_{\mathbf{k}'} U_{\mathbf{k},\mathbf{k}'} g(\mathbf{k}') = 0. \tag{A.11}$$

If there are non-trivial negative energy solutions to this equation, then the *ground-state is unstable* to the formation of bound pairs. Many Cooper pairs will form until a new equilibrium, superconducting state is achieved. The simulatenous filling of many pairs into the same state is possible because the Cooper pair is spin zero and, therefore, a boson. The final ground-state resembles a Bose-Einstein condensate.

The nature of the attractive interaction $U_{\mathbf{k},\mathbf{k}'}$ has been left unspecified. Frölich (1950) first suggested the electron-electron interaction was mediated by polarizations in the ionic lattice. Such a mechanism is possible because the response time of the ionic lattice is much slower than the electrons, allowing for a long-ranged interaction in which the Columb repulsion has been effectively screened. This has proved to be correct for conventional SCs. In USCs it is likely that another mechanism is at work. Berk and Schrieffer (1966) suggested magnetic polarizations might mediate pairing. Kohn and Luttinger suggested so-called Friedel oscillations could lead to an attractive force. Friedel oscillations refer to a screening in which there are shells of both positive and negative charge. This leads to potential wells that another quasiparticle can be attracted to. Other options include excitions and solitons. In ^3He many factors compose the pair interaction, so that no one mechanism plays a starring role. This may also be the case in USCs.

A.5 Pairing Symmetries

In the *average potential approximation*, $U_{\mathbf{k},\mathbf{k}'} = -U_0/N$ is taken as a small, perturbative constant for simplicity and then nonzero only within a narrow shell $\hbar\omega_D$ of the Fermi sea. In that case it can be shown the Cooper pair equation admits a non-trivial solution with binding energy $\Delta_b = 2\hbar\omega_D e^{-2/(U_0 D(E_F))}$. Here

$D(E_F)$ is the density of states (DOS) at the Fermi level. Its presence marks the importance of the Fermi level DOS on SC. The spherical symmetry of $U_{\mathbf{k},\mathbf{k}'} = -U_0/N$ implies $g(\mathbf{k})$ has definite orbital angular momentum ℓ. Singlet pairing requires that $\ell = 0, 2, 4, ...$ be even. In conventional SCs this is always s-wave as it is expected to produce the lowest-energy binding.

Understanding the pairing symmetry is one of the prime pursuits of those studying USCs. For USCs, the interaction $U_{\mathbf{k},\mathbf{k}'}$ has the lower symmetry of the point group G of the crystal. In this case, the solutions $g(\mathbf{k})$ will be proportional to basis functions of one of the irreducible representations of G. In the case of tetragonal Cu-SCs and Fe-SCs, $G = C_{4v}$ and there are five irreducible representations: $A_{1g}, A_{2g}, B_{1g}, B_{2g}$, and E. Each space has an infinite set of eigenfunctions. As A_{1g} is the trivial representation, its basis functions respect all symmetries of C_{4v}. Such solutions are called "s-wave" in analogy with terminology for conventional SCs. Solutions belonging to B_{1g} are "d-wave". It has been shown conclusively that Cooper pairs in Cu-SCs have d-wave pairing. In Fe-SCs there is a strong expectation that the pairing state belongs to A_{1g}, and thus is s-wave, but one which is not the simplest eigenfunction. In other words, there are evidences of sign changes.

A.6 BCS Theory

In 1957 a microscopic theory of superconductivity by Bardeen, Cooper, and Schreiffer (BCS) [222] could explain the properties of many of the known SCs at that time. Indeed, this theory, in its generalized form, is also expected to be applicable to USCs. Building on the success of Cooper, they defined a many-body Hamiltonian taking into account an attractive interaction $U_{\mathbf{k}\mathbf{k}'}$. In second-quantized form it reads

$$H = \sum_{\mathbf{k}} \epsilon_{\mathbf{k}} (c^{\dagger}_{\mathbf{k}\uparrow} c_{\mathbf{k}\uparrow} + c^{\dagger}_{-\mathbf{k}\downarrow} c_{-\mathbf{k}\downarrow}) + \sum_{\mathbf{k},\mathbf{k}'} U_{\mathbf{k}\mathbf{k}'} c^{\dagger}_{\mathbf{k}\uparrow} c^{\dagger}_{-\mathbf{k}\downarrow} c_{-\mathbf{k}'\downarrow} c_{\mathbf{k}'\uparrow}. \tag{A.12}$$

Here $\epsilon_k = E_{\mathbf{k}} - \mu$ is the quasiparticle energy measured relative to the Fermi level and standard notation has been used. It is not possible to solve this Hamiltonian exactly, therefore a mean-field approach must be used. In the original method a variational form

$$|\Psi_S\rangle = \prod_{\mathbf{k}} (u_{\mathbf{k}} + v_{\mathbf{k}} c^{\dagger}_{\mathbf{k}\uparrow} c^{\dagger}_{-\mathbf{k}\downarrow}) |0\rangle. \tag{A.13}$$

is assumed for the ground-state. The variational parameters $u_{\mathbf{k}}$ and $v_{\mathbf{k}}$ satisfy $u^2_{\mathbf{k}} + v^2_{\mathbf{k}} = 1$ and represent the filling of state $|\mathbf{k}, -\mathbf{k}\rangle$ in a singlet. An alternative approach, formulated by Bogoliubov and Valatin [223, 224], is to perform a canonical transformation of the Hamiltonian followed by a mean-field approximation. In either case the resulting solutions are the same.

On minimizing the BCS variational form, the ground-state is given by

$$u_{\mathbf{k}}^2 = \frac{1}{2}\left[1 + \frac{\epsilon_{\mathbf{k}}}{\sqrt{\epsilon_{\mathbf{k}}^2 + \Delta_{\mathbf{k}}^2}}\right] \quad \text{and} \quad v_{\mathbf{k}}^2 = \frac{1}{2}\left[1 - \frac{\epsilon_{\mathbf{k}}}{\sqrt{\epsilon_{\mathbf{k}}^2 + \Delta_{\mathbf{k}}^2}}\right] \tag{A.14}$$

where the "gap parameters" $\Delta_{\mathbf{k}}$ are specified by the self-consistency condition

$$\Delta_{\mathbf{k}} = -\frac{1}{2}\sum_{\mathbf{k}'} U_{\mathbf{k}\mathbf{k}'} \frac{\Delta_{\mathbf{k}'}}{\sqrt{\epsilon_{\mathbf{k}'}^2 + \Delta_{\mathbf{k}'}^2}}. \tag{A.15}$$

The gap parameters $\Delta_{\mathbf{k}}$ are central to the theory of SC. The opening of an energy gap is tied with the magnitude of $\Delta_{\mathbf{k}}$. Note, however, that $\Delta_{\mathbf{k}}$ is a complex quantity. As in the Cooper pairing problem, the symmetry of $U_{\mathbf{k}\mathbf{k}'}$ dictates $\Delta_{\mathbf{k}}$ be a basis function of an irreducible representation of the point group G of the underlying lattice. The gap parameters can be taken as the order parameter associated with the SC transition, however it is more common to choose $\psi_k = \langle\Psi_S|c_{-\mathbf{k}\downarrow}c_{\mathbf{k}\uparrow}|\Psi_S\rangle$. At finite temperatures the self-consistency condition includes a factor of $\tanh(\frac{1}{2T}\sqrt{\epsilon_{\mathbf{k}'}^2 + \Delta_{\mathbf{k}'}^2})$ on the right-hand side of (A.15). Experimental characterization of the gap reveals facets of the space-time structure of the $U_{\mathbf{k}\mathbf{k}'}$ interaction.

A.7 Conventional Superconductors

Before the advent of high-T_c SCs, most SCs shared a phenomenon known as the isotope effect. Substituting atoms for an isotopic variant had a direct and inverse relation on T_c and H_c. This inspired the suggestion that the ionic lattice had a strong role to play in the attractive coupling $U_{\mathbf{k}\mathbf{k}'}$. Formally, the phonon mediated electron-electron interaction can be written in perturbation theory as

$$U_{\mathbf{k}\mathbf{k}'} = \frac{1}{2}\sum_{\mathbf{q}} |M_{\mathbf{q}}|^2 \left[\frac{1}{E_{\mathbf{k}} - E_{\mathbf{k}-\mathbf{q}} - \hbar\omega_{\mathbf{q}}} + \frac{1}{E_{\mathbf{k}'+\mathbf{q}} - E_{\mathbf{k}'} - \hbar\omega_{\mathbf{q}}}\right], \tag{A.16}$$

where $M_{\mathbf{q}}$ is the strength of coupling to phonon mode $\mathbf{q}$. As the phonon energies are smaller than energies near the Fermi level, the largest contribution will be near $E_{\mathbf{k}} = E_{\mathbf{k}-\mathbf{q}}$, for which $U_{\mathbf{k}\mathbf{k}'} < 0$. Also note $\mathbf{k}$ and $\mathbf{k}'$ appear in separate terms. If the Fermi sea is spherically symmetric, as for a free electron gas or simple metal, then we can justify the average potential approximation $U_{\mathbf{k}\mathbf{k}'} = -U_0/N$ within $\hbar\omega_D$ of the Fermi level.

Working out the consequances of this choice describe the behavior of conventional SCs. Cooper pairs are

connected as a s-wave singlets. The connection between the gap and critical values are

$$\Delta(T) = 3.06 k_B T_c \left(1 - \frac{T}{T_c}\right)^{1/2} \quad \text{and} \quad H_c^2 = 4\pi D(E_F)\Delta(0)^2 \frac{1}{V} \tag{A.17}$$

and the jump in specific heat is

$$\Delta C(T_c) = 4.68 D(E_F) k_B^2 T_c. \tag{A.18}$$

These predictions are in good agreement for conventional SCs and marked a major success of the BCS theory. Deviations from these formula serve as an important point of comparison for USCs.

References

[1] J. Bednorz and K. Mller, "High-T_c superconductivity in perovskite-type oxides," *Physica B+C*, vol. 148, no. 13, pp. 166 –, 1987.

[2] Y. Kamihara, T. Watanabe, M. Hirano, and H. Hosono, "Iron-Based Layered Superconductor $La[O_{1-x}F_x]FeAs$ (x = 0.05–0.12) with $T_c = 26$ K," *Journal of the American Chemical Society*, vol. 130, no. 11, pp. 3296–3297, 2008.

[3] M. Rotter, M. Tegel, and D. Johrendt, "Superconductivity at 38 K in the Iron Arsenide $(Ba_{1-x}K_x)Fe_2As_2$," *Phys. Rev. Lett.*, vol. 101, p. 107006, Sep 2008.

[4] J. Korringa, "On the calculation of the energy of a Bloch wave in a metal," *Physica*, vol. 13, no. 6–7, pp. 392 – 400, 1947.

[5] W. Kohn and N. Rostoker, "Solution of the Schrödinger Equation in Periodic Lattices with an Application to Metallic Lithium," *Phys. Rev.*, vol. 94, pp. 1111–1120, Jun 1954.

[6] D. D. Johnson, D. M. Nicholson, F. J. Pinski, B. L. Gyorffy, and G. M. Stocks, "Density-Functional Theory for Random Alloys: Total Energy within the Coherent-Potential Approximation," *Phys. Rev. Lett.*, vol. 56, pp. 2088–2091, May 1986.

[7] G. Grosso and G. P. Parravicini, *Solid State Physics*. Academic Press, 2000.

[8] J. B. Ketterson and S. N. Song, *Superconductivity*. Cambridge University Press, 1999.

[9] A. C. Rose-Innes and E. H. Rhoderick, *Introduction to Superconductivity*. Pergamon Press, 1969.

[10] M. Tinkham, *Introduction to Superconductivity*. McGraw-Hill, Inc., 1996.

[11] J. F. Annett, *Superconductivity, Superfluids, and Condensates*. Oxford University Press, 2004.

[12] A. A. Kordyuk, "Iron-based superconductors: Magnetism, superconductivity, and electronic structure," *Low Temperature Physics*, vol. 38, no. 9, pp. 888–899, 2012.

[13] M. D. Lumsden and A. D. Christianson, "Magnetism in Fe-based superconductors," *Journal of Physics: Condensed Matter*, vol. 22, no. 20, p. 203203, 2010.

[14] J. Paglione and R. L. Greene, "High-temperature superconductivity in iron-based materials," *Nat Phys*, vol. 6, pp. 645–658, Sep 2010.

[15] A. Chubukov, "Pairing Mechanism in Fe-Based Superconductors," *Annual Review of Condensed Matter Physics*, vol. 3, no. 1, pp. 57–92, 2012.

[16] G. R. Stewart, "Superconductivity in iron compounds," *Rev. Mod. Phys.*, vol. 83, pp. 1589–1652, Dec 2011.

[17] H.-H. Wen and S. Li, "Materials and Novel Superconductivity in Iron Pnictide Superconductors," *Annual Review of Condensed Matter Physics*, vol. 2, no. 1, pp. 121–140, 2011.

[18] Y. Izyumov and E. Kurmaev, *High-T_c Superconductors Based on FeAs Compounds*. Springer, 2010.

[19] I. I. Mazin, "Superconductivity gets an iron boost," *Nature*, vol. 464, pp. 183–186, Mar 2010.

[20] D. J. Scalapino, "A common thread: The pairing interaction for unconventional superconductors," *Rev. Mod. Phys.*, vol. 84, pp. 1383–1417, Oct 2012.

[21] M. R. Norman, "The Challenge of Unconventional Superconductivity," *Science*, vol. 332, no. 6026, pp. 196–200, 2011.

[22] S. He, J. He, W. Zhang, L. Zhao, D. Liu, X. Liu, D. Mou, Y.-B. Ou, Q.-Y. Wang, Z. Li, L. Wang, Y. Peng, Y. Liu, C. Chen, L. Yu, G. Liu, X. Dong, J. Zhang, C. Chen, Z. Xu, X. Chen, X. Ma, Q. Xue, and X. J. Zhou, "Phase diagram and electronic indication of high-temperature superconductivity at 65 K in single-layer FeSe films," *Nat Mater*, vol. 12, pp. 605–610, Jul 2013. Letter.

[23] L. Boeri, O. V. Dolgov, and A. A. Golubov, "Is $LaFeAsO_{1-x}F_x$ an Electron-Phonon Superconductor?," *Phys. Rev. Lett.*, vol. 101, p. 026403, Jul 2008.

[24] K. Haule, J. H. Shim, and G. Kotliar, "Correlated Electronic Structure of $LaO_{1-x}F_xFeAs$," *Phys. Rev. Lett.*, vol. 100, p. 226402, Jun 2008.

[25] H. Ogino, Y. Matsumura, Y. Katsura, K. Ushiyama, S. Horii, K. Kishio, and J. ichi Shimoyama, "Superconductivity at 17 K in $(Fe_2P_2)(Sr_4Sc_2O_6)$: a new superconducting layered pnictide oxide with a thick perovskite oxide layer," *Superconductor Science and Technology*, vol. 22, no. 7, p. 075008, 2009.

[26] Y. Mizuguchi and Y. Takano, "Review of Fe Chalcogenides as the Simplest Fe-Based Superconductor," *Journal of the Physical Society of Japan*, vol. 79, no. 10, p. 102001, 2010.

[27] K. Segawa and Y. Ando, "Magnetic and Transport Properties of FeAs Single Crystals," *Journal of the Physical Society of Japan*, vol. 78, no. 10, p. 104720, 2009.

[28] C.-H. Lee, A. Iyo, H. Eisaki, H. Kito, M. T. Fernandez-Diaz, T. Ito, K. Kihou, H. Matsuhata, M. Braden, and K. Yamada, "Effect of Structural Parameters on Superconductivity in Fluorine-Free $LnFeAsO_{1-y}$ (Ln = La, Nd)," *Journal of the Physical Society of Japan*, vol. 77, no. 8, p. 083704, 2008.

[29] M. Rotter, M. Pangerl, M. Tegel, and D. Johrendt, "Superconductivity and Crystal Structures of $(Ba_{1-x}K_x)Fe_2As_2$ (x=0-1)," *Angewandte Chemie International Edition*, vol. 47, no. 41, pp. 7949–7952, 2008.

[30] M. Gooch, B. Lv, K. Sasmal, J. Tapp, Z. Tang, A. Guloy, B. Lorenz, and C. Chu, "Superconductivity in ternary iron pnictides: AFe_2As_2 (A = alkali metal) and LiFeAs," *Physica C: Superconductivity*, vol. 470, Supplement 1, no. 0, pp. S276 – S279, 2010. Proceedings of the 9th International Conference on Materials and Mechanisms of Superconductivity.

[31] D. J. Singh, "Electronic structure and doping in $BaFe_2As_2$ and LiFeAs: Density functional calculations," *Phys. Rev. B*, vol. 78, p. 094511, Sep 2008.

[32] I. I. Mazin, M. D. Johannes, L. Boeri, K. Koepernik, and D. J. Singh, "Problems with reconciling density functional theory calculations with experiment in ferropnictides," *Phys. Rev. B*, vol. 78, p. 085104, Aug 2008.

[33] Z. P. Yin, S. Lebègue, M. J. Han, B. P. Neal, S. Y. Savrasov, and W. E. Pickett, "Electron-Hole Symmetry and Magnetic Coupling in Antiferromagnetic LaFeAsO," *Phys. Rev. Lett.*, vol. 101, p. 047001, Jul 2008.

[34] M. A. McGuire, A. D. Christianson, A. S. Sefat, B. C. Sales, M. D. Lumsden, R. Jin, E. A. Payzant, D. Mandrus, Y. Luan, V. Keppens, V. Varadarajan, J. W. Brill, R. P. Hermann, M. T. Sougrati, F. Grandjean, and G. J. Long, "Phase transitions in LaFeAsO: Structural, magnetic, elastic, and transport properties, heat capacity and Mössbauer spectra," *Phys. Rev. B*, vol. 78, p. 094517, Sep 2008.

[35] I. I. Mazin and M. D. Johannes, "A key role for unusual spin dynamics in ferropnictides," *Nat Phys*, vol. 5, pp. 141–145, Feb 2009.

[36] Z.-A. Ren, G.-C. Che, X.-L. Dong, J. Yang, W. Lu, W. Yi, X.-L. Shen, Z.-C. Li, L.-L. Sun, F. Zhou, and Z.-X. Zhao, "Superconductivity and phase diagram in iron-based arsenic-oxides $ReFeAsO_{1-\delta}$ (Re = rare-earth metal) without fluorine doping," *EPL (Europhysics Letters)*, vol. 83, no. 1, p. 17002, 2008.

[37] W. Lu, X.-L. Shen, J. Yang, Z.-C. Li, W. Yi, Z.-A. Ren, X.-L. Dong, G.-C. Che, L.-L. Sun, F. Zhou, and Z.-X. Zhao, "Superconductivity at 41.0 K in the F-doped $LaFeAsO_{1-x}F_x$," *Solid State Communications*, vol. 148, no. 34, pp. 168 – 170, 2008.

[38] P. J. W. Moll, R. Puzniak, F. Balakirev, K. Rogacki, J. Karpinski, N. D. Zhigadlo, and B. Batlogg, "High magnetic-field scales and critical currents in SmFeAs(O, F) crystals," *Nat Mater*, vol. 9, pp. 628–633, Aug 2010.

[39] C. Liu, Y. Lee, A. D. Palczewski, J.-Q. Yan, T. Kondo, B. N. Harmon, R. W. McCallum, T. A. Lograsso, and A. Kaminski, "Surface-driven electronic structure in LaFeAsO studied by angle-resolved photoemission spectroscopy," *Phys. Rev. B*, vol. 82, p. 075135, Aug 2010.

[40] M. Rotter, M. Tegel, D. Johrendt, I. Schellenberg, W. Hermes, and R. Pöttgen, "Spin-density-wave anomaly at 140 K in the ternary iron arsenide $BaFe_2As_2$," *Phys. Rev. B*, vol. 78, p. 020503, Jul 2008.

[41] P. Richard, T. Sato, K. Nakayama, T. Takahashi, and H. Ding, "Fe-based superconductors: an angle-resolved photoemission spectroscopy perspective," *Reports on Progress in Physics*, vol. 74, no. 12, p. 124512, 2011.

[42] M. A. Tanatar, A. Kreyssig, S. Nandi, N. Ni, S. L. Bud'ko, P. C. Canfield, A. I. Goldman, and R. Prozorov, "Direct imaging of the structural domains in the iron pnictides AFe_2As_2 A=Ca, Sr, Ba," *Phys. Rev. B*, vol. 79, p. 180508, May 2009.

[43] H. Xiao, T. Hu, A. P. Dioguardi, N. apRoberts Warren, A. C. Shockley, J. Crocker, D. M. Nisson, Z. Viskadourakis, X. Tee, I. Radulov, C. C. Almasan, N. J. Curro, and C. Panagopoulos, "Evidence for filamentary superconductivity nucleated at antiphase domain walls in antiferromagnetic $CaFe_2As_2$," *Phys. Rev. B*, vol. 85, p. 024530, Jan 2012.

[44] I. Morozov, A. Boltalin, O. Volkova, A. Vasiliev, O. Kataeva, U. Stockert, M. Abdel-Hafiez, D. Bombor, A. Bachmann, L. Harnagea, M. Fuchs, H.-J. Grafe, G. Behr, R. Klingeler, S. Borisenko, C. Hess, S. Wurmehl, and B. Buchner, "Single Crystal Growth and Characterization of Superconducting LiFeAs," *Crystal Growth & Design*, vol. 10, no. 10, pp. 4428–4432, 2010.

[45] S. V. Borisenko, V. B. Zabolotnyy, D. V. Evtushinsky, T. K. Kim, I. V. Morozov, A. N. Yaresko, A. A. Kordyuk, G. Behr, A. Vasiliev, R. Follath, and B. Büchner, "Superconductivity without Nesting in LiFeAs," *Phys. Rev. Lett.*, vol. 105, p. 067002, Aug 2010.

[46] G. F. Chen, W. Z. Hu, J. L. Luo, and N. L. Wang, "Multiple Phase Transitions in Single-Crystalline $Na_{1-\delta}FeAs$," *Phys. Rev. Lett.*, vol. 102, p. 227004, Jun 2009.

[47] J. Guo, S. Jin, G. Wang, S. Wang, K. Zhu, T. Zhou, M. He, and X. Chen, "Superconductivity in the iron selenide $K_xFe_2Se_2$ $(0.0 \leq x \leq 1.0)$," *Phys. Rev. B*, vol. 82, p. 180520, Nov 2010.

[48] S. V. Borisenko, A. N. Yaresko, D. V. Evtushinsky, V. B. Zabolotnyy, A. A. Kordyuk, J. Maletz, B. Bchner, Z. Shermadini, H. Luetkens, K. Sedlak, R. Khasanov, A. Amato, A. Krzton-Maziopa, K. Conder, E. Pomjakushina, H.-H. Klauss, and E. Rienks, ""Cigar" Fermi surface as a possible requisite for superconductivity in iron-based superconductors," 2012.

[49] C. Wang, L. Li, S. Chi, Z. Zhu, Z. Ren, Y. Li, Y. Wang, X. Lin, Y. Luo, S. Jiang, X. Xu, G. Cao, and Z. Xu, "Thorium-doping-induced superconductivity up to 56K in $Gd_{1-x}Th_xFeAsO$," *EPL (Europhysics Letters)*, vol. 83, no. 6, p. 67006, 2008.

[50] H.-H. Wen, G. Mu, L. Fang, H. Yang, and X. Zhu, "Superconductivity at 25K in hole-doped ($La_{1-x}Sr_x$)OFeAs," *EPL (Europhysics Letters)*, vol. 82, no. 1, p. 17009, 2008.

[51] C. R. Rotundu, D. T. Keane, B. Freelon, S. D. Wilson, A. Kim, P. N. Valdivia, E. Bourret-Courchesne, and R. J. Birgeneau, "Phase diagram of the $PrFeAsO_{1-x}F_x$ superconductor," *Phys. Rev. B*, vol. 80, p. 144517, Oct 2009.

[52] H.-H. Wen and S. Li, "Materials and Novel Superconductivity in Iron Pnictide Superconductors," *Annual Review of Condensed Matter Physics*, vol. 2, no. 1, pp. 121–140, 2011.

[53] S. Nandi, M. G. Kim, A. Kreyssig, R. M. Fernandes, D. K. Pratt, A. Thaler, N. Ni, S. L. Bud'ko, P. C. Canfield, J. Schmalian, R. J. McQueeney, and A. I. Goldman, "Anomalous Suppression of the Orthorhombic Lattice Distortion in Superconducting ($Ba_{1-x}K_x$)Fe_2As_2 Single Crystals," *Phys. Rev. Lett.*, vol. 104, p. 057006, Feb 2010.

[54] E. Fawcett, H. L. Alberts, V. Y. Galkin, D. R. Noakes, and J. V. Yakhmi, "Spin-density-wave antiferromagnetism in chromium alloys," *Rev. Mod. Phys.*, vol. 66, pp. 25–127, Jan 1994.

[55] Q. Huang, J. Zhao, J. W. Lynn, G. F. Chen, J. L. Luo, N. L. Wang, and P. Dai, "Doping evolution of antiferromagnetic order and structural distortion in $LaFeAsO_{1-x}F_x$," *Phys. Rev. B*, vol. 78, p. 054529, Aug 2008.

[56] R. Cimberle, C. Ferdeghini, F. Canepa, M. Ferretti, A. Martinelli, A. Palenzona, A. S. Siri, and M. Tropeano, "Magnetic properties of undoped and 15% f doped smfeaso compounds," 2008.

[57] R. M. Fernandes, A. V. Chubukov, and J. Schmalian, "What drives nematic order in iron-based superconductors?," *Nat Phys*, vol. 10, pp. 97–104, Feb 2014. Review.

[58] J. Zhao, Q. Huang, C. de la Cruz, S. Li, J. W. Lynn, Y. Chen, M. A. Green, G. F. Chen, G. Li, Z. Li, J. L. Luo, N. L. Wang, and P. Dai, "Structural and magnetic phase diagram of $CeFeAsO_{1-x}F_x$ and its relation to high-temperature superconductivity," *Nat Mater*, vol. 7, pp. 953–959, Dec 2008.

[59] S. Margadonna, Y. Takabayashi, M. T. McDonald, M. Brunelli, G. Wu, R. H. Liu, X. H. Chen, and K. Prassides, "Crystal structure and phase transitions across the metal-superconductor boundary in the $SmFeAsO_{1-x}F_x$ ($0 \leq x \leq 0.20$) family," *Phys. Rev. B*, vol. 79, p. 014503, Jan 2009.

[60] J. T. Park, D. S. Inosov, C. Niedermayer, G. L. Sun, D. Haug, N. B. Christensen, R. Dinnebier, A. V. Boris, A. J. Drew, L. Schulz, T. Shapoval, U. Wolff, V. Neu, X. Yang, C. T. Lin, B. Keimer, and V. Hinkov, "Electronic Phase Separation in the Slightly Underdoped Iron Pnictide Superconductor $Ba_{1-x}K_xFe_2As_2$," *Phys. Rev. Lett.*, vol. 102, p. 117006, Mar 2009.

[61] M.-H. Julien, H. Mayaffre, M. Horvati, C. Berthier, X. D. Zhang, W. Wu, G. F. Chen, N. L. Wang, and J. L. Luo, "Homogeneous vs. inhomogeneous coexistence of magnetic order and superconductivity probed by NMR in Co- and K-doped iron pnictides," *EPL (Europhysics Letters)*, vol. 87, no. 3, p. 37001, 2009.

[62] D. K. Pratt, M. G. Kim, A. Kreyssig, Y. B. Lee, G. S. Tucker, A. Thaler, W. Tian, J. L. Zarestky, S. L. Bud'ko, P. C. Canfield, B. N. Harmon, A. I. Goldman, and R. J. McQueeney, "Incommensurate Spin-Density Wave Order in Electron-Doped $BaFe_2As_2$ Superconductors," *Phys. Rev. Lett.*, vol. 106, p. 257001, Jun 2011.

[63] L. W. Harriger, A. Schneidewind, S. Li, J. Zhao, Z. Li, W. Lu, X. Dong, F. Zhou, Z. Zhao, J. Hu, and P. Dai, "Transition from Three-Dimensional Anisotropic Spin Excitations to Two-Dimensional Spin Excitations by Electron Doping the FeAs-Based $BaFe_{1.96}Ni_{0.04}As_2$ Superconductor," *Phys. Rev. Lett.*, vol. 103, p. 087005, Aug 2009.

[64] S. Jiang, H. Xing, G. Xuan, C. Wang, Z. Ren, C. Feng, J. Dai, Z. Xu, and G. Cao, "Superconductivity up to 30 K in the vicinity of the quantum critical point in $BaFe_2(As_{1-x}P_x)_2$," *Journal of Physics: Condensed Matter*, vol. 21, no. 38, p. 382203, 2009.

[65] J.-P. Reid, M. A. Tanatar, A. Juneau-Fecteau, R. T. Gordon, S. R. de Cotret, N. Doiron-Leyraud, T. Saito, H. Fukazawa, Y. Kohori, K. Kihou, C. H. Lee, A. Iyo, H. Eisaki, R. Prozorov, and L. Taillefer, "Universal Heat Conduction in the Iron Arsenide Superconductor KFe_2As_2: Evidence of a d-Wave State," *Phys. Rev. Lett.*, vol. 109, p. 087001, Aug 2012.

[66] W. Li, J. Li, J.-X. Zhu, Y. Chen, and C. S. Ting, "Pairing symmetry in the iron-pnictide superconductor KFe_2As_2," *EPL (Europhysics Letters)*, vol. 99, no. 5, p. 57006, 2012.

[67] L. Ma, G. F. Chen, D.-X. Yao, J. Zhang, S. Zhang, T.-L. Xia, and W. Yu, "^{23}Na and ^{75}As NMR study of antiferromagnetism and spin fluctuations in NaFeAs single crystals," *Phys. Rev. B*, vol. 83, p. 132501, Apr 2011.

[68] W. Lv and P. Phillips, "Orbitally and magnetically induced anisotropy in iron-based superconductors," *Phys. Rev. B*, vol. 84, p. 174512, Nov 2011.

[69] C.-C. Chen, J. Maciejko, A. P. Sorini, B. Moritz, R. R. P. Singh, and T. P. Devereaux, "Orbital order and spontaneous orthorhombicity in iron pnictides," *Phys. Rev. B*, vol. 82, p. 100504, Sep 2010.

[70] E. C. Blomberg, M. A. Tanatar, R. M. Fernandes, I. I. Mazin, B. Shen, H.-H. Wen, M. D. Johannes, J. Schmalian, and R. Prozorov, "Sign-reversal of the in-plane resistivity anisotropy in hole-doped iron pnictides," *Nat Commun*, vol. 4, p. 1914, May 2013. Article.

[71] H. Lee, E. Park, T. Park, V. A. Sidorov, F. Ronning, E. D. Bauer, and J. D. Thompson, "Pressure-induced superconducting state of antiferromagnetic $CaFe_2As_2$," *Phys. Rev. B*, vol. 80, p. 024519, Jul 2009.

[72] J. Wu, P. Phillips, and A. H. Castro Neto, "Theory of the Magnetic Moment in Iron Pnictides," *Phys. Rev. Lett.*, vol. 101, p. 126401, Sep 2008.

[73] W. Lu, J. Yang, X. L. Dong, Z. A. Ren, G. C. Che, and Z. X. Zhao, "Pressure effect on superconducting properties of $LaO_{1-x}F_xFeAs$ (x =0.11) superconductor," *New Journal of Physics*, vol. 10, no. 6, p. 063026, 2008.

[74] P. L. Alireza, Y. T. C. Ko, J. Gillett, C. M. Petrone, J. M. Cole, G. G. Lonzarich, and S. E. Sebastian, "Superconductivity up to 29 K in $SrFe_2As_2$ and $BaFe_2As_2$ at high pressures," *Journal of Physics: Condensed Matter*, vol. 21, no. 1, p. 012208, 2009.

[75] E. Colombier, S. L. Bud'ko, N. Ni, and P. C. Canfield, "Complete pressure-dependent phase diagrams for $SrFe_2As_2$ and $BaFe_2As_2$," *Phys. Rev. B*, vol. 79, p. 224518, Jun 2009.

[76] F. Ishikawa, N. Eguchi, M. Kodama, K. Fujimaki, M. Einaga, A. Ohmura, A. Nakayama, A. Mitsuda, and Y. Yamada, "Zero-resistance superconducting phase in $BaFe_2As_2$ under high pressure," *Phys. Rev. B*, vol. 79, p. 172506, May 2009.

[77] A. Kreyssig, M. A. Green, Y. Lee, G. D. Samolyuk, P. Zajdel, J. W. Lynn, S. L. Bud'ko, M. S. Torikachvili, N. Ni, S. Nandi, J. B. Leão, S. J. Poulton, D. N. Argyriou, B. N. Harmon, R. J. McQueeney, P. C. Canfield, and A. I. Goldman, "Pressure-induced volume-collapsed tetragonal phase of $CaFe_2As_2$ as seen via neutron scattering," *Phys. Rev. B*, vol. 78, p. 184517, Nov 2008.

[78] C. Liu, T. Kondo, R. M. Fernandes, A. D. Palczewski, E. D. Mun, N. Ni, A. N. Thaler, A. Bostwick, E. Rotenberg, J. Schmalian, S. L. Bud/'ko, P. C. Canfield, and A. Kaminski, "Evidence for a Lifshitz transition in electron-doped iron arsenic superconductors at the onset of superconductivity," *Nat Phys*, vol. 6, pp. 419–423, Jun 2010.

[79] P. Hansmann, R. Arita, A. Toschi, S. Sakai, G. Sangiovanni, and K. Held, "Dichotomy between Large Local and Small Ordered Magnetic Moments in Iron-Based Superconductors," *Phys. Rev. Lett.*, vol. 104, p. 197002, May 2010.

[80] T. Kondo, R. M. Fernandes, R. Khasanov, C. Liu, A. D. Palczewski, N. Ni, M. Shi, A. Bostwick, E. Rotenberg, J. Schmalian, S. L. Bud'ko, P. C. Canfield, and A. Kaminski, "Unexpected Fermi-surface nesting in the pnictide parent compounds $BaFe_2As_2$ and $CaFe_2As_2$ revealed by angle-resolved photoemission spectroscopy," *Phys. Rev. B*, vol. 81, p. 060507, Feb 2010.

[81] V. Brouet, M. Marsi, B. Mansart, A. Nicolaou, A. Taleb-Ibrahimi, P. Le Fèvre, F. Bertran, F. Rullier-Albenque, A. Forget, and D. Colson, "Nesting between hole and electron pockets in $Ba(Fe_{1-x}Co_x)_2As_2$ (x=0–0.3) observed with angle-resolved photoemission," *Phys. Rev. B*, vol. 80, p. 165115, Oct 2009.

[82] D. J. Singh and M.-H. Du, "Density Functional Study of $LaFeAsO_{1-x}F_x$: A Low Carrier Density Superconductor Near Itinerant Magnetism," *Phys. Rev. Lett.*, vol. 100, p. 237003, Jun 2008.

[83] W. Setyawan and S. Curtarolo, "High-throughput electronic band structure calculations: Challenges and tools ," *Computational Materials Science*, vol. 49, no. 2, pp. 299 – 312, 2010.

[84] P. J. Hirschfeld, M. M. Korshunov, and I. I. Mazin, "Gap symmetry and structure of Fe-based superconductors," *Reports on Progress in Physics*, vol. 74, no. 12, p. 124508, 2011.

[85] S. Ideta, T. Yoshida, I. Nishi, A. Fujimori, Y. Kotani, K. Ono, Y. Nakashima, S. Yamaichi, T. Sasagawa, M. Nakajima, K. Kihou, Y. Tomioka, C. H. Lee, A. Iyo, H. Eisaki, T. Ito, S. Uchida, and R. Arita, "Dependence of Carrier Doping on the Impurity Potential in Transition-Metal-Substituted FeAs-Based Superconductors," *Phys. Rev. Lett.*, vol. 110, p. 107007, Mar 2013.

[86] G. Grüner, "The dynamics of charge-density waves," *Rev. Mod. Phys.*, vol. 60, pp. 1129–1181, Oct 1988.

[87] W. Bao, Y. Qiu, Q. Huang, M. A. Green, P. Zajdel, M. R. Fitzsimmons, M. Zhernenkov, S. Chang, M. Fang, B. Qian, E. K. Vehstedt, J. Yang, H. M. Pham, L. Spinu, and Z. Q. Mao, "Tunable $(\delta\pi, \delta\pi)$-Type Antiferromagnetic Order in α-Fe(Te,Se) Superconductors," *Phys. Rev. Lett.*, vol. 102, p. 247001, Jun 2009.

[88] S. O. Diallo, V. P. Antropov, T. G. Perring, C. Broholm, J. J. Pulikkotil, N. Ni, S. L. Bud'ko, P. C. Canfield, A. Kreyssig, A. I. Goldman, and R. J. McQueeney, "Itinerant Magnetic Excitations in Antiferromagnetic $CaFe_2As_2$," *Phys. Rev. Lett.*, vol. 102, p. 187206, May 2009.

[89] J. Zhao, D. T. Adroja, D.-X. Yao, R. Bewley, S. Li, X. F. Wang, G. Wu, X. H. Chen, J. Hu, and P. Dai, "Spin waves and magnetic exchange interactions in $CaFe_2As_2$," *Nat Phys*, vol. 5, pp. 555–560, Aug 2009.

[90] N. Xu, P. Richard, X. Shi, A. van Roekeghem, T. Qian, E. Razzoli, E. Rienks, G.-F. Chen, E. Ieki, K. Nakayama, T. Sato, T. Takahashi, M. Shi, and H. Ding, "Possible nodal superconducting gap and Lifshitz transition in heavily hole-doped $Ba_{0.1}K_{0.9}Fe_2As_2$," *Phys. Rev. B*, vol. 88, p. 220508, Dec 2013.

[91] M. Yi, D. H. Lu, J. G. Analytis, J.-H. Chu, S.-K. Mo, R.-H. He, R. G. Moore, X. J. Zhou, G. F. Chen, J. L. Luo, N. L. Wang, Z. Hussain, D. J. Singh, I. R. Fisher, and Z.-X. Shen, "Electronic structure of the $BaFe_2As_2$ family of iron-pnictide superconductors," *Phys. Rev. B*, vol. 80, p. 024515, Jul 2009.

[92] J.-P. Castellan, S. Rosenkranz, E. A. Goremychkin, D. Y. Chung, I. S. Todorov, M. G. Kanatzidis, I. Eremin, J. Knolle, A. V. Chubukov, S. Maiti, M. R. Norman, F. Weber, H. Claus, T. Guidi, R. I. Bewley, and R. Osborn, "Effect of Fermi Surface Nesting on Resonant Spin Excitations in $Ba_{1-x}K_xFe_2As_2$," *Phys. Rev. Lett.*, vol. 107, p. 177003, Oct 2011.

[93] H. Gretarsson, A. Lupascu, J. Kim, D. Casa, T. Gog, W. Wu, S. R. Julian, Z. J. Xu, J. S. Wen, G. D. Gu, R. H. Yuan, Z. G. Chen, N.-L. Wang, S. Khim, K. H. Kim, M. Ishikado, I. Jarrige, S. Shamoto, J.-H. Chu, I. R. Fisher, and Y.-J. Kim, "Revealing the dual nature of magnetism in iron pnictides and iron chalcogenides using x-ray emission spectroscopy," *Phys. Rev. B*, vol. 84, p. 100509, Sep 2011.

[94] C. de la Cruz, Q. Huang, J. W. Lynn, J. Li, W. R. II, J. L. Zarestky, H. A. Mook, G. F. Chen, J. L. Luo, N. L. Wang, and P. Dai, "Magnetic order close to superconductivity in the iron-based layered $LaO_{1-x}F_xFeAs$ systems," *Nature*, vol. 453, pp. 899–902, Jun 2008.

[95] Q. Huang, Y. Qiu, W. Bao, M. A. Green, J. W. Lynn, Y. C. Gasparovic, T. Wu, G. Wu, and X. H. Chen, "Neutron-Diffraction Measurements of Magnetic Order and a Structural Transition in the Parent $BaFe_2As_2$ Compound of FeAs-Based High-Temperature Superconductors," *Phys. Rev. Lett.*, vol. 101, p. 257003, Dec 2008.

[96] M. Liu, L. W. Harriger, H. Luo, M. Wang, R. A. Ewings, T. Guidi, H. Park, K. Haule, G. Kotliar, S. M. Hayden, and P. Dai, "Nature of magnetic excitations in superconducting $BaFe_{1.9}Ni_{0.1}As_2$," *Nat Phys*, vol. 8, pp. 376–381, May 2012.

[97] H. Park, K. Haule, and G. Kotliar, "Magnetic Excitation Spectra in $BaFe_2As_2$: A Two-Particle Approach within a Combination of the Density Functional Theory and the Dynamical Mean-Field Theory Method," *Phys. Rev. Lett.*, vol. 107, p. 137007, Sep 2011.

[98] Z. P. Yin, K. Haule, and G. Kotliar, "Kinetic frustration and the nature of the magnetic and paramagnetic states in iron pnictides and iron chalcogenides," *Nat Mater*, vol. 10, pp. 932–935, Dec 2011.

[99] M. Daghofer, A. Nicholson, A. Moreo, and E. Dagotto, "Three orbital model for the iron-based superconductors," *Phys. Rev. B*, vol. 81, p. 014511, Jan 2010.

[100] Q. Luo, G. Martins, D.-X. Yao, M. Daghofer, R. Yu, A. Moreo, and E. Dagotto, "Neutron and ARPES constraints on the couplings of the multiorbital Hubbard model for the iron pnictides," *Phys. Rev. B*, vol. 82, p. 104508, Sep 2010.

[101] L. W. Harriger, H. Q. Luo, M. S. Liu, C. Frost, J. P. Hu, M. R. Norman, and P. Dai, "Nematic spin fluid in the tetragonal phase of $BaFe_2As_2$," *Phys. Rev. B*, vol. 84, p. 054544, Aug 2011.

[102] O. J. Lipscombe, G. F. Chen, C. Fang, T. G. Perring, D. L. Abernathy, A. D. Christianson, T. Egami, N. Wang, J. Hu, and P. Dai, "Spin Waves in the $(\pi, 0)$ Magnetically Ordered Iron Chalcogenide $Fe_{1.05}Te$," *Phys. Rev. Lett.*, vol. 106, p. 057004, Feb 2011.

[103] M. Wang, C. Fang, D.-X. Yao, G. Tan, L. W. Harriger, Y. Song, T. Netherton, C. Zhang, M. Wang, M. B. Stone, W. Tian, J. Hu, and P. Dai, "Spin waves and magnetic exchange interactions in insulating $Rb_{0.89}Fe_{1.58}Se_2$," *Nat Commun*, vol. 2, p. 580, Dec 2011.

[104] F. L. Ning, K. Ahilan, T. Imai, A. S. Sefat, M. A. McGuire, B. C. Sales, D. Mandrus, P. Cheng, B. Shen, and H.-H. Wen, "Contrasting Spin Dynamics between Underdoped and Overdoped $Ba(Fe_{1-x}Co_x)_2As_2$)," *Phys. Rev. Lett.*, vol. 104, p. 037001, Jan 2010.

[105] S. Wakimoto, K. Kodama, M. Ishikado, M. Matsuda, R. Kajimoto, M. Arai, K. Kakurai, F. Esaka, A. Iyo, H. Kito, H. Eisaki, and S.-i. Shamoto, "Degradation of Superconductivity and Spin Fluctuations by Electron Overdoping in $LaFeAsO_{1-x}F_x$," *Journal of the Physical Society of Japan*, vol. 79, no. 7, p. 074715, 2010.

[106] C. Lester, J.-H. Chu, J. G. Analytis, T. G. Perring, I. R. Fisher, and S. M. Hayden, "Dispersive spin fluctuations in the nearly optimally doped superconductor $Ba(Fe_{1-x}Co_x)_2As_2$ (x=0.065)," *Phys. Rev. B*, vol. 81, p. 064505, Feb 2010.

[107] S. O. Diallo, D. K. Pratt, R. M. Fernandes, W. Tian, J. L. Zarestky, M. Lumsden, T. G. Perring, C. L. Broholm, N. Ni, S. L. Bud'ko, P. C. Canfield, H.-F. Li, D. Vaknin, A. Kreyssig, A. I. Goldman, and R. J. McQueeney, "Paramagnetic spin correlations in $CaFe_2As_2$ single crystals," *Phys. Rev. B*, vol. 81, p. 214407, Jun 2010.

[108] M. M. Korshunov and I. Eremin, "Theory of magnetic excitations in iron-based layered superconductors," *Phys. Rev. B*, vol. 78, p. 140509, Oct 2008.

[109] S. L. Bud'ko, N. Ni, and P. C. Canfield, "Jump in specific heat at the superconducting transition temperature in $Ba(Fe_{1-x}Co_x)_2As_2$ and $Ba(Fe_{1-x}Ni_x)_2As_2$ single crystals," *Phys. Rev. B*, vol. 79, p. 220516, Jun 2009.

[110] H. Oh, J. Moon, D. Shin, C.-Y. Moon, and H. J. Choi, "Brief review on iron-based superconductors: are there clues for unconventional superconductivity?," *Progress in Superconductivity*, vol. 13, pp. 65–84, 2011.

[111] C. W. Hicks, T. M. Lippman, M. E. Huber, Z.-A. Ren, J. Yang, Z.-X. Zhao, and K. A. Moler, "Limits on the Superconducting Order Parameter in $NdFeAsO_{1-x}F_y$ from Scanning SQUID Microscopy," *Journal of the Physical Society of Japan*, vol. 78, no. 1, p. 013708, 2009.

[112] P. Richard, T. Sato, K. Nakayama, S. Souma, T. Takahashi, Y.-M. Xu, G. F. Chen, J. L. Luo, N. L. Wang, and H. Ding, "Angle-Resolved Photoemission Spectroscopy of the Fe-Based $Ba_{1-x}K_xFe_2As_2$ High Temperature Superconductor: Evidence for an Orbital Selective Electron-Mode Coupling," *Phys. Rev. Lett.*, vol. 102, p. 047003, Jan 2009.

[113] P. Soven, "Coherent-Potential Model of Substitutional Disordered Alloys," *Phys. Rev.*, vol. 156, pp. 809–813, Apr 1967.

[114] D. W. Taylor, "Vibrational Properties of Imperfect Crystals with Large Defect Concentrations," *Phys. Rev.*, vol. 156, pp. 1017–1029, Apr 1967.

[115] S. Ghosh, D. A. Biava, W. A. Shelton, and D. D. Johnson, "Systematically exact integrated density-of-states Lloyds formula for disordered alloys with short-range order," *Phys. Rev. B*, vol. 73, p. 085106, Feb 2006.

[116] R. Zeller, "An elementary derivation of Lloyd's formula valid for full-potential multiple-scattering theory," *Journal of Physics: Condensed Matter*, vol. 16, no. 36, p. 6453, 2004.

[117] P. Lloyd, "Wave propagation through an assembly of spheres: II. The density of single-particle eigenstates," *Proceedings of the Physical Society*, vol. 90, no. 1, p. 207, 1967.

[118] A. Lodder and P. J. Braspenning, "Generalized Lloyd formula for the electron density of states," *Phys. Rev. B*, vol. 49, pp. 10215–10221, Apr 1994.

[119] A. Lodder and J. P. Dekker, "Generalized Friedel sum from Lloyds formula," *Phys. Rev. B*, vol. 49, pp. 10206–10214, Apr 1994.

[120] J. S. Faulkner and G. M. Stocks, "Calculating properties with the coherent-potential approximation," *Phys. Rev. B*, vol. 21, pp. 3222–3244, Apr 1980.

[121] J. Faulkner, "The modern theory of alloys ," *Progress in Materials Science*, vol. 27, no. 12, pp. 1 – 187, 1982.

[122] A. Alam, S. N. Khan, B. G. Wilson, and D. D. Johnson, "Efficient isoparametric integration over arbitrary space-filling Voronoi polyhedra for electronic structure calculations," *Phys. Rev. B*, vol. 84, p. 045105, Jul 2011.

[123] P. M. Boerrigter, G. Te Velde, and J. E. Baerends, "Three-dimensional numerical integration for electronic structure calculations," *International Journal of Quantum Chemistry*, vol. 33, no. 2, pp. 87–113, 1988.

[124] G. te Velde and E. Baerends, "Numerical integration for polyatomic systems ," *Journal of Computational Physics*, vol. 99, no. 1, pp. 84 – 98, 1992.

[125] J. van W Morgan, "Integration of Poisson's equation for a complex system with arbitrary geometry," *Journal of Physics C: Solid State Physics*, vol. 10, no. 8, p. 1181, 1977.

[126] J. Bernal, "FORTRAN codes for Voronoi tessellation and Delauney triangulations," 2010.

[127] Y. Wang, G. M. Stocks, and J. S. Faulkner, "General method for evaluating shape truncation functions of Voronoi polyhedra," *Phys. Rev. B*, vol. 49, pp. 5028–5031, Feb 1994.

[128] N. Ni, M. E. Tillman, J.-Q. Yan, A. Kracher, S. T. Hannahs, S. L. Bud'ko, and P. C. Canfield, "Effects of Co substitution on thermodynamic and transport properties and anisotropic H_{c2} in $Ba(Fe_{1-x}Co_x)_2As_2$ single crystals," *Phys. Rev. B*, vol. 78, p. 214515, Dec 2008.

[129] N. Ni, A. Thaler, J. Q. Yan, A. Kracher, E. Colombier, S. L. Bud'ko, P. C. Canfield, and S. T. Hannahs, "Temperature versus doping phase diagrams for $Ba(Fe_{1-x}TM_x)_2As_2$ (TM=Ni,Cu,Cu/Co) single crystals," *Phys. Rev. B*, vol. 82, p. 024519, Jul 2010.

[130] Y. Nishihara, Y. Yamaguchi, M. Tokumoto, K. Takeda, and K. Fukamichi, "Superconductivity and magnetism of bcc Cr-Ru alloys," *Phys. Rev. B*, vol. 34, pp. 3446–3449, Sep 1986.

[131] S. K. Burke and B. D. Rainford, "Determination of the antiferromagnetic phase boundary in Cr-Fe alloys," *Journal of Physics F: Metal Physics*, vol. 8, no. 10, p. L239, 1978.

[132] G. Schadler, P. Weinberger, A. Gonis, and J. Klima, "Bloch spectral functions for complex lattices: applications to substoichiometric TiN_x and the Fermi surface of TiN_x," *Journal of Physics F: Metal Physics*, vol. 15, no. 8, p. 1675, 1985.

[133] E. Aktürk and S. Ciraci, "First-principles study of the iron pnictide superconductor $BaFe_2As_2$," *Phys. Rev. B*, vol. 79, p. 184523, May 2009.

[134] J. Fink, S. Thirupathaiah, R. Ovsyannikov, H. A. Dürr, R. Follath, Y. Huang, S. de Jong, M. S. Golden, Y.-Z. Zhang, H. O. Jeschke, R. Valentí, C. Felser, S. Dastjani Farahani, M. Rotter, and D. Johrendt, "Electronic structure studies of $BaFe_2As_2$ by angle-resolved photoemission spectroscopy," *Phys. Rev. B*, vol. 79, p. 155118, Apr 2009.

[135] P. Richard, K. Nakayama, T. Sato, M. Neupane, Y.-M. Xu, J. H. Bowen, G. F. Chen, J. L. Luo, N. L. Wang, X. Dai, Z. Fang, H. Ding, and T. Takahashi, "Observation of Dirac Cone Electronic Dispersion in $BaFe_2As_2$," *Phys. Rev. Lett.*, vol. 104, p. 137001, Mar 2010.

[136] W. Malaeb, T. Yoshida, A. Fujimori, M. Kubota, K. Ono, K. Kihou, P. M. Shirage, H. Kito, A. Iyo, H. Eisaki, Y. Nakajima, T. Tamegai, and R. Arita, "Three-Dimensional Electronic Structure of Superconducting Iron Pnictides Observed by Angle-Resolved Photoemission Spectroscopy," *Journal of the Physical Society of Japan*, vol. 78, no. 12, p. 123706, 2009.

[137] K. Matan, S. Ibuka, R. Morinaga, S. Chi, J. W. Lynn, A. D. Christianson, M. D. Lumsden, and T. J. Sato, "Doping dependence of spin dynamics in electron-doped $Ba(Fe_{1-x}Co_x)_2As_2$," *Phys. Rev. B*, vol. 82, p. 054515, Aug 2010.

[138] T. D. Stanescu, V. Galitski, and S. Das Sarma, "Orbital fluctuation mechanism for superconductivity in iron-based compounds," *Phys. Rev. B*, vol. 78, p. 195114, Nov 2008.

[139] J.-H. Chu, J. G. Analytis, C. Kucharczyk, and I. R. Fisher, "Determination of the phase diagram of the electron-doped superconductor $Ba(Fe_{1-x}Co_x)_2As_2$," *Phys. Rev. B*, vol. 79, p. 014506, Jan 2009.

[140] M. G. Kim, J. Lamsal, T. W. Heitmann, G. S. Tucker, D. K. Pratt, S. N. Khan, Y. B. Lee, A. Alam, A. Thaler, N. Ni, S. Ran, S. L. Bud'ko, K. J. Marty, M. D. Lumsden, P. C. Canfield, B. N. Harmon, D. D. Johnson, A. Kreyssig, R. J. McQueeney, and A. I. Goldman, "Effects of Transition Metal Substitutions on the Incommensurability and Spin Fluctuations in $BaFe_2As_2$ by Elastic and Inelastic Neutron Scattering," *Phys. Rev. Lett.*, vol. 109, p. 167003, Oct 2012.

[141] S. Ideta, T. Yoshida, M. Nakajima, W. Malaeb, T. Shimojima, K. Ishizaka, A. Fujimori, H. Kimigashira, K. Ono, K. Kihou, Y. Tomioka, C. H. Lee, A. Iyo, H. Eisaki, T. Ito, and S. Uchida, "Effects of Zn substitution on the electronic structure of $BaFe_2As_2$ revealed by angle-resolved photoemission spectroscopy," *Phys. Rev. B*, vol. 87, p. 201110, May 2013.

[142] A. S. Sefat, D. J. Singh, R. Jin, M. A. McGuire, B. C. Sales, and D. Mandrus, "Renormalized behavior and proximity of $BaCo_2As_2$ to a magnetic quantum critical point," *Phys. Rev. B*, vol. 79, p. 024512, Jan 2009.

[143] D. J. Singh, "Electronic structure of $BaCu_2As_2$ and $SrCu_2As_2$ *sp*-band metals," *Phys. Rev. B*, vol. 79, p. 153102, Apr 2009.

[144] K. Kudo, M. Takasuga, Y. Okamoto, Z. Hiroi, and M. Nohara, "Giant Phonon Softening and Enhancement of Superconductivity by Phosphorus Doping of $BaNi_2As_2$," *Phys. Rev. Lett.*, vol. 109, p. 097002, Aug 2012.

[145] Z. Xiao, F.-Y. Ran, H. Hiramatsu, S. Matsuishi, H. Hosono, and T. Kamiya, "Epitaxial growth and electronic structure of a layered zinc pnictide semiconductor, β-$BaZn_2As_2$," *Thin Solid Films*, no. 0, pp. –, 2013.

[146] J. M. Luttinger, "Fermi Surface and Some Simple Equilibrium Properties of a System of Interacting Fermions," *Phys. Rev.*, vol. 119, pp. 1153–1163, Aug 1960.

[147] T. Berlijn, C.-H. Lin, W. Garber, and W. Ku, "Do Transition-Metal Substitutions Dope Carriers in Iron-Based Superconductors?," *Phys. Rev. Lett.*, vol. 108, p. 207003, May 2012.

[148] H. Wadati, I. Elfimov, and G. A. Sawatzky, "Where Are the Extra *d* Electrons in Transition-Metal-Substituted Iron Pnictides?," *Phys. Rev. Lett.*, vol. 105, p. 157004, Oct 2010.

[149] A. Alam, B. Kraczek, and D. D. Johnson, "Structural, magnetic, and defect properties of Co-Pt-type magnetic-storage alloys: Density-functional theory study of thermal processing effects," *Phys. Rev. B*, vol. 82, p. 024435, Jul 2010.

[150] B. L. Gyorffy, A. J. Pindor, J. Staunton, G. M. Stocks, and H. Winter, "A first-principles theory of ferromagnetic phase transitions in metals," *Journal of Physics F: Metal Physics*, vol. 15, no. 6, p. 1337, 1985.

[151] D. A. Biava, S. Ghosh, D. D. Johnson, W. A. Shelton, and A. V. Smirnov, "Systematic, multisite short-range-order corrections to the electronic structure of disordered alloys from first principles: The KKR nonlocal CPA from the dynamical cluster approximation," *Phys. Rev. B*, vol. 72, p. 113105, Sep 2005.

[152] B. L. Gyorffy and G. M. Stocks, "Concentration Waves and Fermi Surfaces in Random Metallic Alloys," *Phys. Rev. Lett.*, vol. 50, pp. 374–377, Jan 1983.

[153] P. Vilmercati, A. Fedorov, F. Bondino, F. Offi, G. Panaccione, P. Lacovig, L. Simonelli, M. A. McGuire, A. S. M. Sefat, D. Mandrus, B. C. Sales, T. Egami, W. Ku, and N. Mannella, "Itinerant electrons, local moments, and magnetic correlations in the pnictide superconductors $CeFeAsO_{1-x}F_x$ and $Sr(Fe_{1-x}Co_x)_2As_2$," *Phys. Rev. B*, vol. 85, p. 220503, Jun 2012.

[154] V. Crisan, P. Entel, H. Ebert, H. Akai, D. D. Johnson, and J. B. Staunton, "Magnetochemical origin for Invar anomalies in iron-nickel alloys," *Phys. Rev. B*, vol. 66, p. 014416, Jul 2002.

[155] H. J. Monkhorst and J. D. Pack, "Special points for Brillouin-zone integrations," *Phys. Rev. B*, vol. 13, pp. 5188–5192, Jun 1976.

[156] D. D. Johnson, F. J. Pinski, and G. M. Stocks, "Fast method for calculating the self-consistent electronic structure of random alloys," *Phys. Rev. B*, vol. 30, pp. 5508–5515, Nov 1984.

[157] A. J. Pindor, W. M. Temmerman, B. L. Gyorffy, and G. M. Stocks, "On the electronic structure of Ag c Pd 1-c alloys," *Journal of Physics F: Metal Physics*, vol. 10, no. 12, p. 2617, 1980.

[158] W. H. Butler and G. M. Stocks, "Calculated electrical conductivity and thermopower of silver-palladium alloys," *Phys. Rev. B*, vol. 29, pp. 4217–4223, Apr 1984.

[159] Free energy change per atom is the formation energy plus the ideal mixing entropy, i.e., $\Delta s = (2/5)k_B T[x\log(x) + (1-x)\log(1-x)]$, with annealing T=1000 °C. The 2/5 arises because Fe/M occupy only 2/5 of all sites.

[160] J. B. Staunton, D. D. Johnson, and F. J. Pinski, "Theory of compositional and magnetic correlations in alloys: Interpretation of a diffuse neutron-scattering experiment on an iron-vanadium single crystal," *Phys. Rev. Lett.*, vol. 65, pp. 1259–1262, Sep 1990.

[161] F. J. Pinski, B. Ginatempo, D. D. Johnson, J. B. Staunton, G. M. Stocks, and B. L. Gyorffy, "Origins of compositional order in nipt alloys," *Phys. Rev. Lett.*, vol. 66, pp. 766–769, Feb 1991.

[162] J. D. Althoff, D. D. Johnson, and F. J. Pinski, "Commensurate and incommensurate ordering tendencies in the ternary fcc cu-ni-zn system," *Phys. Rev. Lett.*, vol. 74, pp. 138–141, Jan 1995.

[163] J. F. Clark, F. J. Pinski, D. D. Johnson, P. A. Sterne, J. B. Staunton, and B. Ginatempo, "van Hove Singularity Induced $L1_1$ Ordering in CuPt," *Phys. Rev. Lett.*, vol. 74, pp. 3225–3228, Apr 1995.

[164] J. B. Staunton and B. L. Gyorffy, "Onsager cavity fields in itinerant-electron paramagnets," *Phys. Rev. Lett.*, vol. 69, pp. 371–374, Jul 1992.

[165] J. B. Staunton, J. Poulter, B. Ginatempo, E. Bruno, and D. D. Johnson, "Incommensurate and Commensurate Antiferromagnetic Spin Fluctuations in Cr and Cr Alloys from ¡i¿Ab Initio¡/i¿ Dynamical Spin Susceptibility Calculations," *Phys. Rev. Lett.*, vol. 82, pp. 3340–3343, Apr 1999.

[166] P. J. Durham, "Theory of photoemission from random alloys," *Journal of Physics F: Metal Physics*, vol. 11, no. 11, p. 2475, 1981.

[167] P. J. Durham, R. G. Jordan, G. S. Sohal, and L. T. Wille, "Bulk and Surface Effects in Photoemission from Disordered Cu-Ni Alloys," *Phys. Rev. Lett.*, vol. 53, pp. 2038–2041, Nov 1984.

[168] P. M. Aswathy, J. B. Anooja, P. M. Sarun, and U. Syamaprasad, "An overview on iron based superconductors," *Superconductor Science and Technology*, vol. 23, no. 7, p. 073001, 2010.

[169] P. C. Canfield and S. L. Bud'ko, "FeAs-Based Superconductivity: A Case Study of the Effects of Transition Metal Doping on $BaFe_2As_2$," *Annual Review of Condensed Matter Physics*, vol. 1, no. 1, pp. 27–50, 2010.

[170] C. Liu, T. Kondo, R. M. Fernandes, A. D. Palczewski, E. D. Mun, N. Ni, A. N. Thaler, A. Bostwick, E. Rotenberg, J. Schmalian, S. L. Bud/'ko, P. C. Canfield, and A. Kaminski, "Evidence for a Lifshitz transition in electron-doped iron arsenic superconductors at the onset of superconductivity," *Nat Phys*, vol. 6, pp. 419–423, Jun 2010.

[171] C. Liu, A. D. Palczewski, R. S. Dhaka, T. Kondo, R. M. Fernandes, E. D. Mun, H. Hodovanets, A. N. Thaler, J. Schmalian, S. L. Bud'ko, P. C. Canfield, and A. Kaminski, "Importance of the Fermi-surface topology to the superconducting state of the electron-doped pnictide $Ba(Fe_{1-x}Co_x)_2As_2$," *Phys. Rev. B*, vol. 84, p. 020509, Jul 2011.

[172] I. I. Mazin, D. J. Singh, M. D. Johannes, and M. H. Du, "Unconventional Superconductivity with a Sign Reversal in the Order Parameter of $LaFeAsO_{1-x}F_x$," *Phys. Rev. Lett.*, vol. 101, p. 057003, Jul 2008.

[173] H. Ding, P. Richard, K. Nakayama, K. Sugawara, T. Arakane, Y. Sekiba, A. Takayama, S. Souma, T. Sato, T. Takahashi, Z. Wang, X. Dai, Z. Fang, G. F. Chen, J. L. Luo, and N. L. Wang, "Observation of Fermi-surface–dependent nodeless superconducting gaps in $Ba_{0.6}K_{0.4}Fe_2As_2$," *EPL (Europhysics Letters)*, vol. 83, no. 4, p. 47001, 2008.

[174] C. de la Cruz, Q. Huang, J. W. Lynn, J. Li, W. R. II, J. L. Zarestky, H. A. Mook, G. F. Chen, J. L. Luo, N. L. Wang, and P. Dai, "Magnetic order close to superconductivity in the iron-based layered $LaO_{1-x}F_xFeAs$ systems," *Nature*, vol. 453, pp. 899–902, Jun 2008.

[175] A. D. Christianson, E. A. Goremychkin, R. Osborn, S. Rosenkranz, M. D. Lumsden, C. D. Malliakas, I. S. Todorov, H. Claus, D. Y. Chung, M. G. Kanatzidis, R. I. Bewley, and T. Guidi, "Unconventional superconductivity in $Ba_{0.6}K_{0.4}Fe_2As_2$ from inelastic neutron scattering," *Nature*, vol. 456, pp. 930–932, Dec 2008.

[176] M. D. Lumsden, A. D. Christianson, D. Parshall, M. B. Stone, S. E. Nagler, G. J. MacDougall, H. A. Mook, K. Lokshin, T. Egami, D. L. Abernathy, E. A. Goremychkin, R. Osborn, M. A. McGuire, A. S. Sefat, R. Jin, B. C. Sales, and D. Mandrus, "Two-dimensional resonant magnetic excitation in $BaFe_{1.84}Co_{0.16}As_2$," *Phys. Rev. Lett.*, vol. 102, p. 107005, Mar 2009.

[177] S. Chi, A. Schneidewind, J. Zhao, L. W. Harriger, L. Li, Y. Luo, G. Cao, Z. Xu, M. Loewenhaupt, J. Hu, and P. Dai, "Inelastic Neutron-Scattering Measurements of a Three-Dimensional Spin Resonance in the FeAs-Based $BaFe_{1.9}Ni_{0.1}As_2$ Superconductor," *Phys. Rev. Lett.*, vol. 102, p. 107006, Mar 2009.

[178] K. Okazaki, Y. Ota, Y. Kotani, W. Malaeb, Y. Ishida, T. Shimojima, T. Kiss, S. Watanabe, C.-T. Chen, K. Kihou, C. H. Lee, A. Iyo, H. Eisaki, T. Saito, H. Fukazawa, Y. Kohori, K. Hashimoto, T. Shibauchi, Y. Matsuda, H. Ikeda, H. Miyahara, R. Arita, A. Chainani, and S. Shin, "Octet-Line Node Structure of Superconducting Order Parameter in KFe_2As_2," *Science*, vol. 337, no. 6100, pp. 1314–1317, 2012.

[179] T. Yoshida, I. Nishi, A. Fujimori, M. Yi, R. Moore, D.-H. Lu, Z.-X. Shen, K. Kihou, P. Shirage, H. Kito, C. Lee, A. Iyo, H. Eisaki, and H. Harima, "Fermi surfaces and quasi-particle band dispersions of the iron pnictides superconductor KFe_2As_2 observed by angle-resolved photoemission spectroscopy," *Journal of Physics and Chemistry of Solids*, vol. 72, no. 5, pp. 465 – 468, 2011.

[180] F. F. Tafti, A. Juneau-Fecteau, M.-E. Delage, S. Rene de Cotret, J.-P. Reid, A. F. Wang, X.-G. Luo, X. H. Chen, N. Doiron-Leyraud, and L. Taillefer, "Sudden reversal in the pressure dependence of Tc in the iron-based superconductor KFe_2As_2," *Nat Phys*, vol. 9, pp. 349–352, Jun 2013. Letter.

[181] A. F. Wang, S. Y. Zhou, X. G. Luo, X. C. Hong, Y. J. Yan, J. J. Ying, P. Cheng, G. J. Ye, Z. J. Xiang, S. Y. Li, and X. H. Chen, "Anomalous doping effects of Co impurities on the iron-based superconductorKFe_2As_2: evidence for a d-wave superconducting state," *ArXiv e-prints*, June 2012.

[182] J. K. Dong, S. Y. Zhou, T. Y. Guan, H. Zhang, Y. F. Dai, X. Qiu, X. F. Wang, Y. He, X. H. Chen, and S. Y. Li, "Quantum Criticality and Nodal Superconductivity in the FeAs-Based Superconductor KFe_2As_2," *Phys. Rev. Lett.*, vol. 104, p. 087005, Feb 2010.

[183] S. L. Bud'ko, M. Sturza, D. Y. Chung, M. G. Kanatzidis, and P. C. Canfield, "Heat capacity jump at T_c and pressure derivatives of superconducting transition temperature in the $Ba_{1-x}K_xFe_2As_2$ ($0.2 \leq x \leq 1.0$) series," *Phys. Rev. B*, vol. 87, p. 100509, Mar 2013.

[184] W. Malaeb, T. Shimojima, Y. Ishida, K. Okazaki, Y. Ota, K. Ohgushi, K. Kihou, T. Saito, C. H. Lee, S. Ishida, M. Nakajima, S. Uchida, H. Fukazawa, Y. Kohori, A. Iyo, H. Eisaki, C.-T. Chen, S. Watanabe, H. Ikeda, and S. Shin, "Abrupt change in the energy gap of superconducting $Ba_{1-x}K_xFe_2As_2$ single crystals with hole doping," *Phys. Rev. B*, vol. 86, p. 165117, Oct 2012.

[185] K. Nakayama, T. Sato, P. Richard, Y.-M. Xu, T. Kawahara, K. Umezawa, T. Qian, M. Neupane, G. F. Chen, H. Ding, and T. Takahashi, "Universality of superconducting gaps in overdoped $Ba_{0.3}K_{0.7}Fe_2As_2$ observed by angle-resolved photoemission spectroscopy," *Phys. Rev. B*, vol. 83, p. 020501, Jan 2011.

[186] X. Zhang, Y. S. Oh, Y. Liu, L. Yan, S. R. Saha, N. P. Butch, K. Kirshenbaum, K. H. Kim, J. Paglione, R. L. Greene, and I. Takeuchi, "Evidence of a universal and isotropic $2\Delta/k_BT_C$ ratio in 122-type iron pnictide superconductors over a wide doping range," *Phys. Rev. B*, vol. 82, p. 020515, Jul 2010.

[187] D. V. Evtushinsky, D. S. Inosov, V. B. Zabolotnyy, A. Koitzsch, M. Knupfer, B. Büchner, M. S. Viazovska, G. L. Sun, V. Hinkov, A. V. Boris, C. T. Lin, B. Keimer, A. Varykhalov, A. A. Kordyuk, and S. V. Borisenko, "Momentum dependence of the superconducting gap in $Ba_{1-x}K_xFe_2As_2$," *Phys. Rev. B*, vol. 79, p. 054517, Feb 2009.

[188] T. Sato, K. Nakayama, Y. Sekiba, P. Richard, Y.-M. Xu, S. Souma, T. Takahashi, G. F. Chen, J. L. Luo, N. L. Wang, and H. Ding, "Band Structure and Fermi Surface of an Extremely Overdoped Iron-Based Superconductor KFe_2As_2," *Phys. Rev. Lett.*, vol. 103, p. 047002, Jul 2009.

[189] S. Avci, O. Chmaissem, D. Y. Chung, S. Rosenkranz, E. A. Goremychkin, J. P. Castellan, I. S. Todorov, J. A. Schlueter, H. Claus, A. Daoud-Aladine, D. D. Khalyavin, M. G. Kanatzidis, and R. Osborn, "Phase diagram of $Ba_{1-x}K_xFe_2As_2$," *Phys. Rev. B*, vol. 85, p. 184507, May 2012.

[190] C. Liu, G. D. Samolyuk, Y. Lee, N. Ni, T. Kondo, A. F. Santander-Syro, S. L. Bud'ko, J. L. McChesney, E. Rotenberg, T. Valla, A. V. Fedorov, P. C. Canfield, B. N. Harmon, and A. Kaminski, "K-Doping Dependence of the Fermi Surface of the Iron-Arsenic $Ba_{1-x}K_xFe_2As_2$ Superconductor Using Angle-Resolved Photoemission Spectroscopy," *Phys. Rev. Lett.*, vol. 101, p. 177005, Oct 2008.

[191] A. Alam and D. D. Johnson, "Chemically Mediated Quantum Criticality in $NbFe_2$," *Phys. Rev. Lett.*, vol. 107, p. 206401, Nov 2011.

[192] R. Zeller, "An elementary derivation of Lloyd's formula valid for full-potential multiple-scattering theory," *Journal of Physics: Condensed Matter*, vol. 16, no. 36, p. 6453, 2004.

[193] A. R. Denton and N. W. Ashcroft, "Vegard's law," *Phys. Rev. A*, vol. 43, pp. 3161–3164, Mar 1991.

[194] T. Wolf. Karlsruhe Institute of Technology (private communication, Oct. 2013).

[195] S. A. J. Kimber, A. Kreyssig, Y.-Z. Zhang, H. O. Jeschke, R. Valenti, F. Yokaichiya, E. Colombier, J. Yan, T. C. Hansen, T. Chatterji, R. J. McQueeney, P. C. Canfield, A. I. Goldman, and D. N. Argyriou, "Similarities between structural distortions under pressure and chemical doping in superconducting $BaFe_2As_2$," *Nat Mater*, vol. 8, pp. 471–475, Jun 2009.

[196] C. H. Lee, K. Kihou, H. Kawano-Furukawa, T. Saito, A. Iyo, H. Eisaki, H. Fukazawa, Y. Kohori, K. Suzuki, H. Usui, K. Kuroki, and K. Yamada, "Incommensurate Spin Fluctuations in Hole-Overdoped Superconductor KFe_2As_2," *Phys. Rev. Lett.*, vol. 106, p. 067003, Feb 2011.

[197] M. S. Torikachvili, S. L. Bud'ko, N. Ni, and P. C. Canfield, "Effect of pressure on the structural phase transition and superconductivity in $Ba_{1-x}K_xFe_2As_2$ ($x = 0$ and 0.45) and $SrFe_2As_2$ single crystals," *Phys. Rev. B*, vol. 78, p. 104527, Sep 2008.

[198] K. Kuroki, S. Onari, R. Arita, H. Usui, Y. Tanaka, H. Kontani, and H. Aoki, "Unconventional Pairing Originating from the Disconnected Fermi Surfaces of Superconducting $LaFeAsO_{1-x}F_x$," *Phys. Rev. Lett.*, vol. 101, p. 087004, Aug 2008.

[199] F. Wang, H. Zhai, Y. Ran, A. Vishwanath, and D.-H. Lee, "Functional Renormalization-Group Study of the Pairing Symmetry and Pairing Mechanism of the FeAs-Based High-Temperature Superconductor," *Phys. Rev. Lett.*, vol. 102, p. 047005, Jan 2009.

[200] S. Li, C. de la Cruz, Q. Huang, G. F. Chen, T.-L. Xia, J. L. Luo, N. L. Wang, and P. Dai, "Structural and magnetic phase transitions in $Na_{1-\delta}FeAs$," *Phys. Rev. B*, vol. 80, p. 020504, Jul 2009.

[201] F. Ma, W. Ji, J. Hu, Z.-Y. Lu, and T. Xiang, "First-Principles Calculations of the Electronic Structure of Tetragonal α-FeTe and α-FeSe Crystals: Evidence for a Bicollinear Antiferromagnetic Order," *Phys. Rev. Lett.*, vol. 102, p. 177003, Apr 2009.

[202] R. A. Ewings, T. G. Perring, R. I. Bewley, T. Guidi, M. J. Pitcher, D. R. Parker, S. J. Clarke, and A. T. Boothroyd, "High-energy spin excitations in $BaFe_2As_2$ observed by inelastic neutron scattering," *Phys. Rev. B*, vol. 78, p. 220501, Dec 2008.

[203] C. Chao and D. Jian-Hui, "Electronic Structure of KFe_2Se_2 from First-Principles Calculations," *Chinese Physics Letters*, vol. 28, no. 5, p. 057402, 2011.

[204] C. Ma, H. X. Yang, H. F. Tian, H. L. Shi, J. B. Lu, Z. W. Wang, L. J. Zeng, G. F. Chen, N. L. Wang, and J. Q. Li, "Microstructure and tetragonal-to-orthorhombic phase transition of AFe_2As_2 (A=Sr,Ca) as seen via transmission electron microscopy," *Phys. Rev. B*, vol. 79, p. 060506, Feb 2009.

[205] M. A. Tanatar, E. C. Blomberg, A. Kreyssig, M. G. Kim, N. Ni, A. Thaler, S. L. Bud'ko, P. C. Canfield, A. I. Goldman, I. I. Mazin, and R. Prozorov, "Uniaxial-strain mechanical detwinning of $CaFe_2As_2$ and $BaFe_2As_2$ crystals: Optical and transport study," *Phys. Rev. B*, vol. 81, p. 184508, May 2010.

[206] A. H. King and Y. Zhu, "Twin-corner disclinations in $YBa_2CU_3O_{7-\delta}$," *Philosophical Magazine A*, vol. 67, no. 4, pp. 1037–1044, 1993.

[207] B. Kalisky, J. R. Kirtley, J. G. Analytis, J.-H. Chu, A. Vailionis, I. R. Fisher, and K. A. Moler, "Stripes of increased diamagnetic susceptibility in underdoped superconducting $Ba(Fe_{1-x}Co_x)_2As_2$ single crystals: Evidence for an enhanced superfluid density at twin boundaries," *Phys. Rev. B*, vol. 81, p. 184513, May 2010.

[208] J. L. Niedziela, M. A. McGuire, and T. Egami, "Local structural variation as source of magnetic moment reduction in $BaFe_2As_2$," *Phys. Rev. B*, vol. 86, p. 174113, Nov 2012.

[209] M. J. Han, Q. Yin, W. E. Pickett, and S. Y. Savrasov, "Anisotropy, Itineracy, and Magnetic Frustration in High-T_C Iron Pnictides," *Phys. Rev. Lett.*, vol. 102, p. 107003, Mar 2009.

[210] S. D. Wilson, Z. Yamani, C. R. Rotundu, B. Freelon, E. Bourret-Courchesne, and R. J. Birgeneau, "Neutron diffraction study of the magnetic and structural phase transitions in $BaFe_2As_2$," *Phys. Rev. B*, vol. 79, p. 184519, May 2009.

[211] S.-H. Baek, N. J. Curro, T. Klimczuk, E. D. Bauer, F. Ronning, and J. D. Thompson, "First-order magnetic transition in single-crystalline $CaFe_2As_2$ detected by ^{75}As nuclear magnetic resonance," *Phys. Rev. B*, vol. 79, p. 052504, Feb 2009.

[212] A. Georges, L. d. Medici, and J. Mravlje, "Strong Correlations from Hunds Coupling," *Annual Review of Condensed Matter Physics*, vol. 4, no. 1, pp. 137–178, 2013.

[213] T. Miyake, K. Nakamura, R. Arita, and M. Imada, "Comparison of *Ab initio* Low-Energy Models for LaFePO, LaFeAsO, $BaFe_2As_2$, LiFeAs, FeSe, and FeTe: Electron Correlation and Covalency," *Journal of the Physical Society of Japan*, vol. 79, no. 4, p. 044705, 2010.

[214] K. Haule and G. Kotliar, "Coherence-incoherence crossover in the normal state of iron oxypnictides and importance of Hund's rule coupling," *New Journal of Physics*, vol. 11, no. 2, p. 025021, 2009.

[215] K. Nakamura, R. Arita, and M. Imada, "*Ab initio* Derivation of Low-Energy Model for Iron-Based Superconductors LaFeAsO and LaFePO," *Journal of the Physical Society of Japan*, vol. 77, no. 9, p. 093711, 2008.

[216] V. Anisimov, E. Kurmaev, A. Moewes, and I. Izyumov, "Strength of correlations in pnictides and its assessment by theoretical calculations and spectroscopy experiments ," *Physica C: Superconductivity*, vol. 469, no. 912, pp. 442 – 447, 2009. Superconductivity in Iron-Pnictides.

[217] P. Werner, M. Casula, T. Miyake, F. Aryasetiawan, A. J. Millis, and S. Biermann, "Satellites and large doping and temperature depedence of electronic properties in hole-doped $BaFe_2As_2$," *Nat Phys*, vol. 8, pp. 331–337, Mar 2012.

[218] G. Kresse and J. Furthmüller, "Efficient iterative schemes for *ab initio* total-energy calculations using a plane-wave basis set," *Phys. Rev. B*, vol. 54, pp. 11169–11186, Oct 1996.

[219] G. Kresse and D. Joubert, "From ultrasoft pseudopotentials to the projector augmented-wave method," *Phys. Rev. B*, vol. 59, pp. 1758–1775, Jan 1999.

[220] Z. P. Yin and W. E. Pickett, "Antiphase magnetic boundaries in iron-based superconductors: A first-principles density-functional theory study," *Phys. Rev. B*, vol. 80, p. 144522, Oct 2009.

[221] T. Shimojima, K. Ishizaka, Y. Ishida, N. Katayama, K. Ohgushi, T. Kiss, M. Okawa, T. Togashi, X.-Y. Wang, C.-T. Chen, S. Watanabe, R. Kadota, T. Oguchi, A. Chainani, and S. Shin, "Orbital-Dependent Modifications of Electronic Structure across the Magnetostructural Transition in $BaFe_2As_2$," *Phys. Rev. Lett.*, vol. 104, p. 057002, Feb 2010.

[222] J. Bardeen, L. N. Cooper, and J. R. Schrieffer, "Theory of Superconductivity," *Phys. Rev.*, vol. 108, pp. 1175–1204, Dec 1957.

[223] N. Bogoljubov, "On a new method in the theory of superconductivity," *Il Nuovo Cimento*, vol. 7, no. 6, pp. 794–805, 1958.

[224] J. Valatin, "Comments on the theory of superconductivity," *Il Nuovo Cimento*, vol. 7, no. 6, pp. 843–857, 1958.